Dark Matter searches and the Galactic Center in the very-high-energy gamma-ray universe

Emmanuel Moulin

SORBONNE UNIVERSITÉ

MÉMOIRE D'HABILITATION À DIRIGER DES RECHERCHES

Spécialité Astroparticules

présenté par

Emmanuel Moulin

DRF/Irfu/DPhP, CEA Saclay

Dark Matter searches and the Galactic Center in the very-high-energy gamma-ray universe

HDR soutenue le 18 Novembre 2019 devant le jury composé de :

Jacques Dumarchez	*Rapporteur, Président*
Gautier Hamel De Monchenault	
Antoine Kouchner	*Rapporteur*
Subir Sarkar	*Rapporteur*
Joseph Silk	

Contents

Introduction

This memoir for habilitation to conduct research presents the work I carried out at the CEA Saclay in the context the H.E.S.S. experiment and the CTA project. The central theme of this work is the quest for WIMP dark matter in their astrophysical environment and the study of the Galactic centre via gamma rays at very high energies. More technical or older contributions will not be mentioned here.

My main activity in the last decade focused to contribute to the search for dark matter. Understanding of the nature of DM is arguably one of the most fundamental questions in modern physics and cosmology. While dark matter is an essential ingredient of the Universe evolution, from its origin to the formation of galaxies and clusters, its fundamental nature remains unknown. The Standard Model of particle physics is proved to be very successful in light of the results obtained at the LHC and in particular with the discovery of the long-time sought Higgs boson. A fundamental particle candidate to explain the dark matter observed in the universe is still to be discovered.

Dark matter is a key ingredient of modern cosmology. It pervades the universe at all scales as it is inferred from a large variety of astrophysical and cosmological datasets, though it has not been detected yet except through its gravitational interaction. The possible connection with extensions of the Standard Model of particle physics being under the scrutiny of colliders, makes the identification of dark matter one of the major goals of contemporary cosmology and particle physics.

Evidences for the existence of dark matter have accumulated over the past decades. Studies of the structure of the galaxies, the large scale structure distribution based on galaxy surveys, the analysis of the structure formation after Big Bang, the chemical evolution of the Universe including the primordial nucleosynthesis, as well as observations of the cosmic microwave background unambiguously showed that the matter content of the Universe is largely dominated by non-baryonic dark matter relative to baryonic matter[1].

[1]There are new theories of gravitation that seek to do without dark matter. It is however hard to reconcile such theories with observations of large scale structures which are difficult to

Chapter 1 of this memoir briefly presents the numerous astrophysical and cosmological observations which requires the existence of dark matter. While various hypotheses have been invoked, dark matter in the form of WIMPs attracted significant interest for various reasons. Chapter 2 describes the reasons why gamma rays are arguably crucial messengers to look for WIMP signals in astrophysical environments. Searches carried out with the H.E.S.S. instrument towards selected astrophysical targets are presented in Chapter 3 together with prospective studies for the future Cherenkov Telescope Array (CTA). Chapter 4 focuses on the study of Galactic Center astrophysics in the context of the search for the origin of the Galactic cosmic rays at the highest energies.

reproduce without a dominant component of dark matter.

Chapter 1

Preamble: the cold dark matter paradigm

Contents

This chapter is intended to provide a glimpse of the cold dark matter paradigm focused on the main background required for the understanding of what is presented in the following chapters. It is not an exhaustive review but discusses the main concepts to which the search for dark matter presented in this memoir refers to.

1.1 The standard model of cosmology

The observable universe is described with a homogeneous and isotropic average geometry at large-enough scales ($\gtrsim$ 10 Mpc), the former property coming from galaxy surveys while the latter being supported by the observations of the cosmic microwave background (CMB). It is described as a system that evolves from an extremely high temperature and density state that occurred about 13 billions years ago known as *the Big-Bang*. The universe is believed to have experienced an early phase of expansion with accelerated (exponential) expansion rate, referred as to the *inflation*, during which the temperature drops down by orders of magnitude. It is believed to end up with a phase, named as reheating, from which the universe starts to grow normally and higher temperature is recovered. As the universe then expands and cools down it undergoes phase transitions with symmetry breaking that sets on the fundamental forces and departures from thermal equilibrium which gives rise to the properties of the known elementary particles and maybe new ones. At a temperature of $\sim$4000 K, the universe becomes neutral when the electrons and nuclei get bounded, called the *recombination*, from which the photons decouple from thermal equilibrium and give rise the CMB. The universe is neutral until the first stars formed which induces a period of reionization. Structure formation proceeds in a hierarchical way that eventually leads to the largest structures observed today, such as galaxies and clusters of galaxies.

The description of the geometry and evolution of the universe is given in terms of two parameters – its spatial curvature and its expansion – which appear in the general space-time metric of Robertson and Walker[1]. The Einstein's equations assuming the matter content as a perfect fluid lead to the Friedmann-Lemaître equation. The latter gives the connection between the expansion rate $H(t)$ and the total energy density of the universe $\Omega_{\rm tot}$[2]. Cosmological measurements show that the universe is very close to be geometrically flat with the curvature energy density $\Omega_{\rm k} = 1 - \Omega_{\rm tot} = 0.00040 \pm 0.00036$ from combined measurements of CMB and BAO data. Interestingly, models of cosmic inflation predict $\Omega_{\rm tot}$ to

[1]This is the general metric from the properties of homogeneity and isotropy that are observed at sufficiently large scales in the Universe

[2]$\Omega_{\rm tot}$ is defined by the total energy density today divided by the critical density $\rho_{\rm c}$ of a flat (k=0) universe.

be very close to one. The total energy density content of the universe, $\Omega_{\rm tot}$, is the sum of the energy density of radiation, baryons, dark matter and dark energy. The baryonic matter content is mainly obtained through the analysis of CMB data and from primordial nucleosynthesis. The measurements on the power spectrum the CMB performed by the Plank satellite (see Fig. 1.1) provide [1] $\Omega_{\rm B}h^2 = 0.02205 \pm 0.00028$[1] and a CDM density of $\Omega_{\rm CDM}h^2 = 0.1199 \pm 0.0027$ [1]. From the measurement of h^2, one finds that about 26% of the total content of the universe is in the form of CDM, while only $\sim$5% is made of ordinary matter. With an universe perfectly flat, the contribution to the energy density from the cosmological constant Λ is $\Omega_\Lambda \simeq 69\%$. This is the present challenge in modern cosmology: what the 95% of the total energy density of the universe is made of ?

An additional piece of evidence for the need of CDM is the gravitational lensing of the CMB. Distortions of the angular power spectrum of the CMB due to the gravitational lensing of large-scale structures[3] has been detected in Planck data which is in very good agreement with the prediction of the ΛCDM using the above-mentioned parameter values [3].

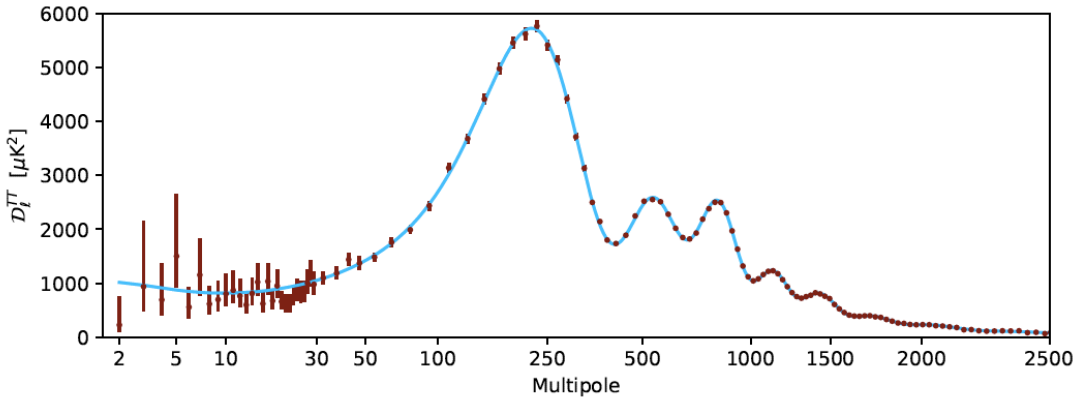

Figure 1.1: *The temperature power spectrum of the CMB shown as foreground-subtracted, frequency-averaged, cross-half-mission angular power spectrum. Figure extracted from Ref. [4].*

The cosmological ΛCDM model has clearly emerged passing numerous consistency checks, with parameters accurately measured. However, despite its stunning successes, it raised three big questions of contemporary physics: the nature

[1]Each component is given in terms of Ωh^2, where h is the scaled Hubble constant defined as $h = H_0/(100 {\rm kms}^{-1}{\rm Mpc}^{-1})$.

[2]The WMAP 7-year value is $h = 0.704 \pm 0.025$ [2], while the best-fit value given by Planck is somewhat smaller $h = 0.673 \pm 0.012$ [1].

[3]The main part of this signal comes from redshift of 2 to 3 where galactic structures formed.

of the inflation field, the nature of the vacuum energy, and the nature of dark matter. The latter one can give a strong connection between particle physics and cosmology.

1.2 Cold dark matter

1.2.1 A brief historical perspective

Dark matter plays a major role in contemporary cosmology. However, the concept of dark matter emerged more than 80 years ago before it be supported by a variety of astrophysical observations today. In the early 1930s, J. Oort studied the motion of stars in the Solar neighborhood and showed that the gravitational mass inferred from the visible stellar density cannot account for the vertical kinematics of the stars [5]. In 1933, F. Zwicky, arguably the pioneer in the dark matter field, studied the galaxy motion in the cluster of galaxies Coma. Counting the number of galaxies and the potential energy assuming an average galaxy mass, he derived the kinetic energy through the virial theorem and subsequently the velocity dispersion of $\sim$100 kms^{-1}. He noticed that the observed velocity dispersion of galaxies are too high ($\sim$ 1000 kms^{-1}) to remain bounded to the cluster over cosmic time assuming that all the mass is contained in galaxies [6]. In the early 1970s, a big step forward was performed with the measurement of galaxy rotation curve by V. Rubin [7]. The comparison of the rotation curves predicted from photometry and those measured from 21 cm observations showed that additional mass was needed in the outer parts of some galaxies. More recently, the observation of a pair of merging galaxy clusters provides another empirical piece of evidence for the existence of dark matter. The distribution of stars and galaxies is spatially separated from the distribution of hot gas traced by X-ray observations as shown in Fig. 1.2. A comparison with weak-lensing tracing the overall mass and X-ray measurements showed that the mass in this system does not follow the baryon distribution. While it has been longtime recognized that MOND is capable to reproduce the observed dynamics of spiral and elliptical galaxies, the observations of merging galaxy clusters change the debate between MOND and dark matter. On galaxy cluster scale, MOND is not as successful and fails to reproduce the dynamics of galaxy clusters, and in particular the bullet cluster. The needed additional mass cannot be accounted by MOND and a significant amount of non-ordinary matter is required. Additional keV neutrinos have been advocated in order to reconcile the merging galaxy observations and MOND.

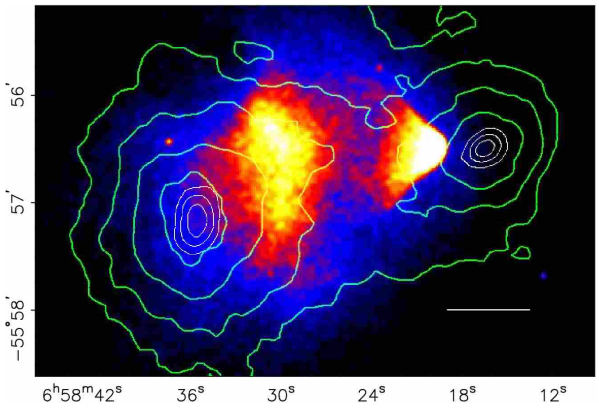

Figure 1.2: *The Bullet cluster (1E0657-558). The colored map shows the X-ray observations of the merging system carried out by the Chandra satellite. The green contours show the reconstructed weak-lensing signal proportional to the projected mass of the system. Figure extracted from [8].*

1.2.2 Dark matter distribution at galaxy and cluster scales

The evidence for dark matter at the galaxy scale comes from the measurements of rotation curves of galaxies. Observed rotation curves show a flat behavior of the circular velocities of stars as a function of the distance to the galactic center, even far away from the visible disk. While there is a consensus on the shape of dark matter halos at large distance, it is not clear whether the distribution is cuspy or cored in the inner part of the galaxies, the dark matter being a subdominant component with respect to the stellar and gas components. The observations of low-surface-brightness galaxies (see, for instance, Refs. [9, 10, 11]). Studies of the rotation curves have suggested the possibility of centrally cored dark matter profiles.

Numerical N-body simulations of gravitational clustering from initial conditions following the non-linear evolution of perturbations provide prediction of the density distribution of dark matter. Dark matter halos are observed to surround all systems. The growth of dark matter halos proceeds via mergers in ΛCDM universe and universal properties of the halos can then be confronted to observations from galactic scale up to galaxy cluster scale. These simulations using collisionless cold dark matter are well fitted by power-law density distribution in the inner halos referred hereafter as to *cuspy* profiles. Early studies [15, 16] showed that the dark matter density goes as r^{-1} towards the inner part of the halo, which is shallower than the classical isothermal profile derived from the observations of constant circular velocities in the outer regions of many spiral galaxies with a r^{-2} behavior in the observable radius range [**?**]. All the N-body

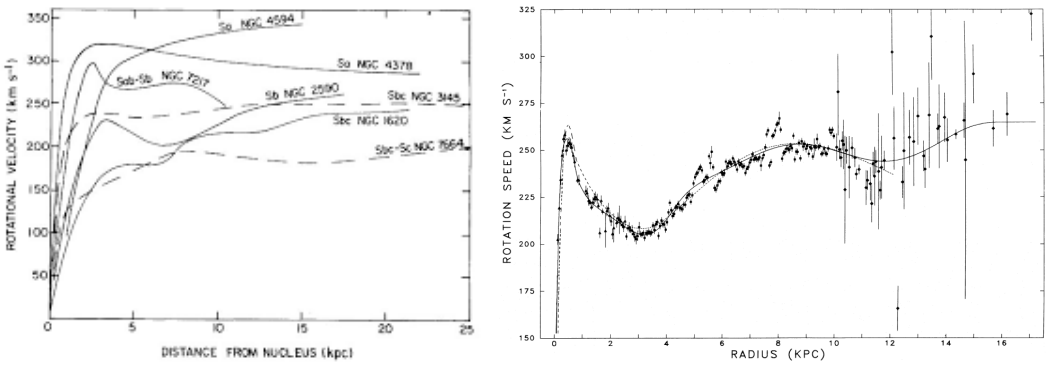

Figure 1.3: *Galaxy rotation curves.* ***Left panel:*** *Rotation curves of seven spiral galaxies of different Hubble type in the 1970s. Beyond ten kpc, the Keplerian fall is not observed. Figure extracted from Ref [12].* ***Right panel:*** *The rotation curve of the Milky Way galaxy. Figure extracted from Ref. [13]. See Ref. [14] for recent measurements.*

simulations agree on the main halo structures [16, 17, 18], and have shown a significant departure from a r^{-2} power law distribution both in the inner and outer halo regions. The predictive power is now limited by the complex interplay between dark matter and the baryonic component, which is poorly understood. From these simulations the density profiles are predicted down to about 0.1% of the virial radius[1]. Below this scale, the form of the dark matter profile relies on an extrapolation of the N-body simulation predictions. A standard parameterization of these simulated halos is gvien by the Navarro, Frenk and White (NFW) profile. Subsequent N-body simulations showed inner profiles both steeper and shallower than r^{-1}, see, for instance, Refs [20, 21]. The large scale structure formation is still far from being fully understood. The description of the evolution of structures from primordial density fluctuations, is complicated by the action of many physical processes involving baryonic physics such as gas dynamics, radiative cooling, photoionization, recombination and radiative transfer.

Clusters of galaxies are the largest and most massive gravitationally bound systems in the Universe, with radii of a few Mpc and total masses 10^{14} to 10^{15} $M_\odot$, of which galaxies, gas and DM contribute about 5, 15 and 80%, respectively [22]. Most of the dynamical estimates for galaxy clusters are consistent with a value of $\Omega_{\rm DM} \sim 0.3$. The DM halo distribution within galaxy clusters appears to be well reproduced by N-body numerical simulations for gravitational structure formation, see Refs [23, 24, 25, 22] and references therein. This may be in contrast to smaller-scale systems like dwarf galaxies where disagreements

[1]For the Milky Way, the virial radius is ∼100 kpc.

Figure 1.4: *Cosmological N-body simulation of a Milky Way-like halo. Projected dark matter density of a Milky Way-like halo at $z = 0$. The brightness of the image scales with the logarithm of the squared dark matter density. The colour hue encodes the local particle velocity dispersion. Figure extracted from Ref. [19].*

between theoretical predictions and actual estimates of the DM halo profile from observations. Although such discrepancies may vanish at galaxy cluster scale, the influence of baryon infall in the DM gravitational potential can still flatten the DM density distribution in the inner regions of galaxy clusters, see, for instance, Ref. [26].

1.2.3 Some issues with the CDM paradigm

The CDM model provides a very good agreement with observations at large scales, *i.e.* at the galaxy cluster scale and in the primordial universe. Cosmological N-body simulations of DM structuration and evolution face three main issues at galactic scale with a pure CDM model: *(i)* the predicted number of Galactic satellites is not observed; *(ii)* a cusp/core controversy in centers of galaxies developed; *(iii)* the angular momentum problem: the galactic disks are predicted too

small compared to observations. The origin of these problems may come from the lack of realism of the simulations regarding physical processes, their lack of spatial resolution, or in the nature of dark matter.

Many missing satellites ?

The missing satellite problem refers to the overabundance of predicted CDM subhalos [27, 28] compared to satellite galaxies known to exist in the Local Group. These small objects are not observed and could only be dark halos [29]. A popular interpretation of this issue relies on the statement that the smallest dark matter halos are extremely inefficient at forming stars. Alternatives include the fact that some of the dark matter is warm or self-interacting which helps to alleviate the discrepancy (see 1.2.4).

Substructures would likely survive the merging process with abundance in CDM halos [30]. Milky-Way-size halos should host a large number of satellite subhalos, with over ∼100 objects potentially massive enough to host observable satellite galaxies (with $L > 10^6$ $L_\odot$). However, only ∼10 satellites brighter than this around the Milky Way were observed at that time. This leads to conclude that dwarf galaxy formation would need to be largely suppressed to explain this discrepancy. In the late 1990's, these dwarf satellite issue has been confirmed by numerical simulations [27, 28]. More recent simulations have verified these calculations (see, for instance, Refs. [19, 20]). The mass function of substructure is predicted to rise steeply at the smallest masses, while the luminosity function of observed dwarf satellites is fairly flat.

The most important observational fact in the last decade is the discovery of a new population of faint satellite galaxies. The number of galaxy companions has more than double the known satellite population in the Local Group (see Belokurov 2009). One of the exciting point of these discoveries is that a much larger population of undiscovered dwarfs are missing satellite galaxies in halo of the Milky Way. These missing objects are extremely dark matter dominated, but too dim and/or too diffuse to have been discovered yet, at least, until recently. A large number (more than one hundred) of low-luminosity galaxies may be orbiting within the Milky Way halo. These systems have stellar distributions too diffuse to have been easily discovered so far, but new surveys and new techniques are at work that may very well reveal hundreds of these missing satellite galaxies within the next decade. Recent surveys like DES recently discovered low-luminosity satellite galaxies [31] and new surveys such as PanStarrs and SkyMapper are expected to yield numerous additional ultra-faints dSphs.

However, there are physical mechanisms that may act to suppress galaxy formation within the smallest halos. In fact, it is known that feedback processes, particularly the early reionization of gas by the first stars and winds generated by

supernovae, prevent the vast majority of the small subhalos that survive inside large CDM halos, to form visible small galaxies [32, 33, 34].

The core-cusp controversy

The core-cusp controversy refers to the discrepancy observed between the central density of dark matter halos in galaxies predicted by cosmological N-body simulations which indicates a steep power-law-like behaviour [35, 36, 37, 38] and the observed galaxy rotation curves which point to a core-like structure, see Ref. [39] for a review. A core is also observed in dwarf irregular galaxies which are dominated by dark matter.

Dwarf Irregular Galaxies[1] are dominated by dark matter and the baryon mass is dominated by gas. In these objects, the surface densities of dark matter and HI follows the same radial distribution [40]. A prototype is the dwarf irregular galaxy DDO154 [41]. A possibility of the non-observation of DM cusp is that DM would not be dominating in these galaxy centers. Note that it is already the case in more evolved early-type galaxies, dominated by the stars at their centrer. An alternative would be that the mass in the center of these HI-dominated galaxies could also be predominantly baryonic, in the form of cold condensed molecular gas.

This problem requires many efforts to solve it but no solution is perfectly satisfactory. The authors of Ref. [42] showed that black hole binaries can flatten cusps but they do not exist in dwarf galaxies. Central cusps are resilient to stellar feedback [43] while the density is moderately lowered. Bars have weak impact [44] and are not likely to be present in dwarf galaxies.

The determination of the DM density profile behaviour in the central region of galaxies suffer from large uncertainties, because the density of (visible) baryonic matter is expected to dominate that of DM at small galactocentric radii. On the observational front, this means that going from gravitational measurements of the total mass density to limits on the DM density requires careful modeling of the baryonic (stars, gas) component and has associated large systematic uncertainties. Simulation-based predictions including hydrodynamics and feedback physics in addition to the gravitational effects for the expected DM abundance have large uncertainties due to the effects of baryonic physics down to the smallest scales, and at sufficiently small galactocentric distances, the resolution limit of simulations also becomes relevant.

[1] At optical wavelengths dwarf irregular galaxies are small, faint and appear to be unstructured and irregular in shape. These systems are low surface brightness, gas-rich, metal-poor, with some level of star formation. The main difference with dwarf spheroidal galaxies is that the latter do not have neither current star formation nor detectable gas. However, they may have had distinct episodes of star formation.

The angular momentum of baryons

The angular momentum problem emerged with the small size of galaxy disks found in cosmological simulations compared to observations. In the current paradigm, baryons and dark matter at first have the same angular momentum. During the process of making galaxies through hierarchical merging, baryons lose their angular momentum to the CDM through dynamical friction. The problem may be the too early concentration of baryons and the formation of galaxy disks as a result of a merger events.

Alternatively, the disks could be formed through accretion of gas from large-scale filaments and this process could occur at late times in the formation of the galaxy. A solution could be to increase the efficiency of feedback processes during the star formation. Supernovae may provide enough energy to keep disks with angular momentum close to the value required from the observations. This also impacts the distribution of dark matter with a realistic formation of cores. The formation of disks occur late when the dark matter concentration in the central region of galaxies has been reduced. The feedback process is required to happen until late time to avoid gas from collapsing.

Another way is to accrete mass from filaments where the gas is channelled. The accretion is not spherical and the gas keeps angular momentum. This mechanism is supported by the observations of a large amount of barred galaxies. In the absence of accretion of external cold gas, the bars drive the gas towards the galaxy center. Gas experience strong dynamical friction with dark matter particles if condensed very early in galaxies. A way-out is that gas accretes slowly and is loosely bound in the outer part of the galaxy.

1.2.4 Alternatives to cold dark matter ?

A solution to form dark matter core may be found in the properties of the dark matter particles, *i.e* in the velocity of the DM particle at thermal decoupling or in the self-interaction strength of the DM particles.

The free streaming scale of warm dark matter (WDM) particles dampens the fluctuation of the matter power spectrum and flattens the mass function of the halos. All primordial density fluctuations smaller than the WDM free streaming scale λ_c are erased, with $\lambda_c \propto 1/m_{\rm WDM}$. No structure is expected to form below this scale in the bottom-up scenario of structure formation. One possible solution for WDM is that the dark matter particle is a thermal relic of the order of 1 keV. Popular representatives of WDM candidates from particle physics models are the sterile neutrino [45, 46] and the gravitino [47, 48, 49].

A kpc core in a dwarf galaxy $\sim 10^{10}\,{\rm M}_\odot$ is viable with a WDM particle mass of $\sim$0.1 keV [50, 51], the central concentration decreasing with decreasing

mass. However, X-ray background measurements and Lyman-α forest analyses constrain the allowed mass range to be between 3 keV and 50 keV [52, 53, 54, 55]. According to these constraints, a 1-to-2 keV mass WDM would produce tens-of-parsecs cores, which is not sufficient explain the possible kpc cores observed in dwarf galaxies (see, for instance, Refs. [56, 57, 58]). WDM cores form but are too small to be astrophysically relevant. Over the relevant radial range, the profiles are also cuspy but have lower concentration than CDM halos or subhalos of the same mass. Warm dark matter may not be a viable solution for explaining the presence of cored density profiles in low mass galaxies unless mixed CDM and WDM are considered [59].

Weak WDM masses reduce the cusp concentration and may create cores but on the other hand the number of small galaxies, such as the satellites of the Milky Way, depends on the mass of the warm particle. The abundance of subhalos scales with the mass of the host galactic halo. The mass of WDM needs to be high enough to have a sufficient number of satellites. A comparison of the predicted satellite luminosity functions to the observed one for the dwarf spheroidal galaxies of the Milky Way provides a lower bound on the thermally produced WDM particle mass. Contrary to the CDM, the mass function of WDM is not increasing steeply with decreasing mass and has a cutoff at small masses [60, 61]. If the WDM mass is too small, there will be too few surviving subhalos to account for the number of MW satellites. However, the number of surviving subhalos is a strong function of the host halo mass. The limit on the WDM mass then depends on the MW halo mass which is uncertain to within a factor of a few, see, for instance, Ref. [62]. In Ref. [63]: for a halo mass less than $1.1 \times 10^{12} M_{\odot}$, thermally produced WDM is ruled out. This has to be moderated since if the halo mass is greater than $2 \times 10^{12} M_{\odot}$, all WDM masses higher than 2 keV are allowed. For a particle mass of 3.3 keV [55], if the Milky Way halo mass is lower than $1.4 \times 10^{12} M_{\odot}$, WDM is not viable [63]. In conclusion, WDM with velocity dispersion of $\sim$0.1 c may solve the missing satellite problem but not the *core/cusp* issue.

Self-interacting dark matter (SIDM) [64, 65], consisting of DM particles with strong self-interaction and weak scale annihilation cross section, has been proposed to alleviate some issues between simulations and observations at subgalactic scales. The scattering cross section for the elastic collision is due to strong interaction similar to the neutron-neutron scattering at low energy. To have impact on dark matter halos over cosmological scale and not spooling the success of CDM on large scales in the universe, simulations [66, 67] show that the typical cross section per mass unit to flatten the density profile in the core of galaxies is of $\sim$ 1 barn/GeV[1], the weak scale cross section being of $\sim$ 1 picobarn. Such an

[1]This value is consistent with the Bullet cluster bounds [68].

interaction strength allows to obtain kpc cores in galaxies. However, SIDM collisions lead to shallow and spherical halos in contradiction with other observations of dense an ellipsoidal galaxy cluster cores [69, 70]. This self-interaction strength scale may be too large for galaxy clusters compared to the observation of cusps in these systems. Adding a power-law velocity dependency to the cross section may alleviate the possible discrepancy. DM is self-interacting in dwarf halos, while appearing to be collisionless in larger halos at galaxy cluster scale where relative velocity is of $\sim$1000 kms^{-1}. Considering that CDM particles interact through a Yukawa potential [71] can explain cores in dwarf galaxies without impacting the dynamics of galaxy clusters with much larger velocity dispersion. The non-trivial velocity dependency of the cross section allows the interaction to be effective for dwarf galaxies while being entirely suppressed at high velocities relevant for galaxy cluster cores and the evaporation of small subhalos within bigger halos. The energy released by collision may be higher than the gravitational binding energy and make the DM evaporate. This could explain the deficit of observed satellites compared to pure CDM expectations.

1.3 Particle candidates

1.3.1 Observational requests

Although a weak discrepancy exists between observational amounts of baryonic matter and predictions coming from Big Bang nucleosynthesis calculations indicating the existence of dark baryons, dark matter is principally non-baryonic from a wealth of convincing astrophysical and cosmological measurements. At the galactic scale, this is strengthened by the outcome of the searches for dark baryonic matter in the form of MAssive Compact Halo Objects (MACHOs) that has been conducted through microlensing measurements. The EROS experiment concluded that the MACHO contribution to the mass of the Galactic halo is less than 8% [72], which strengthens the need for a dominant non-baryonic dark matter component.

While the fundamental nature of dark matter is still elusive, observational astrophysical and cosmological measurements, from galaxy rotation curve to precision cosmology measurements (CMB, LSS, SN1a, BAO, ...) define a set of properties that must be satisfied by dark matter.

(i) It is a new particle. No candidate exhibits the necessary properties within the Standard Model of particle physics. In the standard cosmological model, dark matter dilutes as $1/a^3$ as the universe expands;

(ii) It makes up to 26% of the total energy density of the universe. $\Omega_{\rm DM}h^2 = 0.1199\pm0.0027$ from latest Planck satellite measurements;

(iii) it is cold, or not too warm. At the time of CMB, dark matter is not relativistic, $p/m << 1$;

(iv) it is feebly interacting, *i.e. collisionless*, with itself and ordinary matter. In particular, it interacts very weakly with electromagnetic radiation, *dark...*, and is colorless;

(v) it is stable on cosmological time scales. Its lifetime should be much higher than 10^{27}s;

(vi) it is possibly a thermal relic of the early universe. At a temperature of the hot plasma higher than their mass, dark matter particles are freely created and destructed in pair. As the universe cools down, their relative number density is suppressed as annihilations proceed and temperature drops below their mass. The density then freezes out as the universe expands.
The mass, interaction and charge of dark matter are however not known.

Candidates include axions, sterile neutrinos, and weakly interacting massive particles. From hierarchical structure formation theories and simulations, the non-baryonic dark matter is compatible with a gas of cold and weakly interacting massive particles (WIMPs). A major motivation for WIMPs is that in the standard thermal picture of the early universe a particle with an annihilation cross section and mass of the order of the weak interaction scale leads to the observed relic density today as discussed below. Interestingly, theories beyond the SM, mainly built in order to solve problems inherent to particle physics, like the unification of couplings at high energy and the hierarchy and naturalness problems [73] do have dark matter candidates. The currently most popular candidates for WIMPs come from the supersymmetric and extradimensional theories which are succinctly described below[1]. There has been a wealth of dark matter candidates proposed over the last decades. A huge variety of models beyond the Standard Model physics have been constructed which include a stable, electrically neutral, and colorless particle. Many of which could serve as a phenomenologically viable candidate for dark matter. An exhaustive list is not possible here and the dark matter of our universe could plausibly consist of particles ranging from 10^{-6} eV axions to 10^{16} GeV WIMPzillas depending on the set of requirements used to characterize it.

Finding the *WIMP miracle* (see Sect. 1.3.2) to be fairly compelling (along with the hierarchy problem, which strongly suggests the existence of new particles at or around the electroweak scale), dark matter in the form of weak-scale particles is presented here, with a mass in the few GeV to several tens-of-TeV range, followed by a short incursion in the dark matter candidate zoo. Exhaustive excellent reviews on the particle physics candidates can be found in Refs. [74, 75, 76, 77].

[1] Axions are also popular candidates while for different reasons compared to WIMPs. See Sec. 1.3.4 for more details.

1.3.2 Weakly Interacting Massive Particles

Massive dark matter particles with weak scale interactions, labeled as WIMPs (weakly interacting massive particles), are of particular interest. They naturally arise in many theories beyond the Standard Model of particle physics. Among the most popular ones are the lightest neutralino in Minimal Supersymmetric Models (MSSM) and first Kaluza-Klein excitations in models with extra dimensions.

In the early universe, when the temperature T is much higher than their mass $m_{\rm WIMP}$, WIMPs can be produced and destroyed. As the temperature decreases, their density is exponentially suppressed with $m_{\rm WIMP}/T$. The equilibrium is left when the temperature is not high enough to sustain the pair production of WIMPs, and only the annihilation process remains possible. As the universe expands, when the WIMP mean free path becomes comparable to the Hubble distance, WIMPs cannot self-annihilate anymore. Their co-moving density remains then constant. This process is commonly referred to as *freeze-out*. The remaining diluted abundance of WIMPs may constitute the DM today. When ones solves the Boltzmann equation, the freeze-out temperature is approximately $m_{\rm WIMP}/20$, therefore the particles are non-relativistic. For pure s-wave annihilation[1], the annihilation cross section of WIMP weighted by their relative velocity, $\langle\sigma v\rangle$, depends only on their relic density $\Omega_{\rm DM}h^2$ as:

$$\langle\sigma v\rangle \approx \frac{3\times10^{-27}\ {\rm cm^3 s^{-1}}}{\Omega_{\rm DM}h^2}\ . \tag{1.1}$$

A velocity averaged annihilation cross section of $\langle\sigma v\rangle = 3\times10^{-26}\ {\rm cm^3 s^{-1}}$ is seen therefore as the benchmark value, or a *natural scale*, since it is the one that yields the correct relic DM abundance measured in the universe.

Interestingly, for massive particles interacting at the electroweak scale, it implies $\langle\sigma v\rangle \sim \alpha^2/m_{\rm W}$ for WIMP masses of a few hundred GeV. The WIMP density is in remarkable agreement with the latest measurements of the cold DM relic density by the Planck satellite [78]. Although this could be a coincincidence, this is sometimes coined as the *WIMP miracle*. A recent and detailed calculation can be found in Ref. [79].

Supersymmetric candidates Sypersymmetry is amongst the most attractive theories beyond the Standard Model of particle physics. In particular, weak-scale supersymmetry provides us with an elegant solution to the hierarchy problem and

[1]The annihilation process generally assumes a cross-section which is dominated by a term independent of velocity (s-wave annihilation). In many DM models a s-wave annihilation cross-section can be absent or helicity suppressed. In order to reproduce the correct DM relic density in these models, the leading term in the cross section is proportional to the DM velocity squared (p-wave annihilation).

enables grand unification by causing the gauge couplings of the Standard Model to evolve to a common scale. From the dark matter standpoint, the lightest supersymmetric particle is stable under models that conserve R-parity[1]. Extensive reviews on supersymmetric dark matter exist in literature [74, 75, 76, 80]. The most natural supersymmetric dark matter candidate is the lightest neutralino $\tilde{\chi}_0$ [81]. It has gauge couplings and a mass which for a large range of parameters in the supersymmetric sector implies a relic density in the required range to explain the observed CDM relic density. The outcome of a recent scan of phenomenological MSSM parameter space [82] is shown in Fig. 1.5. On the left panel on can distinguish in the TeV mass range, two representative class of DM models : the *Higgsino* models (red points) with $\sigma v \sim 10^{-26}$ cm^{3}s^{-1}, and the prominent *Wino* models (blue points) around 2 to 3 TeV with σv values from 10^{-25} to 10^{-22} cm^{3}s^{-1}, which receive a substantial enhancement from the Sommerfeld effect. The right panel shows the number of models according to their dominant annihilation channels, *i.e.* with the largest branching fraction.

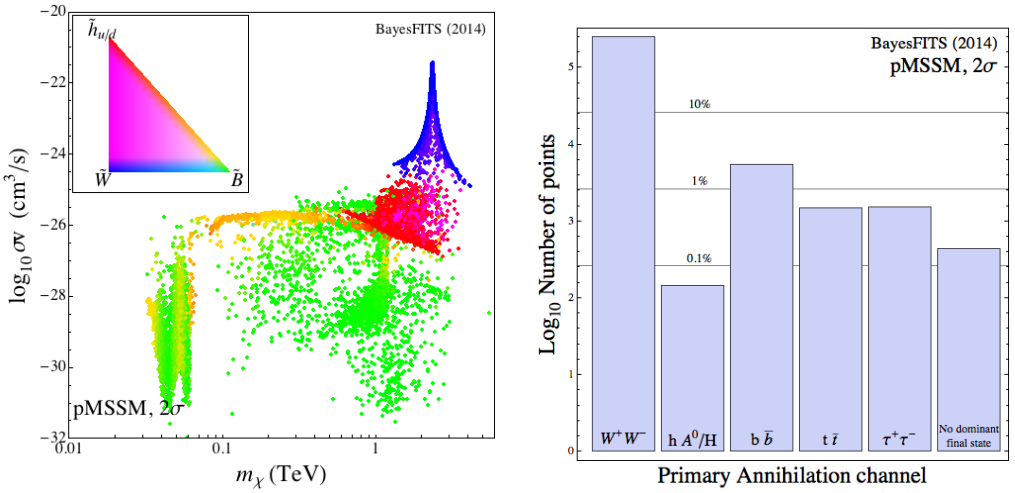

Figure 1.5: ***Left panel:*** *Distribution of the models from a pMSSM scan of the parameter space in the $(m_\chi, \sigma v)$ plane. The colours encode the composition of the lightest neutralino. Pure states are shown for the bino $\tilde{B}$ (green points), blue for the wino $\tilde{W}$ (blue points), and red for the higgsino $\tilde{h}_{u/d}$ (red points).* ***Right panel:*** *Number of models according to their primary channels from the pMSSM scan. Figures extracted from Ref. [82].*

[1]This is a multiplicative quantum number that is conserved to avoid, for example, excessive baryon number violating processes and therefore keep the proton lifetime large enough to avoid violating experimental bounds.

Kaluza-Klein dark matter An alternative to supersymmetric candidates for new weak-scale physics is the possibility of dark matter particles from extra dimensions. This idea goes back to the 1920's with the work of Kaluza and Klein [83]. Modern views are referred to universal extra dimensions (UED). In the simplest UED model, *minimal UED*, there is one extra dimension of size R compactified on a circle. Every Standard Model particle has an infinite number of partner particles, with one at every Kaluza-Klein level n with mass $\sim$ n/R. In constrat to supersymmetry, partner particles have the same spin. The lightest KK particle can be the first KK mode $\tilde{B}^{(1)}$ of the weak hypercharge gauge boson as a viable DM candidate [84]. Contrary to neutralinos for which leptonic annihilation channels are severely suppressed, the $\tilde{B}^{(1)}$ boson also has important branching ratio in direct annihilation channels such as $\tilde{B}^{(1)}\tilde{B}^{(1)} \rightarrow \nu\bar{\nu}, e^+e^-$.

TeV dark matter models The scale of the DM candidates is being pushed forward given the null results from 8 TeV LHC searches and the constraints from direct and indirect detection experiments in the hundred GeV range. Naturally models for dark matter in the multi-TeV mass range have attracted significant interest, both in the theoritical and experimental sides. Amongst them are minimal DM models assuming the standard model extension with an electroweak multiplet [85]: they include wino DM models which naturally appear as LSP in SUSY models, inert doublet models, fermionic 5-plet, scalar 7-plet. Fig. 1.6 shows an example of the velocity-weigthed annihilation cross section and relic density obtained for the 5-plet in of minimal DM models.

TeV DM models usually provide enhanced velocity-weighted cross sections though Sommerfeld enhancement compared to the natural scale. This enhancement which arises from the exchange of EW bosons among the heavy DM particles modifies significantly the annihilation cross section, giving rise to a peculiar structure in peaks. Multi-TeV WIMP DM candidates are arguably even more motivated than before, in the current context of absence of new physics from the LHC. VHE gamma rays are a powerful messengers to search for this class of models and may be being probed by current ground based Cherenkov telescopes and the future Cherenkov Telescope Array (CTA) as it will be shown in the chapter 3.

1.3.3 Bounds on WIMP masses

Assuming that resonances and coannihilations with other new particles slightly heavier than dark matter can be neglected, cosmology suggests a natural value for thermally-produced DM particle of $\langle\sigma \mathrm{v}\rangle \simeq 3 \times 10^{-26}$ cm^{3}s^{-1}. This results is independent of the dark matter particle mass, except at logarithmic corrections.

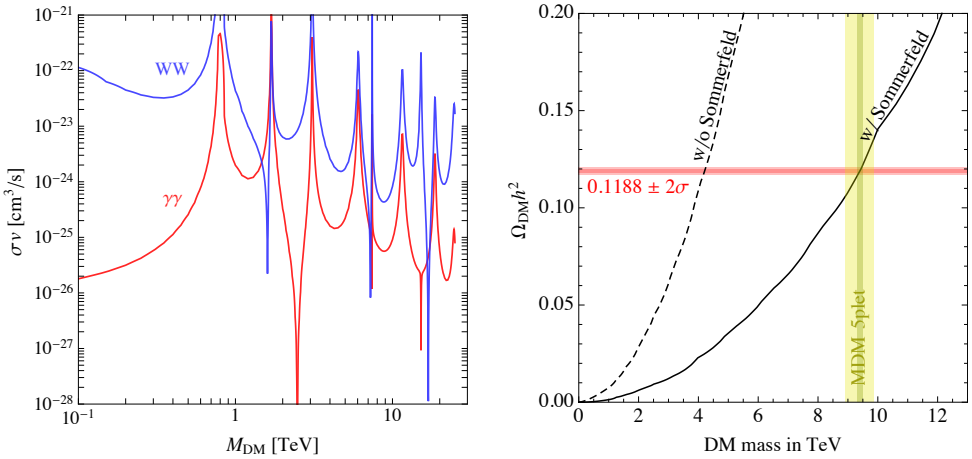

Figure 1.6: ***Left panel:*** *Velocity-weighted annihilation cross section for the 5-plet in Minimal DM models for typical Milky Way velocity values of $v \sim 10^{-3}c$. The Sommerfeld effect can be appreciated for the W^+W^- and $\gamma\gamma$ channels.* ***Right panel:*** *Relic density for the 5-plet as a function of the mass, with and without the Sommerfeld enhancement. Figures extracted from Ref. [86].*

A model-independent upper bound on the mass of the DM particle can be derived from unitarity for thermally produced DM as done in the seminal paper of Griest&Kamionkowski in 1990 [87] and subsequent studies [88, 89]. The partial wave unitarity of the scattering S matrix yields $\sigma v \leq 4\pi/m_{\rm DM}^2 v$. Assuming the current DM relic density measured by Planck [78], the inferred upper bound is about 100 TeV.

Various dark matter candidates have been proposed in the literature (see, for instance, Refs. [90, 91]). The properties of dark matter candidates are, to a large extend, unconstrained. Even if the total annihilation cross section is determined by the relic abundance, the branching ratios to specific annihilation channels are model-dependent. In the absence of a preferred model, searches need to be carried out, as far as possible, in a model-independent approach. To this end, a wide range of dark matter particle masses and annihilation spectra are considered. On a theoretical point of view, if a DM particle is thermally-produced in the early Universe and comprises all the dark matter, there are two important constraints on its properties. The first comes from the unitarity of the scattering matrix [92, 93]. Following the formalism of quantum field theory in the two-body scattering process and an expansion in partial waves, one obtains an upper bound on the annihilation cross section. In the low-velocity limit, where

s-wave annihilation dominates, this translates into:

$$\langle \sigma v \rangle < \frac{4\pi}{m_{\rm DM}^2 v} \simeq 1.5 \times 10^{-19}\,{\rm cm^3 s^{-1}} \left(\frac{1\ {\rm TeV}}{m_{\rm DM}}\right)^2 \left(\frac{300\,{\rm kms^{-1}}}{v}\right). \qquad (1.2)$$

This is often termed as *the unitarity bound*. Thus, the dark matter mass is upper-bounded by the observed relic CDM density [1]. Using the latest measurements on the CDM density gives an upper bound on the dark matter mass of about 100 TeV.

The second constraint comes from the requirement that annihilation does not significantly distort the DM halos in the universe today. It is interesting to assess how large the annihilation can be irrespective of possible early-Universe constraints, in particular the dark matter profiles of galaxies. The cross section derived in the KKT model of Ref. [94][2], can be interpreted as an upper bound corresponding to a value of the annihilation cross section which significantly distorts the halo. It expresses as:

$$\langle \sigma v \rangle_{\rm KKT} \lesssim 3 \times 10^{-16}\,{\rm cm^3 s^{-1}} \left(\frac{m_{\rm DM}}{1\ {\rm TeV}}\right). \qquad (1.3)$$

This bound constrains relatively small DM masses.

1.3.4 Other candidates

The axion remains an attractive viable dark matter candidate. Axion has been first introduced by Peccei and Quinn [95] to solve the strong CP problem of QCD in particle physics and its possible role to explain the cosmological dark matter came as a bonus. The Peccei Quinn axions that can account for the dark matter are then limited to a small range in mass. They could indeed constitute cold dark matter since they were produced non-thermally. The axion has been more and more constrained by laboratory searches, stellar cooling and supernova dynamics to be very light, with masses lower than 0.01 eV [96]. The acceptable range where axions pass all the observational constraints and would not overclose the universe [97] is around 10^{-5} - 10^{-2} eV [3]. Irrespective of axion as a solution to the dark matter problem, there are also some interesting mechanisms such

[1] Latest observations from Planck [1, 78] gives $\Omega_{\rm CDM} {\rm h}^2 \simeq 0.11$.

[2] Large annihilation rates were in fact invoked to alter the density profile of dark matter halos in the context of the core-cusp problem, solving an apparent discrepancy between predicted (sharp cuspy) and observed (flat cored) halo profiles. Note that similar effects are obtained with self-interacting dark matter.

[3] However, there are some hypothetical mechanisms in string theory that could make the mass scale smaller.

as axion-photon conversion, that could possibly influence cosmological measurements. TeV gamma-ray observations towards AGN are probing neV mass scale.

Sterile neutrinos with keV masses [46] could alleviate the "cusp/core" problem of cold DM models. They can be detected only if they mix with the ordinary neutrinos and would eventually decay into a standard neutrino and a photon or into three neutrinos. The former process gives mono-energetic photons with $E = m_S/2$, which might be observable by X-ray satellites. If they are produced by oscillations of standard neutrinos, the lower bound from structure formation (Ly-α forest) and upper bound on X-ray fluxes from clusters of galaxies strongly constrain them to form all the DM[1]. Recent observations of a 3.5 keV X-ray line found in the observations of galaxy clusters with the XMM-Newton satellite have been interpreted in terms of sterile neutrino of 7 keV. The complexity of the ISM at these energies makes any DM interpretation challenging and the signal can also be due to transitions of ionized atoms [98].

Primordial black holes of 20-to-100 $M_\odot$ could form the dark matter. The recent detections by the LIGO-Virgo experiments of gravitational signals from mergers of two black holes of a few ten solar masses push people to reconsider the possibility that they may constitute the dark matter [99]. If they would constitute all the dark matter, microlensing events of a star could be searched. For instance, the star brightness in the Andromeda galaxy may change with time due to foreground black holes passing in front of the star on the sky. The absence of significant brightness variation constrains the PBH-dark matter scenario while it cannot definitely exclude it.

1.4 WIMP detection techniques

There are a variety of methods for WIMP searches, and for dark matter particles in general. The WIMP ones can be classified in the indirect, direct and collider searches and the astrophysical probes.

Despite five times as abundant as baryonic matter in the Universe, the identity of dark matter is unknown. Uncovering its identity is a great challenge for fundamental physics and astronomy. A diversity of approaches has been devised with the goal of discovering the identity of dark matter. The observational approaches depend on the candidate under consideration for which there are many possibilities. In the case of WIMP searches, a promising array of groundbreaking experiments are positioned in the quest for dark matter.

[1]This can be evaded if there is a lepton asymmetry higher than 10^{-3} (i.e. some 7 orders of magnitude above the observed baryon-antibaryon asymmetry), and/or if there is an additional source of production in the early Universe.

The collider searches are looking for the production of dark matter particle candidates through the collision of high energy standard model particles such as electrons or protons. Candidate dark matter particles can be produced directly or through processes initiated by quarks and gluons which eventually decay into the lightest stable particle in the spectrum. New stable dark matter particles produced directly cannot be observed and these processes must be tagged by observing initial state radiation.

The direct dark matter search relies on the measurement of the WIMP of the Galactic halo scattering off a target nucleus in low background underground detectors. The elastic scattering cross section is inferred from the a -few-to-tens- of keV energy deposit from the nuclear recoil in the medium. Though there is no cosmological prediction for the fundamental scale of the elastic cross section, the current experiments are steadily improving limits and are now probing the relevant parameter space for the elastic cross section proposed in well-motivated theoretical models.

The indirect detection is seeking for the observation of the products from the self-annihilation of dark matter particles, including charged (antiprotons, positons, anti deuterium) and neutral (neutrinos and gamma-rays) particles. The expected flux in a given species is proportional to the annihilation rate that scales as the square of the dark matter density. Indirect searches then focus on regions where large dark matter densities are accumulated. Among them are the inner Galactic halo or nearby dwarf galaxies for detecting gamma-rays and neutrinos.

If dark matter is in the form of a new elementary particle, its identification requires understanding its interactions through the measurement of the cross section with standard model particles via each of the three methods described above. These three sets of measurements will be key elements to theoretically determine whether the WIMP is a single stable particle, or it is embedded into a larger theory of high energy physics, that may contain a spectrum of particles with masses larger than that of the WIMP.

Astrophysical observable : the dark matter particle properties can be also constrained through their impact on astrophysical observables. In particular, non-gravitational interactions of DM can affect central dark matter densities in galaxies and the mass of dark matter particle affecting dark matter substructure in galaxies. Such interactions may also alter the cooling rates of stars, and influence the pattern of temperature fluctuations observed in the cosmic microwave background. The Planck satellite observations through the measurement of tem-

perature angular power spectrum put constraints on the velocity-weighted annihilation cross section [78]: $f_{\rm eff}\langle\sigma v\rangle \lesssim 4 \times 10^{-28}(m_{\rm DM}/{\rm GeV})\ {\rm cm}^3{\rm s}^{-1}$. The factor $f_{\rm eff}$ encodes the fraction of the rest mass energy from DM annihilation which heats and ionizes the IGM. It depends on the details of the annihilation process: the annihilation channel, the mediator mass, and the DM mass. It ranges from 0.01 to 1 in most of the WIMP models [100, 101].

In this context, the observations of the collision of galaxy clusters enable to probe the properties of the DM particles. Although dark matter is assumed to be collisionless, a non-zero self-interaction cross section would have important astrophysical consequences, in particular in connection with some issues of the CDM model such as the DM profile shape at the center of galaxies predicted in CDM, or the overprediction of small-sized DM subhalos in galactic halos as presented in Sec. 1.2.3. In the collision of two galaxy clusters, as observed for instance in the case of the bullet cluster 1E 0657 [68], a gas sub-cluster seen in X-rays by the Chandra satellite is just exiting from the collision whereas the dark matter revealed through gravitational weak lensing measurements is observed ahead of the gas bullet. Most of the matter of the colliding clusters is separated from the baryonic matter, which give direct evidence that most of the matter in the clusters is dark. The constraints derived from this observation on the cross-section of the dark matter self-interaction is $\sigma/m < 1\ {\rm cm}^2{\rm g}^{-1}$.

The identification of dark matter, i.e. its mass, couplings strengths, ..., is the multi-faceted problem which requires a multi-pronged approach with important roles played by collider, direct and indirect dark matter detection experiments. Attempts have been made to compare the potential of these three techniques using effective field theory interpretation, though its validity is limited depending on the mediator mass with respect to the dark matter mass as discussed, for instance, in Ref. [102]). More realistic approaches are now using the minimal simplified dark model scheme where a minimum set of four parameters is used: the mediator and DM masses, the coupling of the mediator to Standard Model particle, and the coupling of the dark matter particle to the mediator (see Ref. [103]). This comparison scheme avoids misleading comparisons from the effective field theory scheme that were only valid for a sub-region of the parameter space .

1.5 On thermal WIMPs

While we have a good knowledge of the gravitational properties of dark matter from CMB and LSS, we are ignorant about the particle physics nature of dark matter. WIMPs have long time reigned as one of the leading classes of dark matter candidates as a well defined and well motivated model that must be decisively tested.

- The total annihilation cross of thermal WIMPs is pretty much independent of the WIMP mass in the GeV to hundred TeV mass range. This provides a benchmark for indirect dark matter searches, a unique feature compared to other direct detection and collider searches for which there is no target scale.

- While the thermal WIMP is not the only possibility for DM, the predictions made for such a scenario make it now testable in present-day experiments which benefited from instrumental efforts that have developed over the last few decades.

Chapter 2

The role of very-high-energy gamma rays

Contents

The astrophysical search for signals of dark matter particle pair annihilations in cosmic structures on large scales, from galaxies to clusters of galaxies, is, potentially a very powerful technique in the quest for the identification of the fundamental nature of the DM. This chapter aims to provide the main ingredients from Particle Physics and Astrophysics to WIMP dark searches in very-high-energy gamma rays in order to explain the relevance of this messenger for such a quest.

2.1 Dark matter signals in gamma rays

2.1.1 Why VHE gamma rays ?

The indirect search looks for the annihilation or decay products of DM particles in astronomical environments in the universe. Many indirect detection experiments are seeking the remnants of the DM particles that have annihilated and or decayed into Standard Model particles. Among the various species are the neutrinos, gamma-rays, antiprotons and positrons. The scale of the annihilation cross section is closely linked to the process that sets the abundance of DM in the early universe assuming that DM was in thermal equilibrium once.

Among the various species produced by the annihilation or decay of dark matter particles, gamma rays are of particular importance since they almost travel unperturbed during their propagation at the Galactic scale, and therefore trace back the spatial morphology of their sources. This is in contrast with charged particle messengers such as positrons and antiprotons which walk randomly through the magnetic field of the Galaxy. On the other hand, a TeV DM-induced gamma-ray signal provides the bulk of gamma-rays at significantly lower energies than that allowed by kinematics, where the astrophysical gamma-ray background may be severe. However, the specific spectral features of the expected DM signal is a key point against the more smoother background spectra.

2.1.2 Annihilation signals

The energy-differential gamma-ray flux from self-annihilation of dark matter particles is expressed as product of an astrophysical term and a particle physics term. It writes as:

$$\frac{\mathrm{d}\Phi(\Delta\Omega, E_\gamma)}{\mathrm{d}E_\gamma} = \frac{1}{8\pi} \underbrace{\frac{\langle\sigma v\rangle}{m_{\mathrm{DM}}^2} \frac{\mathrm{d}N_\gamma}{\mathrm{d}E_\gamma}}_{Particle\,Physics} \times \underbrace{\bar{J}(\Delta\Omega)\Delta\Omega}_{Astrophysics} . \tag{2.1}$$

The astrophysical factor, referred hereafter as to the *J-factor*, depends on the distribution of dark matter in the astrophysical object. It is generally expressed

as the integral of the mass density squared ρ^2 along the line of sight (los) in a solid angle $\Delta\Omega$ by:

$$J = \int_{\Delta\Omega} d\Omega \int_{los} ds\, \rho^2(r(s))\,. \tag{2.2}$$

The coordinate r reads $r(s) = \sqrt{s^2 + s_0^2 - 2ss_0\cos\theta}$, where s is the distance along the line of sight, s_0 is the distance of the source from the observer location, and θ the angle between the direction of observation and the centre of the object. The *Particle Physics* factor encodes the properties of the DM particle, *i.e.* its velocity-weighted annihilation cross section $\langle\sigma v\rangle$, its energy differential gamma-ray spectrum per annihilation $\mathrm{dN}_\gamma/\mathrm{dE}_\gamma$, and its mass m_{DM}.

Three types of signals can be expected from the self-annihilation of dark matter particles. A continuum of gamma-rays in the final state is obtained via the hadronization and/or decay of the fermions and gauge bosons produced in the annihilation process. The gamma-rays are produced through by the production of π^0s and their subsequent decay. The annihilation spectrum $\mathrm{d}N_\gamma/\mathrm{d}E_\gamma$ generally exhibits a sharp energy cut-off at the mass of the dark matter particle [104], the annihilation process taking place almost at rest. For the quark and gauge bosons channels, the gamma-ray spectrum peaks at about one order of magnitude below the DM mass. With the exception of the lepton annihilation channels, each of these annihilation modes result in a similar spectrum of gamma-rays.

Dark matter particles can produce gamma rays directly, via the production of two gamma rays or one gamma ray and a Z gauge boson, leading to a monoenergetic spectral signature. Such a signal provides a highly distinctive signature, often called a *smoking gun* for dark matter search in the Universe[1]. However, WIMPs do not annihilate via tree level processes to final states containing photons[2]. They may be able to produce final states such as $\gamma\gamma$ and $Z\gamma$ or γh through loop-induced diagrams. These states lead to gamma ray lines with energies of $E_\gamma = m_{\mathrm{DM}}$ and $E_\gamma = m_{\mathrm{DM}}(1 - m_{\mathrm{Z,h}}^2/4m_{\mathrm{DM}}^2)$, respectively. Such photons are produced in only a very small fraction of DM annihilations, however: these processes are suppressed by a factor α^2 compared to the continuum. However, the DM annihilation cross sections to $\gamma\gamma$ and $Z\gamma$ can be up to $10^{-28}\,\mathrm{cm^3 s^{-1}}$, while still matching the inferred cold DM relic density [106]. See Sec. 3.1.4 for more details on these models.

For DM particles annihilating into fermion pairs, gamma rays are produced from final state radiation (FSR). These processes appearing when one goes beyond the leading order have been originally highlighted in Ref. [107]. Such gamma

[1]Most conventional astrophysical signals would produce a smoother and continuous spectrum. However, it has been recently shown in [105] that cold ultrarelativistic pulsar winds could potentially produce narrow gamma-ray lines.

[2]If they did, they would be EMIMPs rather than WIMPs.

rays are produced whenever there are charged particles in the annihilation process [108]. The FSR spectrum peaks near the DM mass and then yields prominent spectral features at the highest energy end of the spectrum. It is suppressed by a factor α relative to the continuum emission. For the $\tau^+\tau^+$ channel, hadronic decay modes have a significant branching ratios. This can be particularly important in the case of Kaluza-Klein dark matter in models with one universal flat extra dimension, where the hypergauge boson $\tilde{B}^1$ is a suitable dark matter candidate. In this case, the dark matter particles annihilate significantly to e^+e^-, $\mu^+\mu^-$ and $\tau^+\tau^-$ [84, 109]. For neutralino self-annihilating in charged gauge boson pairs, radiative processes containing one photon in addition to the W bosons in the final state will give rise to a peak near the mass of the dark matter particle. This effect occurs at the price of a factor α and may give enhancement factor up to a few thousands. It is particularly efficient for masses above $\gtrsim$ 1 TeV [110]. These corrections have been deeply investigated in the case of the MSSM and in the more constrained mSUGRA [111]. In regions where there is a near degeneracy between the lightest neutralino and the tau sleptons, radiative corrections may boost the annihilation signal by up to four orders of magnitude, as in the case of the stau-coannhilation region of the mSUGRA parameter space. In case of pairs of Majorana fermion dark matter particles, the annihilation into light leptons is helicity suppressed by a factor m_l^2/m_χ^4 [112] due to the helicity properties of the DM particle. However, fermion final states containing an additional photon are not subject to such a suppression. Figure 2.1 shows gamma-ray spectra for dark matter particles of a mass of 1 TeV annihilating into quark, gauge boson and lepton pairs, respectively.

Additional gamma rays can be expected if electrons and positrons are produced in the final states. Indeed, electrons and positrons are produced through various prompt mechanisms and by the decay of charged pions. Charged pions decay through muons that eventually decay producing electrons, positrons and neutrinos. Electrons and positrons are subject to spatial diffusion and energy losses. Both spatial diffusion and energy losses contribute to determine the evolution of the source spectrum into the equilibrium spectrum of these particles, *i.e.* the quantity which will be used to determine the overall multi-wavelength gamma-ray emission induced by DM annihilation. These electrons and positrons are non-thermal and they loose their energy in the ambient medium via physical processes : the synchrotron cooling from magnetic field, the bremsstrahlung via interaction in the interstellar gas, and the inverse Compton scattering off starlight, infrared and CMB radiation field . For the energy range of interest here (E$\gtrsim$100 GeV), the main channel for the production of secondary gamma rays is the inverse Compton scattering process on ambient radiation field.

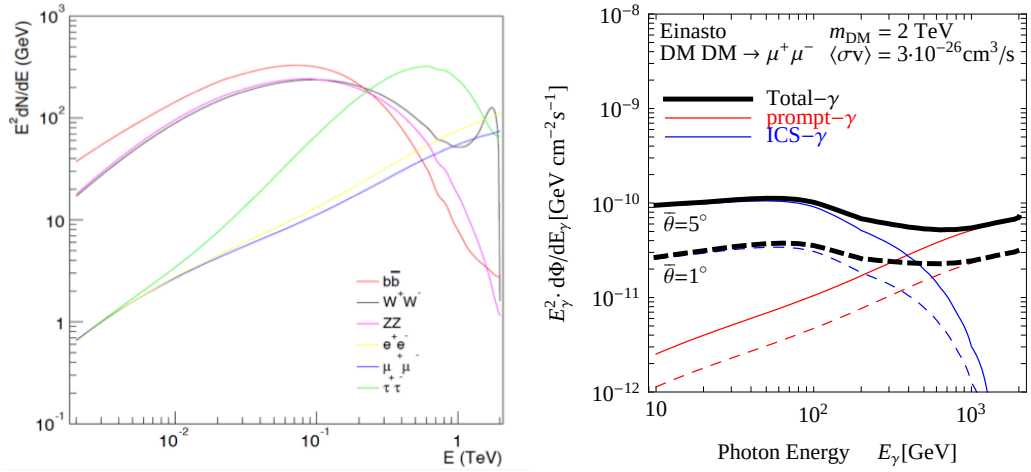

Figure 2.1: *Gamma-ray spectra for pair annihilation of 1 TeV WIMP.* ***Left panel:*** *Annihilation spectrum for 1 TeV dark matter particle self-annihilation in several channels. The spectra for quark ($b\bar{b}$, $t\bar{t}$) and ZZ gauge boson channels are nearly featureless. Annihilation spectra into leptons (e^+e^-, $\mu^+\mu^-$) peak near the kinematic end-point of the distribution. The FSR contribution in the W^+W^- channel is visible at the high-energy end of the spectrum.* ***Right panel:*** *Gamma-ray fluxes for 2 TeV DM candidates annihilating with thermal cross-section ($\sigma v = 3\times10^{-26}cm^3s^{-1}$) into the $\mu^+\mu^-$ channels. The red, blue and thick black lines denote the spectral features of the prompt, ICSs and total fluxes, respectively, expected in the Galactic Center region fro an Einasto DM profiles. Figure extracted from Ref. [113].*

2.1.3 Boost factors

A motivation for studying signal enhancement or "boost" factor has received considerable attention following the measurements on the cosmic-ray electron spectrum by ATIC [114] and PAMELA [115] experiments. Assuming any compelling astrophysical explanation[1] the dark matter interpretation requires a significant boost factor. In Ref. [114] for instance, it is shown that the cut-off in the positron flux near 500 GeV can be accommodated by a 800 GeV mass Kaluza-Klein particle assuming a boost factor of a few hundreds. Neutralinos with radiative corrections can also reproduce the steep rise in the positron to electron ratio above a few GeV measured by PAMELA[2] as shown by [122], invoking however

[1]Substantial works concentrated on the astrophysical interpretation. It has been shown that these signals can be interpreted in a conventional way. Prosaic explanations include the presence of local electron/positron sources such as pulsars or supernova remnants (see, for instance, Refs.[116, 117, 118, 119]). A few decades ago already, the presence of such spectral features from these sources has been put forward [120, 121].

[2]Such a feature has been earlier pointed out by the HEAT experiment. This interesting signal is being further investigated by the AMS-02 experiment, both concerning statistics and

boost factors of about 10^4.

Sommerfeld effect

The Sommerfeld effect [123] in the low-velocity regime can significantly boost the annihilation cross section, see, for instance, Refs. [124, 125, 126, 127, 128]. This non-relaticistic quantum effect arises because the wave function of annihilating particles is distorted by the presence of a Coulomb-like potential with Standard Model vector mediators. In the quantum field theory, this correspond to the contribution of "ladder" diagrams in which the force carrier is exchanged many times before the annihilation finally occurs. The actual velocity-weighted annihilation cross section is then $\langle\sigma v\rangle = S \times \langle\sigma v\rangle_0$, where $\langle\sigma v\rangle_0$ is the tree

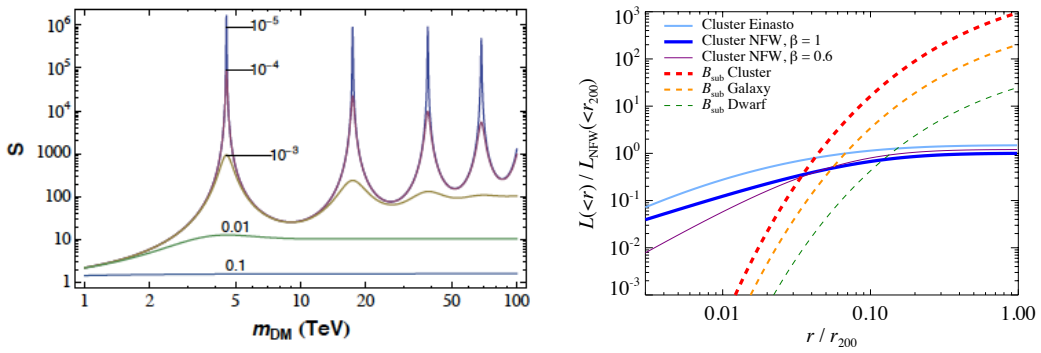

Figure 2.2: *Sommerfeld and substructure boost factors.* ***Left panel:*** *Sommerfeld enhancement S as a function of the dark matter particle mass $m_{\rm DM}$ (top-left panel) for several relative particle velocities β for the mass of the mediated boson $m_{\rm V}$ = 90 GeV and the coupling constant α_2=1/90. Figure extracted from [129].* ***Right panel:*** *Boost factor from dark matter substructures on the gamma-ray signal. Dark matter annihilation luminosity of smooth halo and substructures. Figure extracted from [130].*

level velocity-weighted annihilation cross section and the factor S the *Sommerfeld boost*. In the non-relativistic limit, the s-wave function for the two-body DM state satisfies the Schrödinger equation. Following Ref. [129], a straightforward case can be studied to extract the main physical features of this process. Considering dark matter particles interacting in an attractive Yukawa potential mediated by a boson of mass $m_{\rm V}$, the Sommerfeld boost S can be numerically calculated by solving the Schrodinger equation assuming the boundary conditions that when the two dark matter particles move away from each other, the

energy range.

two-body wave function recovers the plane wave[1]. For more details on the computation and qualitative behaviour of the factor S, see Ref. [127]. Figure 2.2 shows the behavior of the factor S for dark matter particle annihilations mediated via the Z boson and the coupling constant α_2=1/90. The Sommerfeld effect increases with decreasing β and vanishes when $\beta \to 1$. One can distinguish resonant and non-resonant behaviors, depending on the value of the DM mass and the relative velocity β. In the non-resonant case, for $\beta < \alpha$ S expresses $S = \pi\alpha/\beta$ up to a saturation value, approximately given by $S_{\max} \sim 6\alpha m_{\rm V}/m_{\rm DM}$, at $\beta \sim 0.5 m_{\rm V}/m$DM. In the resonant case, for specific values of the mass, the cross-section follows this behavior until $\beta \simeq \sqrt{\alpha m_{\rm V}/m_{\rm DM}}$. Below this critical value, the enhancement grows like $1/\beta^2$ before saturating. The Sommerfeld boost can then reach values as large as 10^5 and be efficient today in very cold environments like dwarf galaxies. A more general treatment of the Sommerfeld enhancement can be found in Ref. [127].

Halo substructures

The signals produced by WIMP pair annihilation scale with the square of the WIMP density and any DM overdensity in the astrophysical object does play a role. This contribution adds to the smooth component in the overall DM flux computation. The presence of an unmerged DM subhalo population in the host halo is firmly established via cosmological N-body simulations [19, 131, 20]. According to these simulations for Galactic halos, 10% to 50% of the dark matter mass of the Milky Way is in the form of substructures or subhalos. However, there is no consensus on what is the mass and radial distribution of the subhalos for them to light up with stars. This issue is somehow connected to the missing satellite problem (see Sec. 1.2.3) and the *too-big-to-fail issue* of ΛCDM [132].

Cosmological simulations predict subhalos down to masses of $\sim 10^6$ $M_\odot$ for Milky Way-sized halo, which is approximately 10^6 lower than the mass of the host halo. The subhalo mass function may extend down to Earth-mass ($\sim 10^{-6}$ $M_\odot$), or below, however simulations are currently not sensitive to such low masses. The low-mass cut-off of the subhalo distribution is related to the free-streaming scale of DM particles in the early Universe and is expected between 10^{-12} $M_\odot$ and 10^{-3} $M_\odot$ for typical WIMP scenarios [133]. From Milky Way-sized simulations, the mass function of subhalos with mass greater than $\sim 10^6$ $M_\odot$ follows a power law that scales as $dN/dM \propto M^{-\alpha}$, with α being between 1.9 and 2.0. Low-mass subhalos dominate the distribution by number while the high-mass subhalos dominate the total mass in substructure.

[1]For $m_{\rm V} \to 0$, the potential becomes Coulomb-like and the Schrödinger equation has the same form as the one that describes the hydrogen atom.

The density profile of the subhalos is subject of debate. Simulations show that the profile can be accomodated by both a Einasto profile [19] and profiles steeper than the NFW parametrization [20, 134]. The gamma-ray signal is also sensitive to the concentration of the subhalos. Substantial uncertainties remain on the relationship of the concentration versus the halo mass, which is measured only down to $\sim 10^8$ $M_\odot$ [135]. The substructure contribution implies a significant increase of the overall DM signal though it relies strongly on extrapolation. There are several treatments of the substructure boost, see, for instance, Refs. [136, 137, 138]. The right panel of Fig. 2.2 shows that it can be up to a factor 10 for dwarf galaxies and up to a factor 1000 for galaxy clusters. Contrary to dwarf galaxies, gamma-ray emission in galaxy clusters is expected to be due to non-thermal processes from cosmic-ray interactions in the gas. While this standard emission traces the centrally-concentrated gas density, the DM emission is more extended due to the contribution of substructures. However, the value of the boost factor is a highly debated quantity from galaxy to galaxy cluster scale.

DM subhalos without associated stars have not yet been conclusively detected in the Milky Way halo. A gamma-ray signal from these objects will be a smoking-gun for dark matter, though their theoretical expected DM signal is subject to a substantial amount of theoretical assumptions.

2.1.4 Decaying dark matter

Although annihilating dark matter is widely discussed in the context of dark matter searches, decaying dark matter has also gained interest, in particular of in the context of very heavy ($\sim$ PeV) dark matter. A particle making up the dark matter in the universe may well have a long but finite lifetime. In this case and if the dark matter particle decays in Standard Model particles, the decay process can be observed. Depending on the particle lifetime, non-thermal particles arising from the decay process can alter key episodes of the early universe such as the nucleosynthesis of light elements or the decoupling of the cosmic microwave background. Therefore, light elemental abundances and the CMB spectrum can be used to set constraints on particle models with an unstable dark matter particle candidate [139]. Among the decay particle debris gamma rays and antimatter (such as energetic cosmic-ray positrons, anti-protons and anti-deuterons) are ideal signals for indirect dark matter detection. As such, gamma-ray and cosmic-ray antimatter data have been extensively used to set constraints on the lifetime of unstable particle dark matter candidates.

The decaying dark matter lifetime can be taken short enough to produce signals observable in the high energy cosmic ray and gamma-ray experiments. Assuming that the lifetime of the dark matter particle is of a few 10^{26} s, it has

been invoked to explain the cosmic-ray spectra measured by PAMELA, Fermi and H.E.S.S. in the spectral fluxes of positrons and electrons. On the other hand, this value is sufficiently long to be in agreement with the cosmological dark matter abundance as well as astrophysical and cosmological observations. Regardless of the cosmic-ray anomalies, there is no shortage of models where the dark matter particle candidate is unstable, see, for instance, Refs. [140, 141, 142] for a miscellaneous list of references.

The expected gamma-ray flux can be obtained from Eq. (2.1) with the following substitutions $\langle\sigma v\rangle/2m_{\rm DM}^2 \to \Gamma/m_{\rm DM}$, with $\tau = 1/\Gamma$ is the dark matter particle decay lifetime, and $\rho^2 \to \rho$ because the decay is a one-body process. In this case the flux is proportional to the density and not to the square of the density, boost factors from halo substructure are therefore not relevant. Galaxy clusters are promising targets for decaying DM. While the signal originating from annihilating DM is proportional to the square of the DM density, for decaying DM the dependence is on the first power.

Dense DM concentrations shine above the astrophysical backgrounds if annihilation is at play, but remain comparatively dim if DM is decaying. Decaying DM wins instead, generally speaking, when large volumes are considered [143].

2.2 Modelling the dark matter distribution

2.2.1 Cusped and cored profiles

A prominent parametrization of cusped profiles from high-resolution cosmological N-body simulations is the double power law model, the NFW profile [16], nearly universal over a wide range of halo masses, defined by:

$$\rho_{\rm NFW}(r) = \rho_{\rm s} \left(\frac{r}{r_{\rm s}}\right)^{-1} \left(1 + \frac{r}{r_{\rm s}}\right)^{-2} . \tag{2.3}$$

This DM halo is parameterized by a virial mass $\rm M_{vir}$ and a concentration parameter $c_{\rm vir}$. $M_{\rm vir}$ is defined as the mass inside the radius $\rm R_{vir}$ assuming a mean density equal to 200 times the critical density of the Universe [144]. The normalization parameter ρ_0 and the scale radius $r_{\rm s}$ can be related to the virial mass and the concentration parameter using the following relations [16], $\rho_{\rm s} = M_{\rm vir}/4\pi r_{\rm s}^3 f(c_{\rm vir})$ and $r_{\rm s} = R_{\rm vir}/c_{\rm vir}$, where the function $f(x)$ is, neglecting constants, the volume integral of the NFW profile given by $f(x) \equiv \ln(1+x) - x/(1+x)$. The profile mass is given by $M(< r) = M_{\rm vir}\, f(r/r_{\rm s})/f(c)$.

Simulations with improved spatial resolution in the central region of the halos showed that the asymptotic behavior in $1/r$ is not achieved and the profile

becomes shallower towards the center of the halo [145]. These results favor the Einasto parameterization expressed as:

$$\rho_{\rm E}(r) = \rho_{-2} \exp\left[-\left(\left(\frac{r}{r_{-2}} \right)^{\alpha} - 1 \right) \right], \tag{2.4}$$

where r_{-2} is the radius at which a log slope of -2 is achieved and ρ_{-2} is the density at r_{-2}. For Milky Way-sized halos, $\alpha = 0.17$ [145]. Similarly to the NFW case, the concentration is given by $c_{\rm vir} = R_{\rm vir}/r_{-2}$.

Another important prediction of the cosmological simulations for the structure of the halos is their concentration. The lower the halo mass is the more it is centrally-concentrated. The concentration-mass relations for the NFW and Einasto profiles can be found in Ref. [146] and Ref. [147], respectively. Extrapolation to low halo masses are subject to uncertainty by several orders of magnitude [148].

The above predictions of the cosmological simulations are valid for dark matter-only simulations. They do not include the effect of baryonic physics. Incorporating baryons into the N-body simulations dramatically increases their complexity. Predictions on the dark matter and total mass distribution require a realistic treatment of the baryons and their dynamical interactions with the dark matter from the early time. The centre of galaxies are complex environments and a number of astrophysical processes may likely change the initial dark matter density distribution. Baryons induce repeated epochs of feedback due to star formation activity. Because baryons dissipate energy and so collapse to smaller scale than dark matter, they constitute a sizeable fraction of the mass in the central regions. In the central regions of galaxies the gravitational potential is dominated by baryons and the dark matter distribution is expected to evolve due to interaction with these components. Collisionless dark matter simulations have reached maturity and much effort have been devoted recently to implement gas hydrodynamics and a description of star formation within simulations [149, 150, 151, 152, 153]. Feedback processes including supernova winds, radiation from young stars, and radiation and heat from black hole accretion play a crucial role in galaxy formation.

Feedback processes impact on the scaffolding of dark matter during galaxy formation, cuspy DM distributions in halo may be altered and may produce core-like DM distributions. However, there is no consensus so far on the DM profile shape at scale lower then 10^{-3} $R_{\rm vir}$.

Two different parametrizations are often considered for cored DM halos. The observation of flat rotation curves in galaxies suggests that the radial density including stellar populations, interstellar gas and dark matter is approximately

isothermal: $\rho(r) \propto r^{-2}$. As the dark matter part is dominant in the outer part of the galaxies, the dark matter density profile should be close to that of an isothermal sphere. This profile has been extensively used in the context rotation curve studies (see Ref. [154] and references therein). The pseudo-isothermal density and mass profiles are given by :

$$\rho(r) = \rho_{\rm c} \left(1 + \left(\frac{r}{r_{\rm c}}\right)^2\right)^{-1}. \tag{2.5}$$

$M(< r) = 4\pi\rho_{\rm c}^3\, h(r/r_{\rm c})$ where the function $h(x)$ is, apart from constants, the volume integral of the pseudo-isothermal profile given by $h(x) \equiv x - \arctan(x)$. Another cored model parametrization that is also often fitted to rotation curve data is the Burkert profile [9] given by:

$$\rho(r) = \rho_{\rm c} \left(1 + \frac{r}{r_{\rm c}}\right)^{-1} \left(1 + \left(\frac{r}{r_{\rm c}}\right)^2\right)^{-1}, \tag{2.6}$$

where $\rho_{\rm c}$ and $r_{\rm c}$ are the core density and radius, respectively. The mass profile is given by $M(< r) = 4\pi\rho_{\rm c}^3\, g(r/r_{\rm c})$, where the function $g(x)$ is, apart from constants, the volume integral of the Burkert profile given by $g(x) \equiv 2\ln(1+x) + \ln(1+x^2) - 2\arctan(x)$.

2.2.2 The Jean modelling

The dark matter mass of a system at dynamical equilibrium dominated by dark matter can be inferred by the kinematics of the tracers of the gravitational potential through the Jeans equation [155]. Assuming spherical symmetry and the system composed of tracers[1] and dark matter to be only pressure-supported, the Jeans equation writes as:

$$M(r) = -\frac{r\langle v_r\rangle^2}{G}\left(\frac{{\rm d}\log\rho_*}{{\rm d}\log r} + \frac{d\log\langle v_r\rangle^2}{d\log r} + 2\,\beta\right), \tag{2.7}$$

where ρ_* is the tracer density profile, $\langle v_r\rangle^2$ is the radial velocity dispersion of the tracers. β is the tracer velocity anisotropy between the tangential and radial velocity dispersions defined as $\beta = 1 - \langle v_t\rangle^2/\langle v_r\rangle^2$. The tracer distributions are typically parameterized with either a Plummer or King profiles [156]. Assuming a mass model, the enclosed mass $M(r)$ is then fitted to observables. The determination of β requires the measurements of proper motion of the individual tracers and at the moment the stellar sample is quite limited. This lead to the mass-anisotropy degeneracy [157]. In practice, the radial dependence of β is

[1] Tracer mean objects whose kinematics can be used to recover properties of the total gravitational potential.

therefore parametrized. This method is particularly useful for the determination of the dark matter distribution in dwarf galaxies where the stellar tracer dynamics in these system is dominated by the gravitational potential induced by dark matter (see Sec. 2.3.4).

Note, however, that very recently the proper motions of stars of the classical dwarf galaxy Sculptor based on data from the Gaia mission and the Hubble Space Telescope have been measured and the radial and tangential velocity dispersions have been derived. The anisotropy parameter shows that stars move preferentially on radial orbits [158]. Such measurements will allow to more precisely reassess the mass distribution models in dwarf galaxy satellites of the Milky Way and comparison with the commonly assumed conventional models. Recently, measurements of proper motions of seven ultra-faint dwarf galaxies have been performed using GAIA DR2 [159].

2.2.3 Baryon and black hole feedbacks on dark matter halos

There are extensive works that aim to quantify the effects of baryons in modifying the dark matter distribution. While discrepancies between observations and simulations remain, the deeper understanding of galaxy formation will help to test the CDM paradigm for the hierarchical clustering. The following paragraphs provide a brief glimpse on the possible impact of baryons and massive black holes on the dark matter distribution.

Baryons

It has been early realized that the dark matter density profiles can be enhanced by the adiabatic contraction of baryons [160, 161]. Baryons cool, relax through two-body collisions and fall into the center of the dark matter halo. This process perturbs the dark matter distribution since in the center the gravitational potential is substantially modified. The dark matter reacts to the infall of baryons and the dark matter is compressed towards the centre of the halo. The strength of this effect depends on the fraction of baryons that slowly dissipates by radiative cooling. The response of a dissipationless dark matter halo to the infall of dissipational baryons is denoted as the model of adiabatic contraction. It can be conveniently treated using adiabatic invariants [155]. Pioneering analytical expressions for the adiabatic contraction process have been calculated in Ref. [160] for purely radial and circular orbits.

For a particle in a purely circular orbit within a spherically-symmetric mass distribution with spherical shells which do not cross each other, the quantity

$r\,M(<r)$ is constant, where $M(<r)$ is the mass enclosed in a radius r, as long as the mass inside r changes slowly with time. Under these assumptions, the final DM profile $M_{\rm DM,f}$, is related to the initial DM and baryon profiles $M_{\rm DM,i}$, $M_{\rm b,i}$, and the final baryon profile $M_{\rm b,f}$ by $[M_{\rm DM,i}(<r_{\rm i}) + M_{\rm b,i}(<r_{\rm i})]r_{\rm i} = [M_{\rm DM,f}(<r_{\rm f}) + M_{\rm b,f}(<r_{\rm f})]r_{\rm f}$, where $r_{\rm i}$ and $r_{\rm f}$) are the initial and final particle radii, respectively. Given that the initial baryon and DM distributions can be obtained through N-body simulations and the final baryonic distribution is measured today, the final DM distribution can thus be computed numerically. This model has been tested in high-resolution numerical simulations [162, 163] and it predicts a DM density within the virial radius in relatively good agreement with observations. An improved model can be obtained including the possibility of elongated orbits [163, 164]. The effect of the contraction of DM in response to the cooling of baryons is relevant in the calculation of the DM annihilation in baryonic environments such as the Galactic center [165, 164].

Massive black holes

Massive black holes at the centre of dark matter halos can either steepen or shallow the dark matter profile, depending on whether the black hole grew adiabatically or via mergers of smaller objects. The effect of a black hole growing slowly in the dark matter halo has been studied in Ref. [**?**]. The dark matter distribution inevitably reacts to the formation of a massive black hole. This process has been extensively studied in the case of black hole embedded in a dense stellar system. For a black hole that grows slowly[1], the stars bounded to the black hole form at first a stellar density cusp with a $r^{-3/2}$ behavior. For time much longer that the relaxation time, the system will eventually evolve towards an equilibrium density following a $r^{-7/4}$ dependence. In the case of dark matter, the term "spike" has been introduced to describe the subsequent enhancement of the dark matter density around the central massive black hole. If the black hole grows adiabatically, the density of matter around will increase. Assuming an initial dark matter profile with $\rho \propto r^{-\gamma}$, both conservation of mass and conservation of angular momentum imply that the final profile scales as $\rho \propto r^{-\gamma_{\rm sp}}$ with $\gamma_{\rm sp} = (9-2\gamma)/(4-\gamma)$ [166]. If one starts with an initially flat dark matter density, the new profile will be a mild spike proportional to $r^{-3/2}$. If the pre-existing density goes as r^{-1}, the final density will be a power law of index $9/4$. While compelling, this scenario relies on assumptions, in particular the adiabatic growth of the black hole. Dynamical processes like off-center formation of the seed black hole, or major merger events, may lead to destruction or reduction of the spike [167, 168].

[1]The black hole growth occurs over a time that is much longer that the crossing time while the age of the black hole is small compared to the relaxation time of the system.

On the other hand, if the massive black hole forms by mergers, the dark matter particles can be ejected from the central region by three-body encounters. This results in cored profiles. The formation of central stellar nuclei in galaxies via merging of star clusters would also destroy initial central cusps and would end up with constant density in the inner regions [169]. Similar mechanisms have been studied in the context of galaxy cluster halos. In Ref. [170], it is shown that the energy transfer from galaxies moving in the dark matter halo by dynamical friction would flatten the dark matter cusp to reach a core-like density distribution. Stellar formation feedback has the effect to flatten the dark matter density distribution. Even if a violent event can eject a important baryon fraction causing the dark matter to be redistributed, this effect is expected to be modest [171]. More realistic simulations to study the feedback from supernova explosions and stellar winds show that bulk gas motion could transfer sufficient energy to dark matter to create large core profiles [172]. The effect of bars in disk galaxies on the dark matter distribution have been studied and the importance of this process debated [173, 174, 175]. Even if bars can transfer angular momentum to the dark matter particles, Ref. [176] showed that this effect on the central dark matter is negligeable.

2.2.4 The mass profile of the Milky Way

The Milky Way is the best-studied galaxy. It is a gravitationally-bound system composed of stars, gas and dark matter. At the heart of the galaxy lies a supermassive black hole with a mass $4.4 \times 10^6 M_\odot$, as inferred from the orbits of tens of stars in the inner 0.01 pc. The baryonic components in visible light are the bulge, the disk which contains the spiral arms, and the stellar halo. About 90% of the baryonic mass is contained in stars while the remaining 10% are formed by gas and dust. In order to uncover information on the DM distribution, the distribution of stars and gas must be extracted by different stellar populations. Gas and stars are the kinematic tracers of the overall gravitational potential. The knowledge of the DM distribution closely relates to the accuracy achieved on these measurements. Our position within the Milky Way's dark matter halo makes more difficult to determine its dark matter density than for many external galaxies.

Spectroscopic measurements of stars in the outer region of the dark matter halo performed by the Sloan Digital Sky Survey (SDSS) allow to determine the mass profile of the Milky Way from the kinematics of a large sample of 2400 Blue Horizontal Branch (BHB) stars. They provide the best measurements up to 60 kpc with $M(\leq 60\,\mathrm{kpc}) = (4.0 \pm 0.7) \times 10^{11}\ M_\odot$ [177], in agreement with the measurements at larger radii that determinates $M(\leq 80\mathrm{kpc}) = 6.9^{+3.0}_{-1.2} \times 10^{11}\ M_\odot$ [178]. Measurements with different sets of stellar population yields a

compatible value but with larger error bars. The mass measurements of the Milky Way based on the kinematics of the tracers (halo stars, globular clusters or dwarf galaxies) of the gravitational potential gives $(0.5 - 2) \times 10^{12}$ $M_{\odot}$. More precise measurements are used to normalize a given DM profile such the total mass within a given galactocentric radius. Distant satellite galaxies of the Milky Way can be used [179], however whether the outlier satellite is bound or is just passing through the Galaxy may be not clear.

The normalisation of the dark matter profiles usually utilizes the measured dark matter density in the Solar neighborhood together with a measurement of the enclosed mass of the Milky Way in a large radius from the GC. Recent measurements of the local DM density gives $\rho_{\odot}^{\mathrm{DM}} = 0.39 \pm 0.03$ GeVcm^{-3} [180] obtained by fitting a complete model of our galaxy (stellar disc, stellar bulge/bar, ISM gas, dark matter halo) to large set of observational data.

GAIA satellite will provide kinematic data that are expected to improve on the systematic uncertainty in the measurement of the local dark matter density [181], while it will be difficult to significantly improve the determination of the shape of the profile near the Galactic center.

2.3 Astrophysical targets and challenges

2.3.1 The Galactic Center

The center of the Milky Way is most likely the brightest source of gamma rays induced by DM particle annihilation because of its large amount of dark matter and proximity. However it is a crowded regions where numerous conventional sources shine at VHE. In addition, diffuse emission (see Chap. 4) from cosmic ray interaction and propagation in the interstellar medium is detected and requires a careful analysis treatment in order to extract a dark matter signal in the Galactic Center region.

Dark matter distribution in the central kiloparsecs

Given our position within the Milky Way disk, the Galactic centre is a delicate region. It is obscured in optical light by about 30 magnitudes. The best windows for observing it is at the infrared and radio wavelengths from which the properties of bulge stars like shape, ages, metallicities, and kinematics can be determined.

The stellar bulge has a barred shape and a mass of $\sim 10^{10}$ $M_{\odot}$. It dominates the gravitational potential up to 2-3 kpc, the gas component within a few kpc being of $\sim 10^{9}$ $M_{\odot}$. Closer towards the center of the Milky Way, the nuclear stellar cluster is extending over 1 pc and has a total stellar mass of $\sim 10^{6}$ $M_{\odot}$.

It dominates the gravitational potential from a few pc down to about 0.1 pc which corresponds to the radius of influence of the black hole. The central black hole can affect the distribution of dark matter as mentioned above. Assuming a NFW profile without Sagittairus A*-induced enhancement of the dark matter density distribution, the dark matter mass in the central ten pc is about 10^4 $M_\odot$. The dark matter and disc components are subdominant to the overall potential compared to the bulge one. Extracting the dark matter distribution has proven to be challenging and is almost unconstrained, such that it is not possible to state whether the distribution steeply rises towards the Galactic Center or remains constant in the bulge [182]. Assumptions are made on the profile shape that is represented by cuspy and cored parametrisations.

A dark matter spike at the Galactic Center ?

Dark matter spikes at the centers of galaxies can be present today. However, they may be altered on Gyr timescale by both the presence of a black hole and the stars. The dark matter gravitationally interacts with the stars and the scattering decreases the DM spike by kinetic heating as pointed out in [183, 184, 185]. Assuming a DM spike with $\gamma_{\rm sp} = 9/4$ experiencing stellar kinematic heating at the Galactic centre during about 10 Gyrs, the DM density distribution will eventually behave as $\rho_{\rm DM} \propto r^{-3/2}$ in the range $10^{-5} < r/r_{\rm h} < 10^{-2}$, with the gravitational radius of influence $r_{\rm h} \simeq 1.6$ pc for the GC black hole[1]. Interestingly, assuming no DM spike, *i.e.* $\gamma = 1$, the effect of stellar heating is to increase the initial spike to 3/2. The DM mass captured after 10 Gyrs could be about 10^4 $M_\odot$ assuming $\rho(r_{\rm h}) = 100$ $M_\odot pc^{-3}$. The amplitude of the possible dark matter enhancement is rather uncertain [184] and depends, for example, on the growth history of the SMBH [186].

Following the approach carried out in Ref. [187], a dark matter spike in the Galactic Center may have been resilient to baryon influence over the Gyr time scale. However, the profile can be significantly smoothed in the central pc by off-center formation of a black-hole seed [188] and/or gravitational scattering between dark matter and stars in the central nuclear cluster [184].

2.3.2 Galactic globular clusters ?

Globular clusters are dense stellar systems of $\gtrsim 10$ Gyr old, found in haloes of galaxies, with typical masses from 10^4 up to a few 10^6 $M_\odot$ similar to the lightest dwarf galaxies. However, globular clusters are much more compact than dwarf

[1]The radius of influence of a black hole is defined as the distance at which the enclosed mass equals twice the mass of the back hole.

galaxies. Observations of globular clusters do not suggest the need for a significant amount of DM, and instead these objects are dominated by baryons [155].

The formation scenario of globular clusters is yet not clear, see, for instance, Chapter 7 of Ref. [189] for an overview. In the primordial formation scenario of globular clusters [190], they were formed in DM minihalos before or during the reionization [191], before the formation of galaxies. However the distribution of globular cluster colors [192] suggests that only metal poor clusters have a cosmological origin while metal rich clusters formed in star-forming events such as galaxy-galaxy mergers. The existence of an extended dark halo required by the primordial formation scenario, has been challenged recently in Refs. [193] and [194]. They show that the stellar kinematics of NGC 2419, a remote GC which experiences little tidal effects from the Milky Way, is incompatible with the presence of an extended dark halo. However, in Ref. [195], it is shown that the measured spread in the Ca abundance can be only explained if NGC 2419 is the remnant of a more massive object. The formation scenario of globular clusters is under debate and in some case globular clusters could be devoid of dark matter.

Assuming that globular cluster formed in a dark matter mini-halos, the initial DM reacts to the infall of baryons and is pulled in towards the center during the evolution of the globular cluster. This process is usually referred to as the adiabatic contraction model [196, 197, 162, 198, 199]. The effect of the contraction of DM in response to the baryon infall is particularly important for the calculation of the DM annihilation in such baryonic environments.

The distribution of baryons and dark matter is affected by the kinetic heating of DM by baryons [185] and by the presence of a black hole [166] as mentioned in Sec. 2.2.3. A growing body of observations on globular clusters shows that they may harbor intermediate mass black holes (IMBHs) with masses ranging from 10^3 to 10^5 $M_\odot$, although the existence of these objects is not yet firmly established. Several globular clusters may host IMBHs such as NGC 6388 [200], ω Centauri [201] in the Milky Way or even G1 in M 31 [202, 203].

If both the mechanisms of adiabatic compression of dark matter by baryon and black hole are at stake, Galactic globular clusters may be targeted for indirect dark matter with gamma-rays (see Sec. 3.4) provided that the dark matter has not been washed out during their dynamical evolution over Gyr time scale. Note, however, there is no observational requirement for dark matter in globular clusters.

2.3.3 Substructures in the Milky Way halo

Intermediate mass black holes

Intermediate mass black holes (IMBH) are compact objects with masses comprised between that of the heaviest remnant of a stellar collapse, $\sim$ 20 $M_\odot$ [204, 205], and the lower end of the mass range of Supermassive Black Holes (SMBH) $\sim 10^6$ $M_\odot$ [206, 207]. Indirect evidence includes the extrapolation of the empirical relation M_{BH}-M_{Bulge} found for the supermassive BHs in galactic nuclei, which leads naturally to the prediction of existence of IMBHs [208]. Observational hints of the existence of IMBHs come from the detection of ultra-luminous X-ray sources that are apparently not associated with active galactic nuclei [209, 210, 211], from stellar kinematics in some globular clusters [212, 201] and emission-line time lags in galaxies [213]. From a theoretical point of view, a population of massive black hole seeds could help to explain the origin of SMBHs. Besides that, a population of IMBHs is a generic prediction of scenarios that seek to explain the properties of supermassive black holes [214, 215, 216]. However, despite their theoretical interest, it is difficult to obtain conclusive evidence for the existence of IMBHs.

The consequences of the formation and growth of IMBHs on the surrounding distribution of DM have been studied in Ref. [217]. In particular, it was shown that these processes lead to the formation of strong dark matter overdensities called *mini-spikes*, which are ideal targets for indirect dark matter searches, as they would appear as a population of gamma-ray pointlike sources with identical energy spectrum. The properties of mini-spikes have been discussed in detail for two different scenarios. In the first one (scenario A), black holes are remnants of the collapse of Population III (or "first") stars [218], which are believed to collapse directly to black holes in the mass range $M \sim 60 - 140$ $M_\odot$ and $M \gtrsim 260$ $M_\odot$ [219]. The second scenario (scenario B) is representative of a class of models in which black holes originate from the collapse of primordial gas in early-forming halos [220, 221, 222, 223, 224, 225, 216]. Futher discussion on the IMBH formation scenarii is provided in Ref. [217].

Dark matter annihilations in mini-spikes

The growth of massive black holes inevitably affects the surrounding distribution of Dark Matter as mentioned above. The profile of the final DM overdensity, called *mini-spike*, depends on the initial distribution of matter, but also on astrophysical processes such as gravitational scattering off stars and mergers. Putting these astrophysical effects aside, and assuming adiabatic growth of the black

hole[1], one can calculate analytically the functional form of the final DM profile (see Sec. 2.2.3). If one starts from an initially uniform DM distribution, which is the most likely situation for black holes in scenario A, the final profile will be a mild mini-spike with density $\rho_{\rm sp} \propto (r/r_h)^{3/2}$ (e.g. see [226] and references therein). If one starts from a cuspy profile that is a power-law with index γ, as relevant for scenario B, the new profile is a new power-law, $\rho_{\rm sp}(r) = \rho(r_{\rm sp})\,(r/r_{\rm sp})^{-\gamma_{\rm sp}}$, where the radius of the spike is $r_{\rm sp} \approx 0.2\,r_h$ [185], and $\gamma_{\rm sp}$ is related to the initial power-law index γ by [166] $\gamma_{\rm sp} = (9-2\gamma)(4-\gamma)$. In the case of the Navarro, Frenk and White profile, $\gamma = 1$, which implies $\gamma_{\rm sp} = 7/3$.

To calculate the annihilation flux, the singularity of $\rho_{\rm sp}$ at $r = 0$ needs to be cut off; a minimal radius $r_{\rm cut}$ is introduced. One limit is given by the size of the IMBH, another by the condition that the annihilation rate of the dark matter particles is smaller than the inverse age of the mini-spike : $\rho_{\rm sp}(r_{\rm lim}) = m_\chi/\sigma v\,(t - t_f) \equiv \rho_{\rm lim}$. An inner cut-off is therefore defined at a radius $r_{\rm cut} = {\rm Max}\,[4R_{\rm Schw}, r_{\rm lim}]$, where $R_{\rm Schw}$ is the Schwarzschild radius of the IMBH[2]. For common values of the mass and cross section of the DM particle, $r_{\rm lim} \sim 10^{-3}$ pc so that $r_{\rm cut} = r_{\rm lim}$.

There are a number of astrophysical effects, such as off-center formation, major mergers, and gravitational scattering off stars, that tend to erase any DM overdensity. However, all these astrophysical processes are unlikely to take place around IMBHs. Mini-spikes around IMBHs that never experience mergers are expected to be stable structures over cosmological timescales, and they may be therefore promising targets for indirect detection. See Ref. [217] for expected gamma-ray flux determination. The left panel of Fig. 2.3 shows the integrated luminosity function of IMBHs in a Milky Way-sized halo, *i.e.* the number of black holes $N_{\rm BH}$ producing an integrated gamma-ray flux higher than a given flux, as a function of the integrated flux. This can be understood as the number of black holes that can be detected with a telescope of given integrated flux sensitivity. The point-source sensitivity (5σ, 25 hours at 20° zenith) for H.E.S.S. is plotted for comparison. The integrated luminosity is shown in the case of the aforementioned scenarios A and B, for three different dark matter particle masses and an annihilation cross section $\sigma v = 3 \times 10^{-26}$ cm^{3}s^{-1}. This value allows for the thermal relic density of the DM particle to account for the measured cold dark matter density $\Omega_{\rm CDM}$. Here, DM particles are assumed to be neutralinos annihilating in the $b\bar{b}$ channel. For the assumed value of σv, a large number of IMBHs in the Milky Way may be within the reach of H.E.S.S. sensitivity for scenario B, see Sec. 3.3.

[1]It is assumed that the black hole grows on a time scale much longer than the dynamical time scales of DM around it

[2]The Schwarzschild radius of a black hole of mass $M_{\rm bh}$ is given by $R_{\rm Schw} = 2.95\,{\rm km}\,(M_{\rm bh}/{\rm M}_\odot)$.

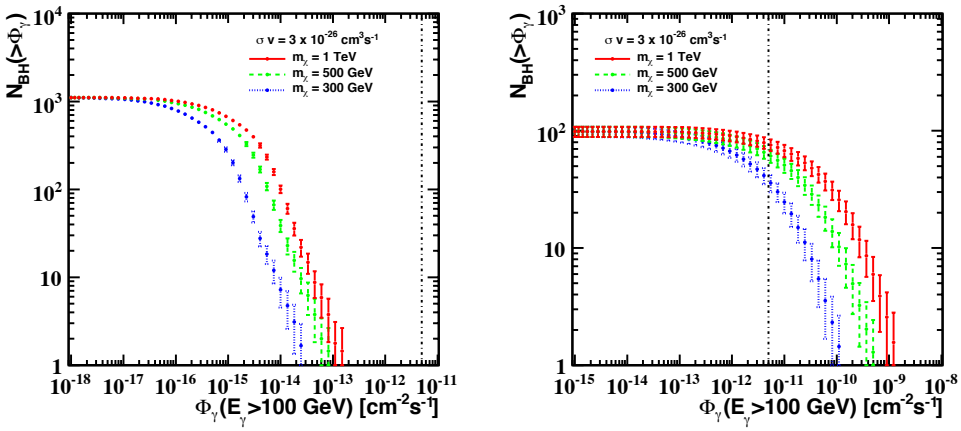

Figure 2.3: *Intermediate-mass black hole luminosity functions. Integrated luminosity function of IMBHs for the scenarii A (left panel, IMBH masses of* $\sim 10^2$ $M_\odot$*), and B (right panel, IMBH masses of* $\sim 10^5$ $M_\odot$*), respectively, for a Milky Way-sized halo obtained from an average of 200 stochastic realizations. Neutralino masses of 300, 500 GeV and 1 TeV, respectively, and a velocity-weighted annihilation cross section* $\sigma v = 3 \times 10^{-26}\, cm^3 s^{-1}$ *are considered. Figure extracted from Ref. [227].*

Galactic subhalos

The IMBH substructure scenario is optimistic in the sense that the abundance and the properties of intermediate-mass black holes and of the dark matter spikes around them remain poorly constrained [228]. Cosmological N-body simulations outcome to numerically well resolved distributions of CDM structures in the Galactic halo [20, 229]. Up to 50% of the dark matter mass of the Milky Way could be bound up in the form of substructure, or subhalos. According to the CDM model, a fraction of these subhalos should host the observed dSphs. However, there is no consensus as to what the mass and radial distribution are for the subhalos that light up with stars. Recent accurate cosmological N-body simulations of the Galactic CDM halo are able to resolve subhaloes down to about 10^6 $M_\odot$ throughout the Galactic halo and even as close to the Galactic center as the solar neighborhood. Much smaller CDM subhaloes are expected to survive in the Galactic halo.

For the purpose of the discussion, the CDM subhalo distribution is extracted from the Via Lactea-II simulation [230]. The resolved subhaloes increase the luminosity of the entire halo as seen by a distant observer by a factor of 1.9. Including the smaller unresolved haloes expected to exist in CDM does increase this factor to values between 4 and 15, depending on extrapolations done for the

abundance and properties assumed for these smaller clumps. The total luminosity from subhaloes may also increase by similar factors considering their own subsubstructures [9]. Smooth subhaloes can be considered in order to provide conservative predictions. Within 1 kpc of the Solar System, a local enhancement is expected, and can reach about 40%.

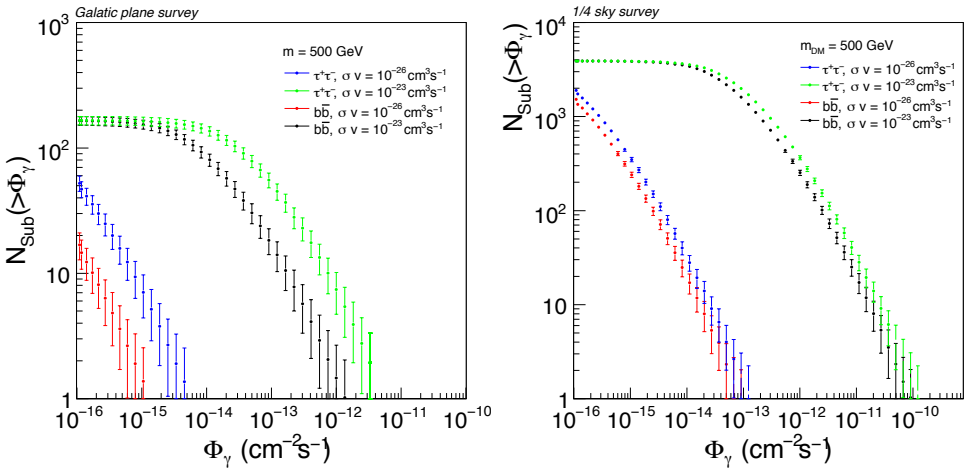

Figure 2.4: *Integrated luminosity function for the VL-II subhaloes in the H.E.S.S. Galactic Plane Survey (left panel) and in a one-quarter-of-the-sky survey (right panel). The considered WIMP mass is 500 GeV; different cases for the annihilation parameters are considered: annihilations into $b\bar{b}$ and $\tau^+\tau^-$ and cross sections of 10^{-23} and 3×10^{-26} $cm^3 s^{-1}$, respectively.*

The smallest resolved clumps have dark matter annihilation luminosities of $L = 1.7 \times 10^5 M_\odot^2 pc^{-3}$, and their mean local separation is 5.8 kpc, *i.e.* in a random realization they are found at a median distance of ∼2.9 kpc from the observer. The expected flux for $\langle \sigma v \rangle = 3 \times 10^{-26}\,cm^3 s^{-1}$, and mass of DM particles of 500 GeV annihilating into $\tau^+\tau^-$ pairs is $7 \times 10^{-14}\,cm^{-2} s^{-1}$ from such a small, but still well resolved, VL-II clump. The observable flux sensitivity for H.E.S.S. is about $10^{-12} cm^{-2} s^{-1}$. This means that the smallest clumps that the VL-II simulation is able to resolve are already too faint to be observed by H.E.S.S. or the CTA for most random realizations. Fig. 2.4 shows the integrated luminosity of dark matter subhalos to estimate how many subhaloes could be visible for a given sensitivity in the Galactic Plane survey (left panel) and in a quarter-of-the-sky survey (right panel), for a mass of WIMP of 500 GeV annihilating into $b\bar{b}$ and $\tau^+\tau^-$ pairs and cross sections of 10^{-23} and 10^{-26} $cm^3 s^{-1}$. The H.E.S.S. Galactic survey has been used to investigate the conventional scenario of CDM subhalos in Sec. 3.3.

While the dark matter profiles in central part of the substructures may not be well constrained, the DM annihilation on these substructures does not rely on fur-

ther density enhancements such as the possible dark matter spike that can form around intermediate-mass black holes. Subhalos without any associated stars have to be conclusively detected around the Milky Way. The expected gamma-ray signal from these objects is subject to a substantial amount of theoretical assumptions. The density profile of the dark subhalos is a subject of uncertainties, the smallest of them $\sim 10^{-6}$ $M_\odot$ may have stepper profile than NFW. The concentration of the subhalos versus their mass is also widely debated and the concentration-mass relationship is only determined down to about 10^8 $M_\odot$. A detection of an object that shines only in gamma rays would be a spectacular confirmation of both the CDM and the WIMP paradigm.

2.3.4 Dwarf spheroidal galaxies

All the galaxies observed in the Universe are dominated by a dark matter component at sufficiently large radii. The ratio of dark matter to luminous matter varies from galaxy to galaxy, the smallest dwarf galaxies having the highest ratio. Dwarf spheroidal galaxies (dSph) are the most numerous galaxies in the universe. Those orbiting under the Milky Way gravitational potential influence are referred to as satellite galaxies. Before the advent of the Sloan Digital Sky Survey (SDSS), the number of satellite galaxies was limited to eleven. Until the early 2000s, the nearest dSph was Sagittarius discovered in 1994 [231]. Soon after, the unequalled photometric sensitivity of SDSS permitted to detect a new population of dSphs. Among this new class are the ultra-faint systems Willman 1, Ursa Major II, Coma Berenices and Segue 1 that are currently targeted for indirect dark matter searches with high-energy gamma rays. A list of dSphs and candidate dSphs can be found in Table 1 of Ref. [232].

Dwarf galaxies are promising targets to search for DM particle annihilation signatures through gamma rays given the following consideration: *(i)* The study of stellar dynamics shows that dSphs are among the most DM-dominated systems in the Universe, with mass-to-light ratio up to a few hundreds. Kinematics of stars then permits to determine their dark matter content and possibly distribution, their kinematics being dominantly driven by the DM gravitational potential. *(ii)* Baryon-DM interaction is not expected to play a major role in the distribution of DM, even in the central region of the object. *(iii)* Many of them lie in the 100 kpc distance range from Sun, making them realistic targets for indirect searches. *(iv)* They show favorable low gamma-ray backgrounds, due to the lack of recent star formation history and little or no gas (up to the present observation sensitivity) acting as target material for cosmic-rays. *(v)* The DM annihilation signal is expected to be less sensitive to the dark matter halo distribution compared to the inner Galactic centre halo. *(vi)* The substructure boost factor is predicted to be negligeable rendering the interpretation of limits straightforward. The

relevance of dwarf galaxies as promising targets for dark matter searches has been emphasized in Ref. [233] in the early 2000's.

Dwarf galaxies can be divided in two classes. The classical dSphs are well-established astrophysical objects with relatively high surface brightness and hundreds to thousand of identified member stars, such as Draco, Fornax and Sculptor. Despite the growing amount of stellar kinematical data, the dark matter profile of classical dSphs is still subject of debate in the inner part and both cored and cuspy profiles can accomodate the stellar kinematics. Fornax and Ursa Minor show hints for the presence of a cored profile [234, 235]. While expectations from cosmological N-body simulations favor cuspy profiles, they remain uncertain in the most central part due to lack of spatial resolution. Analyses of the velocity dispersion data on the eight brightest dSphs shows that both cuspy and cored profiles can well reflect the measured stellar velocity dispersion data, see, for instance, Ref. [236]. The complex interplay of stars, gas and dark matter during the galaxy formation could erase the cusp leading to dark matter cores [237, 172, 169, 238, 239].

Current optical surveys such as DES and PanStarrs reveal the existence new ultra-faint dSphs. More additional ultra-faints dSphs are expected to be detected [240, 241]. Indeed, a new population of low-luminosity dSphs with a peak surface brightness lower than 30 mag arcsec^{-2} (*i.e.* below current detection thresholds) is expected [242]. Toy models applied to numerical N-body simulations predict the discovery of 3-13 L $\gtrsim 10^3$ L$_\odot$ and 9-99 L $\lesssim$ 103 L$_\odot$ (*i.e.*, ultrafaint) dwarfs with DES, and 18-53 L $\gtrsim 10^3$ L$_\odot$ as well as 53-307 L $\lesssim 10^3$ L$_\odot$ dwarfs with LSST [243]. Ultrafaint dSphs are likely to be hosted by light dark subhalos ($\lesssim 10^6$ M$_\odot$) which could be orbiting in the vicinity of the Solar system. These future surveys will extend significantly the knowledge of dwarf galaxies in the southern sky where CTA will have the highest sensitivity. Very recently, the DES data revealed new Milky Way satellites [244, 245], such as Reticulum II, Tucana II and the candidate dSph Tucana III that are very good targets for H.E.S.S. observations (see Sec. 3.2.3). With forthcoming in-depth studies of their dark matter content and distribution using dedicated spectroscopic measurements, these ultra-faint dSph candidates will be well-motivated targets for CTA observations.

Cored or cusped distributions ?

The standard approach to extract the mass density profile is performed with the measurement of the line-of-sight velocities of stars incorporated in the Jeans equation assuming spherical symmetry and dynamical equilibrium for the stellar and dark matter distributions. The mass density include the dark matter, gas and star contributions but the latter two contributions are negligible in the

overall gravitational potential. Despite the quality of the observational stellar dataset, there is a debate as to whether the stellar kinematics can be accommodated by a unique model of the gravitational potential. Modelling the kinematic dataset with the spherical Jeans equation using a single population of stars is found to be unable to discriminate between cusped and cored profiles, due to the mass-anisotropy degeneracy. Data are fully consistent with both profiles, see, for instance, Refs. [136, 246]. The spherical symmetry of the Jeans equation is an assumption. Observations show that they may be elongated [247]. However, relaxing this assumption give consistent results with the spherical case [248].

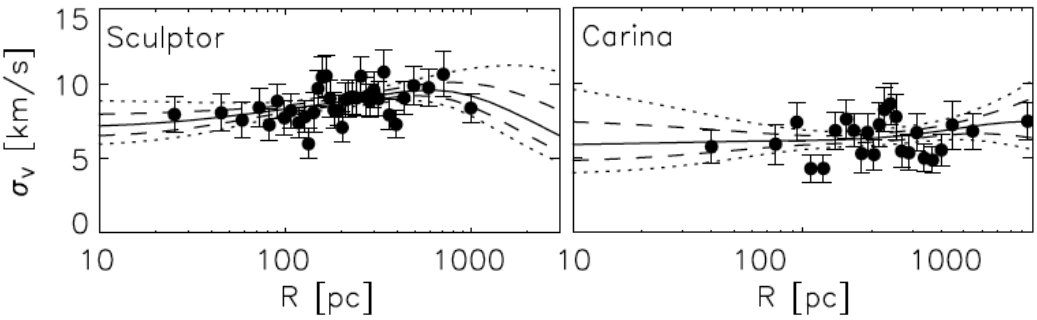

Figure 2.5: *Line-of-sight stellar velocity dispersion profiles observed for the Milky Way's classical dwarf spheroidal satellites Sculptor (left panel) and Carina (right panel) as a function of the projected radius R. The median velocity dispersion form a Markov-Chain Monte Carlo analysis is given by the solid curve as well as the and the 68% (dashed line) and 95% (dotted line) containment bands. Figure extracted from Ref. [249].*

In some dSphs more than a single population of stars can be identified. For the classical dSphs like Sculptor or Fornax, with more than a thousand of member stars, it is possible to isolate two distinct stellar populations, a centrally-located metal-rich population and a more extended metal-poor one. Numerous papers discussed the cusped or cored DM distributions in these dSphs. In Ref. [56], it is found the the NFW profile is severely constrained and a core is significantly preferred. However, it is possible to find stellar distribution models with a NFW DM profile that are consistent with the two stellar populations [250]. The example of Sculptor highlights the difficulty to determine whether the central DM distribution is cored or cusped. While with the presently available kinematic dataset[1] it is not possible to determine the slope of the central distribution, the

[1]The measurement of stellar proper motions may enable to break the parameter degeneracy in the Jeans equation [251, 252], though the required accuracy of about a few km/s per star is likely to be challenging even for modern observatories.

mass integrated with the half-light radius is found to be almost independent of the central slope [253]. The mass measurement translates directly into a J-factor determination up to the half-light radius. At this distance, the J-factor determination is best constrained from the stellar kinematics. Assuming a generalized double power-law profile, determinations of the J-factor through spherical Jeans equation method are consistent as shown in Refs. [254, 249, 255]. Fig. 2.6 shows the radial behavior of the J-factor for the recently detected ultra-faint dSph MW satellites Reticulum II and Triangulum II, which places them among the most promising dSphs for dark matter search. So far, no hints for a significant fraction of binary stars in Reticulum II has been observed. However, it may be the case for Triangulum II for which the J-factor may be artificially inflated by the presence of binary stars compared to initial determination based on six stars [256]. Recent spectroscopic data might indicate that it is either a star cluster or a tidally stripped dwarf galaxy [257].

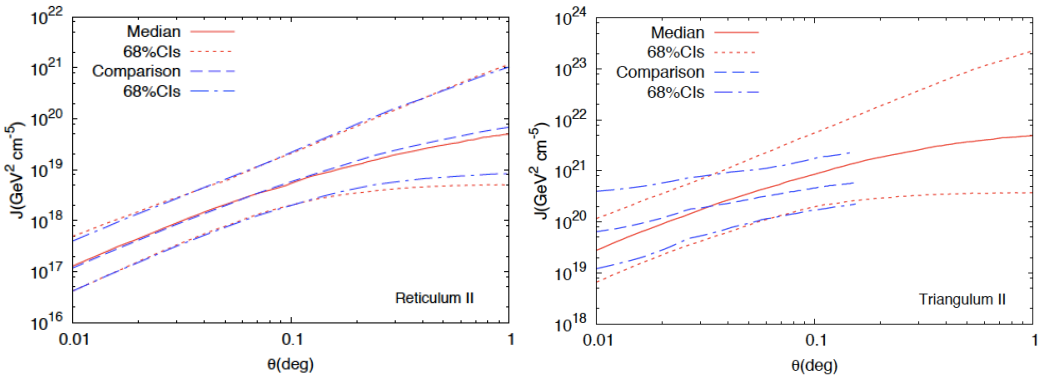

Figure 2.6: *J-factors of Reticulum II (left panel) and Triangulum II (right panel) as a function of integration angle θ from the nominal gravitational center of the system. The red solid line and dotted lines represent the median value and 68% CL containment band, respectively. The blue dashed dotted-dashed lines representing the the same quantities computed in Ref. [258] for Reticulum II and in Ref. [259] for Triangulum II. See also Ref. [257] for updated measurements. Figure extracted from Ref. [260].*

dSphs are unique targets for dark matter searches with gamma rays. Substantial modeling and observational works are dedicated to the understanding of the dSph kinematics and their underlying dark matter distributions. Any possible detection of a dark matter signal in other environments must be corroborated by a detection in the privileged environment of dSphs.

Systematic uncertainty in the J-factor determination

Observations of stellar velocities within dSph galaxies allow one to constrain the DM density profiles, through the Jeans equation of local dynamical equilibrium for assumed stationary systems, $\nabla \cdot \mathcal{P} = -\nu \nabla\Phi$, where $\mathcal{P} = \nu\sigma^2$ is the anisotropic dynamical pressure, ν is the density of the observed tracer (stars in the dSph), $\boldsymbol{\sigma^2}$ is the squared velocity dispersion tensor, while Φ is the gravitational potential. In spherical symmetry, as nearly always assumed for dSph modeling, the Jeans equation can be rewritten as

$$\frac{(\nu\sigma_r^2)}{r} + 2\,\frac{\beta(r)}{r}\,\left(\nu\sigma_r^2\right) = -\nu(r)\frac{G\,M(r)}{r^2}\ , \tag{2.8}$$

where $M(r)$ is the total mass (DM, stars, possible gas and black hole), $\beta = 1-\sigma_\theta^2/\sigma_r^2$ is the *velocity anisotropy* (hereafter, anisotropy), which usually depends on the physical radius r (and where by symmetry, one has $\sigma_\phi = \sigma_\theta$). The Jeans equation (2.8) contains two unknowns, the mass profile $M(r)$ and the anisotropy profile $\beta(r)$ for a single equation, which is usually called the *mass-anisotropy degeneracy*. There are basically two classes of algorithms to such *mass-anisotropy modeling* (see chap. V of Ref. [261] and references therein): 1) methods based on binning the projected radii and measuring the 0th (surface density), 2nd (l.o.s. velocity dispersion), and possibly 4th (l.o.s. kurtosis) moment of the l.o.s. velocity distribution; 2) fitting the distribution of stars in *projected phase space* (projected radii and l.o.s. velocities).

The computation of the J-factors come with several systematic uncertainties. Here below are the main ones.

- Distinguish member stars from interlopers in the foreground (Milky Way stars) is crucial. The inclusion of interlopers tends to increase the width of the l.o.s. velocity distribution, which leads to higher DM normalizations, hence higher J-factors. Furthermore, when they orbit the Milky Way, dSph galaxies are affected by its tidal field, leading to tidal tails, which tend to be elongated towards the center of the Milky Way [262], hence roughly elongated along the l.o.s. given the fairly small distance of the Sun to the center of the Milky Way. This also tends to inflate the l.o.s. stellar velocity dispersion viewed by an observer on Earth [263]. Admittedly, the alignment of the tidal tail with the l.o.s. is usually not perfect, so the observer should notice an increase of the l.o.s. velocity dispersion at large projected radii. For instance, different methods of handling interlopers lead to typical differences in the J-factor of 0.1 dex, especially in poorly-sampled dSph galaxies at low galactic latitudes (i.e. with important contamination by Milky Way foreground stars) [264].

- There are several stellar populations in many dSph galaxies, each with different distributions [265, 266] each with its own Jeans equation probing the same gravitational potential. Neglecting the different stellar population by considering a single one will decrease the accuracy of the derived J-factors.

- The choice of the data binning can affect the mass-anisotropy modeling to the point of concluding to either dark matter cusp or core depending on the choice of binning scheme [267]. This should lead to differences of at least 1 dex in the J-factors.

- Most of mass-anisotropy modeling studies of dSph galaxies assume spherical symmetry, although these galaxies appear to be slightly flattened along the line-of-sight. The assumption of spherical symmetry leads to typical overestimates of J by 0.5 dex [268] and probable uncertainties of 0.2 dex.

- Nearly all mass-anisotropy modeling assume constant velocity anisotropy, while one expects that the outer regions should have more radial orbits, as inferred in giant elliptical galaxies from simulations [269]. For mock dSph galaxies with isotropic orbits inside and strongly radial orbits outside, the assumption of constant velocity anisotropy leads to overestimates of J as high as 0.7 dex [268] and probable uncertainties of 0.2 dex.

- The stellar density profiles of dSph galaxies are not well known because their overall surface densities are low and difficult to distinguish against the foreground Milky Stars, even after selecting with colors and metallicities. This should produce uncertainties of 0.2 dex in the J-factors.

- Even the center of a classical dSph like Fornax is uncertain by a few arc minutes [270]. An incorrect center should lead to underestimate on the cuspiness of both stellar and DM density profiles, hence on underestimated J-factors. An estimate of the impact of incorrect centering on the J-factor is at the level of 0.2 dex uncertainty.

- The usual mass-anisotropy modeling of dSph kinematics in the context of J-factors incorrectly assumes that the l.o.s. velocity distribution is Gaussian (Maxwellian), when we know from mass/orbit modeling theory that velocity anisotropy creates non-Gaussian distributions for $v_{\rm los}$ [271], so that the shape of the l.o.s. velocity distribution actually helps to lift the mass-anisotropy degeneracy of the Jeans equation and thus obtain more accurate masses. We estimate that this induces another 0.1 dex uncertainty in the J-factor.

These systematic biases and uncertainties impact significantly the determination of the J-factor, and should be $\gtrsim 1$ dex. See Ref. [272] for further details and discussion.

2.3.5 Galaxy clusters

Clusters of galaxies present very high mass-to-light ratio environments and should be also considered primary targets for indirect DM searches both for decay and annihilation. However, the empirically-measured mass profile of galaxy clusters is derived from a combination of X-ray temperature profile and gas kinematics assuming hydrostatic equilibrium for nearby clusters. The DM halo of galaxy clusters harbor an abundance of DM substructures, with the most massive ones hosting a galaxy, which contributes to the overall DM luminosity of the clusters. They provide in principle a substantial contribution to the DM annihilation signal. However, large uncertainties in the substructure boost factors remain [148] making them less favored environments for annihilating DM as previously thought [273, 274].

Despite the fact that galaxy clusters are located at much further distances than the dwarf spheroidal galaxies around the Milky Way, the higher annihilation luminosity of clusters with the substructure contribution included could make them comparably good targets for indirect detection of DM. The flux of gamma rays from WIMP DM annihilation in clusters of galaxies is possibly large enough to be detected by current gamma-ray telescopes [275, 273]. However, standard astrophysical scenarios have been proposed for gamma-ray emission (see Ref. [276] for a review), in particular, collisions of intergalactic cosmic rays and target nuclei from the intracluster medium, that may give rise to a challenging gamma-ray background.

Cosmic-ray versus dark matter-induced emission

Galaxy clusters are expected to harbor a significant population of relativistic cosmic-ray protons originating from different sources, such as large-scale shocks associated with accretion and merger processes [277, 278], or supernovae [279] and active galactic nucleus activity [280]. The gamma-ray emission arising from pion decays produced by the interaction of these cosmic-ray protons with the intracluster gas may be a potential astrophysical background to the DM-induced gamma-ray signal. However, the cosmic-ray induced luminosity in clusters is expected to trace the gas density and therefore more centrally-concentrated than an expected dark matter annihilation signal. In the case of Coma, the authors in Ref. [275] showed that such astrophysical background is expected to be higher than the DM annihilation signal. On the other hand, the same study ranked

Fornax as the most luminous cluster in DM-induced gamma-ray emission among a sample of 106 clusters from the HIFLUGCS catalog [281]. The DM-to-cosmic-ray gamma-ray flux ratio of Fornax was predicted to be larger than 100 in the GeV energy range [275] . An independent study [274] has also predicted Fornax to be among the brightest DM galaxy clusters with a favorably low cosmic-ray induced signal. Although the central galaxy of the Fornax cluster, NGC 1399, is a radio galaxy and could in principle emit gamma-rays, the supermassive black hole at the center of this galaxy has been shown to be passive [282]. Indeed, recent observations of several clusters with the Fermi-LAT detector have shown no gamma-ray signal [283], and stringent limits on DM annihilation were derived from the Fornax observations [284].

Substructure contribution

Cosmological N-body simulations suggest the presence of DM substructures in the form of self-bounded overdensities within the main halo of galaxies. A quantification of the substructure flux contribution to the total gamma-ray flux was computed from the Aquarius simulation in Ref. [273] using a NFW profile as the DM density distribution of the smooth halo. The substructure boost depends on the integration angle for the DM signal and crucially on the minimum mass assumed for the substructures [285]. Assuming a minimum mass of 10^{-6} $M_{\odot}$, the enhancement factor can be as large as 100 for 1° integration angle.

A key-ingredient to carefully estimate the enhancement from substructures in the overall DM signal from a given object is the halo concentration. The properties of the DM halo depend on its formation epoch. A flattening of the concentration-mass relationship for CDM halos is obtained towards low masses. The annihilation luminosity being a strong function of the concentration, the flattening decreases the contribution of the smallest substructures to the DM signal. The authors of Ref. [148] derived a boost of about 20 for a virial cluster mass $M_{200} \simeq 10^{15}$ $M_{\odot}$. Like the dSphs, galaxy clusters are localized in space, and their dark matter distributions can be robustly measured from astronomical data sets.

From the measured mass distributions and known distances of galaxy clusters, several studies ranked Fornax, Coma, and Virgo clusters as the brightest source of gamma rays from dark matter annihilation. However, the detectability of a DM-induced gamma-ray signal with a thermal relic cross section is strongly depend on the substructure contribution of the overall flux (see Sec. 3.5).

2.4 Imaging Atmospheric Cherenkov telescope arrays

This section provides a brief overview of gamma-ray astronomy with Imaging Atmospheric Cherenkov telescope detection technique. Several excellent reviews have been written, see, for instance, Refs. [286, 287, 288, 289].

2.4.1 TeV gamma-ray astronomy

The detection of VHE gamma rays with ground-based atmospheric Cherenkov telescopes is nowadays a proven technique to probe non-thermal phenomena in the Universe. TeV gamma-ray astronomy studies astrophysical sources of photons from a few ten GeV up to several ten TeV, commonly referred to as the very high energy (VHE) domain. The TeV energy window has been the last window to be opened with the detection in 1989 of the first source, the Crab nebula [290]. Since then, the progress has been impressive with the detection of more than 180 VHE sources as of early 2019 [291]. TeV astronomy is a mature research field and VHE gamma-rays are found to be useful probe of the interactions of highly relativistic particles with ambient matter or radiation fields. VHE gamma-rays allow us to study the processes of particle acceleration and propagation in the universe, and examine the extreme environments in which they occur. Gamma-ray astronomy provides a unique tool to address many astrophysical topics, such as the extragalactic background photon fields and intergalactic magnetic fields through their imprint on the measured properties of distant gamma-ray sources, as well as to address fundamental physics questions by looking for signatures of dark matter, axion-like particles or Lorentz invariance violation.

Ongoing experiments currently yield a wealth of exciting results including the detection of new classes of TeV emitters such as starburst galaxies [292, 293] or globular clusters [294], and the detection of a hadronic accelerator in the Galactic Center [295]. Ground-breaking results in the quest for the origin of cosmic rays and in fundamental physics have been reported with the detection of VHE gamma-rays such as the recent detection of the first Galactic *PeVatron* [296], tests of Lorentz invariance [297], the gamma-ray opacity of the universe [298] and dark matter [299, 300, 301]

2.4.2 Detection principle and data analysis technique

While the Earth's atmosphere is transparent to radio and optical photons, all electromagnetic radiations of energies above 10 eV are effectively blocked. One can successfully pursue VHE gamma-ray observations from the ground using the

atmosphere as a calorimeter by the detection of the cascading products of the gamma-ray interaction in the upper atmosphere. The pair-produced electrons and positrons interact with air molecules and can also produce secondary gamma rays via bremsstrahlung. This process induces an electromagnetic cascade of particles that are tightly bunched along the projection of the incident primary gamma-ray trajectory. The electromagnetic cascade will be accompanied by a shower of Cherenkov photons produced by sufficiently energetic electrons and positrons[1], which will suffer little from atmospheric absorption. Although the fraction of energy that goes into the optical emission is small, a light detector comprising mirrors, phototubes and fast pulse counting electronics provides a working technique for detecting the cascade and therefore the primary gamma ray. Figure 2.7 shows a sketch of the principle of ground-based Cherenkov telescope technique.

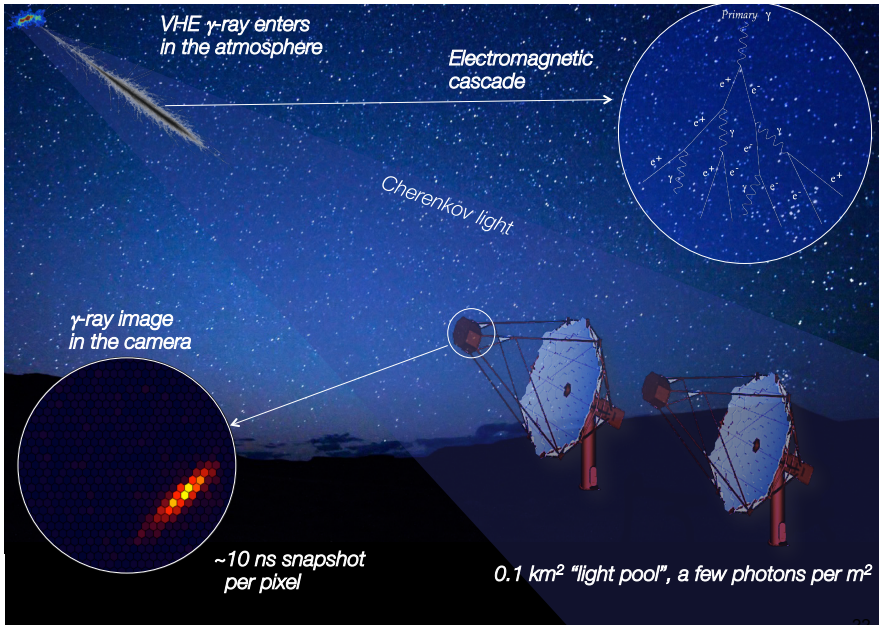

Figure 2.7: *Schematic of the detection principle of a VHE gamma ray with imaging atmospheric Cherenkov telescopes. The Cherenkov flash induced by the electromagnetic cascade can be measured by several telescopes provided they are located in the light pool. Credit: CTA consortium.*

Hadronic and electromagnetic cascades produce different Cherenkov-light patterns on ground as shown in Fig. 2.8. While electromagnetic showers produced by gamma-rays, positrons and electrons are regular, hadronic showers are irregular

[1]The production threshold of the Cherenkov emission is about 40 MeV at ∼10 km in the atmosphere.

due to the presence of sub-showers induced by particles with high transverse momenta produced in hadronic interactions. For 1 TeV gamma-ray, the maximum development of the shower occurs at a depth of about 300 gcm^{-2} which corresponds to an altitude of 10 km above sea level for a vertical incident gamma-ray, and the shower is fully contained in the atmosphere. The Cherenkov light yield is proportional to the total track length of all particles, and thus proportional to the primary gamma-ray energy. An image of the cascade provides a pseudo-calorimteric measurement of the shower energy. The Cherenkov light opening angle is $\sim$1° in air and the Cherenkov photons produced around the shower maximum arrive at observation heights of $\sim$2000 m a.s.l. in a $\sim$120 m radius light pool. The photoelectron density is $\sim$100 m^{-2}TeV^{-1}. Given the typical instrumental efficiency of 10% (reflectivity of mirror and quantum efficiency of photomultipliers) 100 m^{2}optical reflector are required to obtain $\sim$100 photoelectrons in the shower image for 100 GeV γ-ray. The Cherenkov light flash lasts a few nanoseconds and fast photomultipliers and electronics are needed to extract this faint and short signal over the night sky background light.

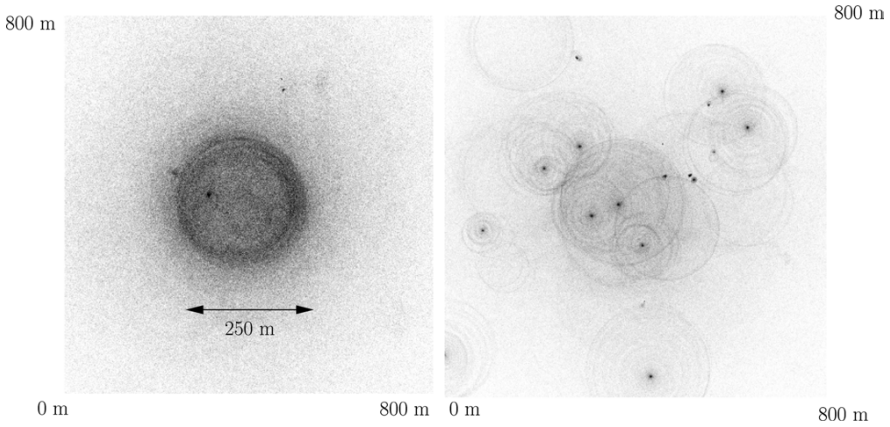

Figure 2.8: *Cherenkov light distribution on ground for a 300 GeV gamma-ray shower (left panel) and a 1 TeV proton shower (right panel), derived from Monte Carlo simulations. The side length is 400 m. The pictures are extracted from Ref. [302].*

A multiple view of the same air shower proves very useful to improve angular and energy resolutions as well as background discrimination as first demonstrated by the HEGRA collaboration [303]. A multi-telescope trigger system is able to efficiently reject most of the muons and hadrons initiated showers. At the analysis level, the stereoscopic view improves the reconstruction of the direction and energy of the primary gamma-ray. Although the shower axis reconstruction is possible with a single telescope, the multiple view of the shower provides a more accurate reconstruction of the shower direction using the intersection of the di-

rections of the major axes of the images recorded in the cameras. The shower core location can also be better determined, thus improving the energy resolution. A better hadronic rejection is also obtained thanks to an improved shower geometry. In a Cherenkov telescope array, the optimal separation of telescopes is close to the radius of the Cherenkov light pool. Low-energy performances can be improved with closer spacing at the expense of effective collection area at higher energies.

Background rejection and analysis technique

The Cherenkov technique faces an overwhelming background from showers initiated by cosmic-ray protons and nuclei. For instance, the gamma-ray rate for the brightest quiescent objects detected by H.E.S.S. is only ∼0.1% of the background showers rate. Showers initiated by TeV protons and nuclei differ in many respects from gamma-ray showers. The sub-showers create substructures in the shower image detected in the camera, and the image is wider due to the large transverse momentum implied by hadronic interactions. Moreover, for a given primary energy, hadronic interactions produce less Cherenkov light, a factor of 2 to 3 times less at ∼1 TeV, due to the energy released in neutrinos, high energy muons and hadrons in the shower core. Single muons reaching the ground produce rings when impacting the telescope dish, or arc-like shape at larger impact distances. The discrimination between hadron and gamma-ray induced showers relies on the geometry of the shower image recorded in the camera. An example of shower images detected in the camera is shown in Fig. 2.9 for hadron, muon and gamma-ray events, respectively.

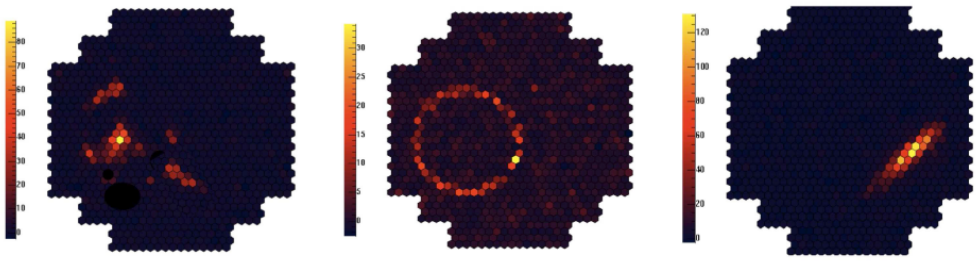

Figure 2.9: *Monte Carlo simulations of images of atmospheric events induced from cosmic particles observed in the camera placed at the focal plane of a Cherenkov telescope. From left to right: hadron-like, isolated muon and gamma-like events (courtesy J. Hinton).*

Another challenging background is the Night Sky Background (NSB) which comes form the diffuse light from stars, light pollution, atmospheric nightglow,

zodiacal light, the Moon, etc. This background can be efficiently discriminated using fast integration electronics. Typical Cherenkov flashes last several nanoseconds and the closer the time integration window the less NSB is integrated. Fig. 2.10 shows the camera images of a gamma-ray shower for integration time of 100 μs, 1 μs, and 10 ns, respectively, of the same shower. The gamma-ray image is clearly visible above NSB for a 10 ns integration window.

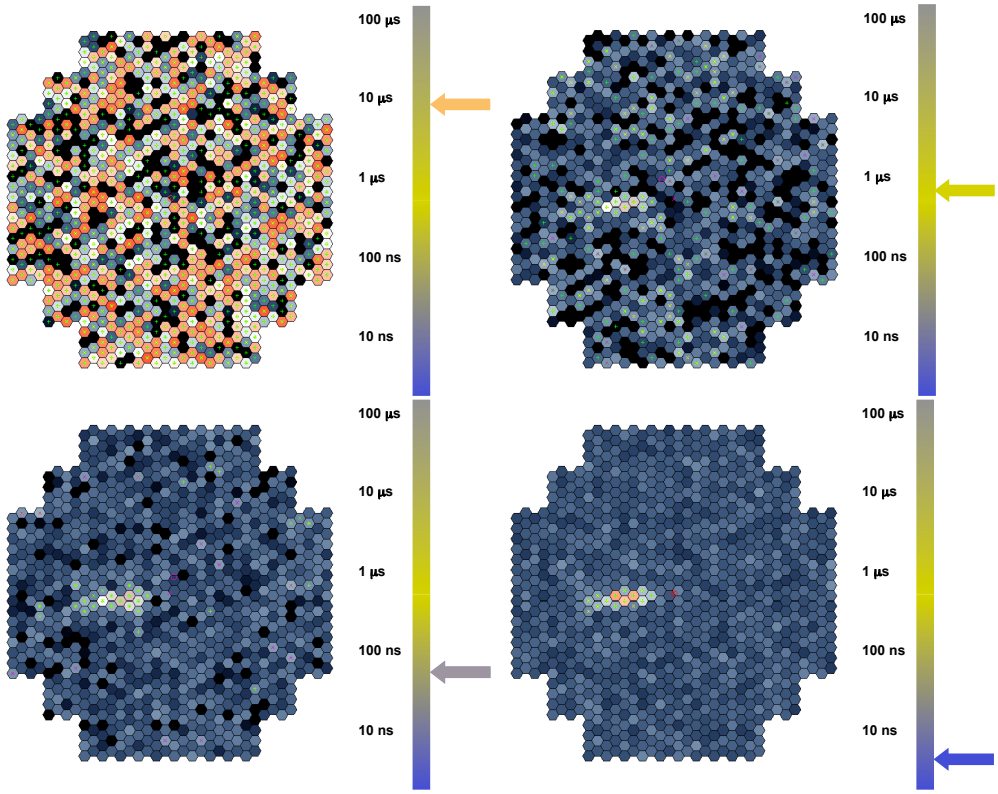

Figure 2.10: *Monte Carlo simulations of gamma-ray shower observed in the camera for acquisition times 10 µs 1 µs, 100 ns and 10 ns (courtesy K. Bernlohr).*

Once gamma-ray-like events are selected via the analysis of the pixellized image topology in the camera, some residual (misidentified) cosmic hadrons and muons together with cosmic electrons and positrons remain in the gamma-ray-like event sample. The subtraction of the isotropic part of the residual background is achieved through observations of regions in the sky where no (or significantly less) gamma ray is expected. The background is measured in control region referred as to the *OFF region* and subtracted to the signal in the *ON region* where (most of) the signal is expected. In this case observations are taken in *wobble* mode where the telescope pointing position is offset from the source depending on the spatial

extend of the expected signal and telescope field of view. For H.E.S.S., the offset is usually taken to 0.5° to 0.7° for sources of about 0.1° extension. The OFF region is selected symmetrically to the ON region from the camera centre, or in an open annulus, where the ON region and other VHE emissions are excluded, to reduce the statistical uncertainty on the background measurement. Under the reasonable assumption of azimuthal symmetry and flat exposure in the camera field of view for the acceptance, this enables a measure of the background in the same condition as for the signal. In the case of a diffuse signal with extension similar to or larger than the camera field of view (a few degrees) with no or low gradient in the emission compared to the size of the camera field of view, this method will likely subtract the extended emission and different observation techniques are required. Dedicated OFF observations, which increases the total observation time, or Monte Carlo simulations of the expected residual background, are required.

The energy scale is often calibrated using Cherenkov light from local muons. Variations in atmospheric profile, the transmission, and the orientation of the shower axis relative to the geomagnetic field can influence the shower development and the light yield. This implies a systematic uncertainty of about 10-20% in the absolute energy calibration. The atmosphere is used as a deep electromagnetic calorimeter but record only small fraction of the total energy. Intrinsic fluctuations in the shower development, shower simulation uncertainties, knowledge of the atmospheric conditions yield an overall energy resolution of about 15% with little energy dependency. The topology of the shower image in the camera together with a multiple view of the shower provides an angular resolution of 0.1°/gamma ray allowing an improved rejection of the background compared to single telescope observations. The sensitivity of the current generation of IACTs is such that the detection of the Crab Nebula is done within a minute, and a source with 1% of the Crab flux ($2 \times 10^{-13}\,\mathrm{m^{-2}s^{-1}}$ above 1 TeV) is detected in 25 h.

2.4.3 Ongoing experiments and near future

Following the successes of the Imaging Cherenkov technique pioneered by the 10 m Whipple telescope, the ground-based Cherenkov telescopes made exciting progress with the usefulness of a high-granularity camera as showed by CAT, and the use of the stereoscopic technique demonstrated by HEGRA. These substantial developments gave birth to the third generation of IACTs: CANGAROO III [304] near Woomera in Australia, H.E.S.S. [305] in the Khomas Highlands of Namibia, MAGIC [306] in the Canari island of La Palma, and VERITAS [307] in southern Arizona. The ongoing IACTs have fields of view of a few degrees and a duty cycle of about 10% imposed by the need of good weather conditions and complete

darkness[1]. Experiments are located both in Southern and Northern hemispheres allowing both simultaneous and follow-up observations of TeV sources. Table 2.1 summarises the main characteristics of currently operating IACTs. The catalog of TeV sources grew rapidly with H.E.S.S. in the southern hemisphere, which provided the first high-sensitivity VHE observations of the densely populated inner Galaxy. It has continuously expanded in recent years as MAGIC and VERITAS have come online.

The Cherenkov Telescope Array

The next-generation observatory for ground-based gamma-ray astronomy will consist of two km-sized arrays with ten to hundred Cherenkov telescopes, one in each hemisphere. The aims for CTA during the design study [308] are the following: *(i)* an order-of-magnitude increase in flux sensitivity at the milliCrab level; *(ii)* significant increase in detection area and thus detection rates, which will be crucial for observations of transient phenomena and studies at the highest energies; *(iii)* a factor of 2-to-3 increase in the angular resolution over current IACTs, resulting in resolving ability for the morphology of extended sources; *(iv)* uniform energy coverage in the range of tens of GeV to >100 TeV; and *(v)* enhanced sky survey capability, monitoring capability and flexibility of operation. The observatory will operate arrays on sites in both hemispheres to provide full sky coverage, and hence maximising the potential for the rarest phenomena such as very nearby supernova, gamma-ray bursts or gravitational wave transients. With about 100 telescopes on the southern site, very flexible operation will be possible, with sub-arrays available for specific tasks.The northern site located in Roque de los Muchachos Observatory in La Palma in the Canary Islands (Spain) will be composed of 4 large telescopes (LST) of 23 m in diameter and 15 medium telescopes (MST) of 12 m in diameter. The southern site will be installed at the European Southern Observatory Cerro Paranal in Chile and will be composed of 4 LSTs, 25 MSTs and 70 small-sized telescopes (SST). The field of view will be of $\sim 3^\circ$ for the LSTs up to $\sim 9^\circ$ for the SSTs. An artist view of the Southern site of the CTA observatory is shown on Fig. 2.11.

The scientific potential of CTA is broad [309]: from understanding the role of relativistic cosmic particles to the search for dark matter. It will cover a huge range in photon energy from 20 GeV to 300 TeV. Wider field of view and improved sensitivity will enable CTA to survey hundreds of times faster than previous TeV instruments. The angular resolution of CTA will approach 1 arcminute at high energies, the best resolution of any instrument operating above the X-ray band, allowing for a detailed imaging of gamma-ray sources. CTA will be operated as an

[1]Recently, observations under partial moonlight have been successfully performed.

Table 2.1: *Main characteristics of current IACTs, including three of historical interest. The energy threshold is given at the trigger level for observations close to the zenith. The approximate sensitivity is expressed in terms of a percentage of the flux of the Crab Nebula (*$\sim 2 \times 10^{-11}$ cm^{2}s^{-1}above 1 TeV) as the minimum flux of a point-like source detectable at the 5σ level in a 50 hours observation time. [a]A second telescope has recently being completed. The sensitivity is expected to be improved by a factor of $\sim$3 with the stereo operation. [b] This instrument has pixels with different sizes.

Instrument	l (deg.)	b (deg.)	Alt. (m)	# of telescopes	Telescope area (m^2)	Pixels /camera	FoV (deg.)	Threshold (GeV)	Sensitivity (% Crab)
H.E.S.S. CT1-4 / CT5 II	-23	16	1800	5	107/600	960/2048	5/3.5	100/30	0.7
MAGIC I+II	29	18	2225	2	234	574/1039[b]	3.5	60	1.0
VERITAS	32	-111	1275	4	106	499	3.5	100	0.7
CANGAROO-III	-31	160	160	3	57.3	427	4	400	15
Whipple	32	-111	2300	1	75	379	2.3	300	15
HEGRA	29	18	2200	5	43	271	4.3	500	5
CAT	42	2	1650	1	17.8	600	4.8	250	15

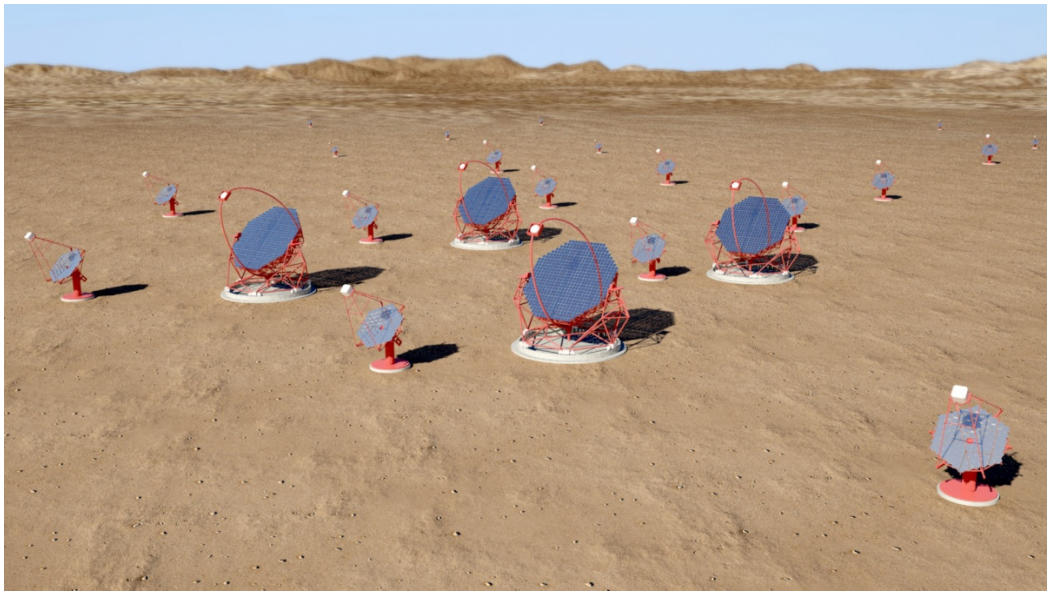

Figure 2.11: *An artist view of the Cherenkov Telescope Array (CTA) observatory with three telescope sizes (large 23 m ⌀, medium 12 m ⌀, small 4-6 m ⌀) for an energy coverage from a few 10 GeV to a few 100 TeV.*

open, proposal-driven observatory. Data available will be publicly released after a one-year proprietary period. The consortium has prepared a core programme using 40-50% of the available observing time in the first ten years of operation focusing on highly motivated observations. Key Science Programs include the search for dark matter, transients, acceleration up to PeV energies in our own galaxy. CTA will also conduct ambitious surveys with quarter-sky extragalactic, full-plane Galactic and Large Magellanic Cloud surveys planned. The input of CTA for TeV dark matter search in specific astrophysical environments will be scrutinized throughout the chapter 3.

Chapter 3

Heavy WIMP searches and prospective studies

Contents

This chapter presents a brief overview of the main results of the searches in which I was involved looking for WIMPs. They have been performed with H.E.S.S. observations. Prospective studies have been carried out for the upcoming CTA observatory. Many of the CTA prospective studies served to elaborate the dark matter programme of CTA published in Ref. [309]. A significant part of the studies shown here has been carried out during the PhD theses of Aion Viana [310], Valentin Lefranc [311] and Lucia Rinchiuso [312].

Ground-based Cherenkov telescopes are ideally suited for targeted searches, *i.e.* to look for dark matter signals in astrophysical objects with known locations. With large collection area and efficient residual background rejection with simultaneous measurements of signal and background, they are very well suited for deep observations of selected sources. Targeted searches belong to the long-term dark matter programs led with ongoing IACTs. Observation campaigns with H.E.S.S. have been conducted towards a variety of environments, *i.e.* the Galactic Centre, Galactic globular clusters, dwarf galaxy satellites of the Milky Way and nearby clusters of galaxies, to look for a dark matter signal.

At first sight, ground-based Cherenkov telescopes do not seem well suited for non-targeted searches, *i.e.* searches towards substructures in the Galactic halos, due to their fields of view limited to a few degrees and the random nature of the possible dark matter substructure positions in the sky. Space-based instruments such as the Fermi satellite can perform much more easily blind searches for DM subhalos with a regular scanning of the entire sky thanks to their large field of view. However, with long-enough exposure and adequate survey strategy, the very good flux sensitivity achieved with the IACT technique make possible to seek efficiently for dark matter annihilations in substructures such as intermediate mass black holes or subhalos as predicted to be harbored in the Milky Way halo.

3.1 The inner Galactic halo

As discussed in Sec. 2.3.1, the Galactic Center is arguably the prime target to detect dark matter in VHE gamma rays and can be observed under favorable conditions by H.E.S.S. due to its location in the Southern hemisphere. However, the Galactic centre harbors a wealth of sources that shine at high and very-high gamma-ray energies (see Chap. 4).

3.1.1 10 years of observations with H.E.S.S. I

The dataset towards the Galactic Centre regularly increased with the regular observation campaigns performed since 2004. The legacy results from H.E.S.S. phase I makes use of 254 hours (live time) of high-quality data of GC observations

during the years 2004-2014. Given the H.E.S.S.-I observation strategy of the GC and the time exposure map, a DM signal can be searched within 1° of the GC. The latest data analysis method developed to search for a dark matter annihilation in the GC region makes use of both the spectral and spatial information of the DM signal with respect to background with a 2-dimensional binned Poisson maximum likelihood analysis, see Refs. [311, 312]. 70 logarithmically-spaced energy bins from 160 GeV to 70 TeV and seven spatial bins corresponding to RoIs defined as the above-mentioned annuli of 0.1° width, have been used. Specific background measurement technique have been developed to select background events for each observation, *i.e.* allowing for signal and background measurements in the same instrumental and atmospheric conditions which does not require any further offline correction [311, 312][1]. A gradient in the expected dark matter signal is required between the signal and background regions. No significant gamma-ray excess with respect to the expected background is obtained. Constraints expressed as upper limits on $\langle\sigma v\rangle$ are obtained from the likelihood ratio test statistic given by $\mathrm{TS} = -2\ln(\mathcal{L}(m_{\mathrm{DM}}, \langle\sigma v\rangle)/\mathcal{L}_{\max}(m_{\mathrm{DM}}, \langle\sigma v\rangle))$, which, in the high statistics limit, follows a χ^2 distribution with one degree of freedom [314]. Values of $\langle\sigma v\rangle$ for which TS is higher than 2.71 are excluded at 95% confidence level (C.L.).

Constraints are derived on $\langle\sigma v\rangle$ for WIMPs from hundred GeV up to several ten TeV in various annihilation channels. The left panel of Fig. 3.1 shows the 95% C. L. observed upper limits for the $\mathrm{W^+W^-}$ channel and the Einasto profile. The expected limits are obtained from 1000 Poisson realizations of the background obtained through observations of blank fields at high latitudes where no signal is expected (see Supplemental Material of Ref. [300] for details.). The mean expected upper limit together with the 68% and 95% containment bands are plotted. The limits reach 6×10^{-26} $\mathrm{cm^3 s^{-1}}$ for a DM particle of mass 1.5 TeV. A factor of five improvement is obtained compared with the results of Ref. [299]. The larger dataset and the improved data analysis method contribute to the increase of the sensitivity of the analysis presented here. In the right panel of Fig. 3.1, the observed 95% C. L. upper limit is shown for the $\tau^+\tau^-$ channel together with expected limits. The limits reach $\langle\sigma v\rangle$ values expected for thermal relic density. The left panel of Fig. 3.2 shows a comparison with the current constraints obtained from the observations of the MAGIC ground-based Cherenkov telescope instrument towards the Segue 1 dwarf galaxy [315][2], the combined analysis of 4 dwarf galaxies observed by H.E.S.S. [316], and the observations of 15 dwarf galaxy satellites of the Milky Way by the Fermi satellite [317]. A

[1] This method is found to be very performant in terms of control of the background measurement but fails to probe extended (several hundred parsec) DM core at the GC. An alternative observation strategy is required such as shown in Ref. [313].

[2] Note that the J-factor of Segue 1 can be significantly overestimated in Ref. [315], a factor of 100 at least according to Ref. [255].

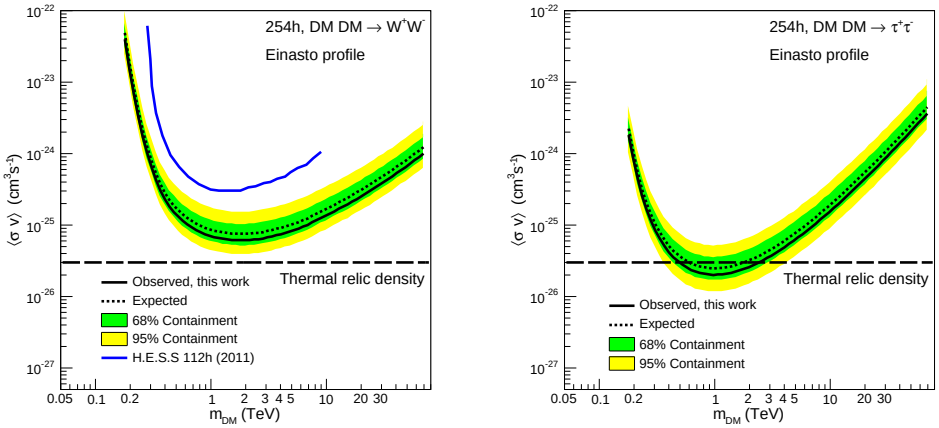

Figure 3.1: *Constraints on the velocity-weighted annihilation cross section $\langle\sigma v\rangle$ for the W^+W^- (left panel) and $\tau^+\tau^-$ (right panel) channels derived from 10 years of observations of the inner 300 pc of the GC region with H.E.S.S. The constraints are expressed as 95% C. L. upper limits as a function of the DM mass mDM. The observed limit is shown as black solid line. The expectations are obtained from 1000 Poisson realizations of the background measured in blank-field observations at high Galactic latitudes. The mean expected limit (black dotted line) together with the 68% (green band) and 95% (yellow band) C. L. containment bands are shown. The blue solid line corresponds to the limits derived in a previous analysis of 4 years (112 h of live time) of GC observations by H.E.S.S. [299]. The horizontal black long-dashed line corresponds to the thermal relic velocity-weighted annihilation cross section (natural scale). Figure extracted from Ref. [300].*

velocity-weighted annihilation cross section of 6×10^{-26} cm^{3}s^{-1} for DM particles with a mass of 1.5 TeV annihilating in the W^+W^- channel are excluded for an Einasto profile. The H.E.S.S. constraints are the most constraining limits obtained so far in the TeV mass range for cuspy Dark matter profiles. The constraints surpass the Fermi limits for particle masses above 400 GeV in the W^+W^- channel. The strongest limits are obtained in the $\tau^+\tau^-$ channel at 2×10^{-26} cm^{3}s^{-1} for a DM particle mass of 1 TeV. For the first time, observations with a ground-based array of imaging atmospheric Cherenkov telescopes are able to probe the thermal relic annihilation cross section in the TeV DM mass range. The right panel of Fig. 3.2 shows the 95% C.L. velocity-weighted annihilation cross section $\langle\sigma v\rangle$ for the prompt annihilation into two photons from H.E.S.S. They reach $\sim 4\times10^{-28}$ cm^{3}s^{-1} for 1 TeV DM mass for the Einasto profile.

The constraints obtained from H.E.S.S.-I observations of the Galactic Centre are the most constraining so far in the TeV mass range. Fermi-LAT and H.E.S.S.

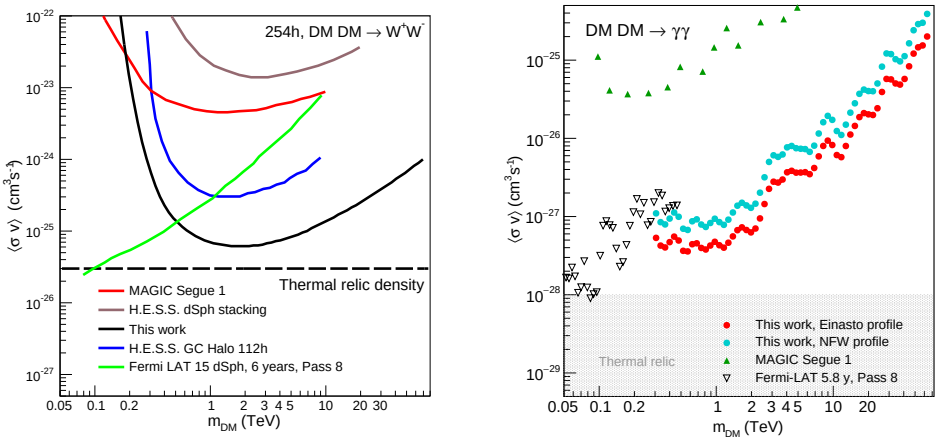

Figure 3.2: ***Left panel:*** *Comparison of constraints on the W^+W^- channels with the previous published H.E.S.S. limits from 112 hours of observations of the GC [299] (blue line), the limits from the observations of 15 dwarf galaxy satellites of the Milky Way by the Fermi satellite [317] (green line), the limits from 157 hours of observations of the dwarf galaxy Segue 1 [315] (red line), and the combined analysis of observations of 4 dwarf galaxies by H.E.S.S. [316] (brown line). Figure extracted from Ref. [300].* ***Right panel:*** *Comparison of constraints on the velocity-weighted annihilation cross section $\langle\sigma v\rangle$ for the prompt annihilation into two photons derived from H.E.S.S. observations taken over ten years (254 h of live time) of the inner 300 pc of the GC region. The constraints are expressed in terms of 95% C. L. upper limits as a function of the DM mass m_{DM} for the Einasto (red dots) and NFW (cyan dots) profiles, respectively, with the limits from the observations of the Milky Way halo by Fermi-LAT [318] (black triangles) as well as the limits from 157 hours of MAGIC observations of the dwarf galaxy Segue 1 [315] (green triangles). The grey-shaded area shows the natural scale for a monochromatic gamma-ray line signal. Figure extracted from Ref. [301].*

constraints together cover more than four orders of magnitude in mass.

3.1.2 Searches with Inner Galaxy Survey with H.E.S.S. II

The current searches with H.E.S.S. towards the inner Galactic halo benefit from additional observations of the phase 2 of H.E.S.S. with an energy threshold lowered down to several tens of GeV and improved sensitivity in the TeV energy range. The H.E.S.S. collaboration is performing a survey of the inner few degrees of the Galactic Centre in order to provide unprecedented sensitivity to dark matter signals in the central region of the Galactic halo, studying in greater details the central diffuse emission, and searching for TeV outflows

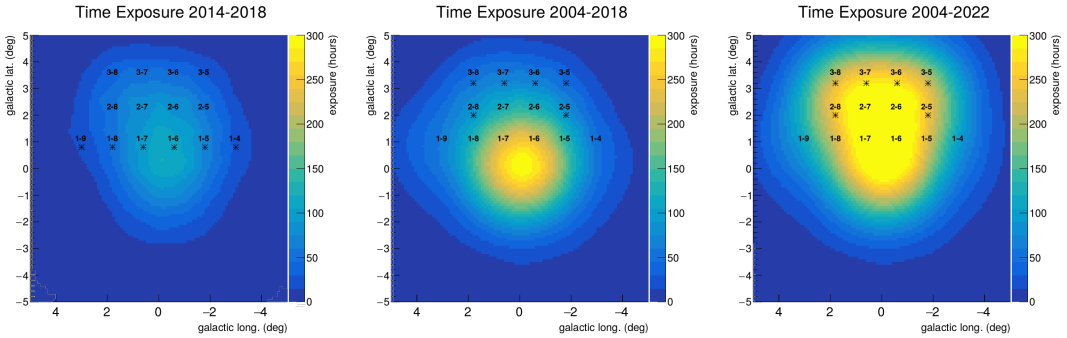

Figure 3.3: *Galactic Centre time exposure map in Galactic Coordinates.* ***Left panel:*** *2014-2018 exposure map from H.E.S.S. II IGS observations. The selected 14 pointings positions of the IGS are marked as black crosses.* ***Middle panel:*** *Current 2004-2018 exposure map from cumulated H.E.S.S.-I and H.E.S.S.-II IGS observations.* ***Right panel:*** *Projected exposure in 2022 from cumulated H.E.S.S.-I and H.E.S.S.-II IGS observations. Figures extracted from Ref. [312].*

from the Galactic Centre (See Chap. 4). The Inner Galaxy Survey (IGS) is a key-science programme for H.E.S.S., which could bring among the last H.E.S.S. high-impact results, even discoveries, before the advent of the CTA-South observatory. The observation programme is a multi-year effort started in 2016 with observation proposal follow-ups and re-evaluation on year-by-year basis. The aim of the IGS is to pursue an extended survey of a region around the Galactic Center at positive Galactic latitudes with telescope pointing position extending up to 3° in the most unbiased way possible. More than 400 hours of observations have been taken with H.E.S.S. II so far. Further details on the IGS can be found in Ref. [312]. Such a survey is the first being carried at VHE gamma-ray energies.

Fig. 3.3 shows the exposure map from 2014-2018 IGS observations (left panel) and the 2004-2018 exposure map (middle panel) from cumulated H.E.S.S.-I and H.E.S.S.-II IGS observations. The right panel of Fig. 3.3 shows the foarecast Galactic Centre exposure map expected in 2022 assuming the continuation of the IGS until 2022 with 100 h/year observations on the pointing positions 2-5, 2-8 and 3-x from 2019 to 2021.

Such a survey currently out by the H.E.S.S. collaboration is crucial both for the search for dark matter and the understanding of the origin of the Galactic cosmic rays at the highest energies. It is the first ever performed in the Galactic Center region in VHE gamma rays.

3.1.3 Prospective studies with CTA

The next-generation IACT is the Cherenkov Telescope Array (CTA) that is conceived to surpass the overall performances of the present IACTs. The CTA sensitivity to DM annihilation is expected to provide a substantial improvement in the flux sensitivity compared to current IACTs up to one order of magnitude [113, 319, 309]. The inner Galactic halo is a key target for CTA with more than 800 hours planned in the inner 5 degrees of the Galactic Centre. These observations towards the inner Galactic halo will provide statistically rich observational datasets.

These datasets will result from the combination of multiple observations with distinct observational parameters that will likely introduce specific observational systematics. Since the systematic errors may be the limiting factor in the error budget for CTA, an assessment of their impact in the CTA sensitivity is currently studied. A possible way to investigate the impact of such uncertainties is to introduce in the likelihood a Gaussian nuisance parameters [320]. The left panel of Fig. 3.4 shows the impact of the systematic uncertainty versus the statistical uncertainty only, on the sensitivity computed at 95% C.L.[1]. The sensitivity is deteriorated over all the mass range for a given observational time. In particular, introducing a systematic error of 0.3%(3%) for 100 hours, deteriorates the sensitivity of a factor 1.5.

Given the higher flux sensitivity of CTA, new emissions may be detected in this very crowded region of the Galactic Center, with numerous astrophysical emitters that may shine in the VHE gamma-ray regime. In particular, the Galactic Diffuse Emission (GDE) detected by the Fermi-LAT satellite [321, 322, 323] originating mainly from mostly by decays of the π^0 produced in proton-proton collisions in the interstellar medium and inverse Compton scattering of energetic electrons off the ambient radiation fields, may be an additional gamma-ray background for Dark matter searches the CTA energy range. Spectral and spatial features of the searched dark matter signals and GDE can be used for discriminating between these components [113]. Since above the CTA threshold the gamma-ray contamination is not fully understood, an *isotropic* flux for GDE all over the RoIs is assumed here. See Ref. [113] for further discussions. With this "extreme" choice, we are clearly overestimating the GDE, because it is reasonable to expect that the diffuse γ-ray contamination decreases as a function of the distance from the Galactic Center. As a consequence, our results is conservative from the point of view of GDE uncertainties. The middle panel of Fig. 3.4 shows the deterioration of the CTA sensitivity once an "extreme" GDE is added to the residual

[1]The sensitivity is defined as the mean upper limits, see Ref. [113] for further details on the procedure. Note that this procedure assumes uncorrelated systematics which is the most pessimistic case and provides the largest possible impact on the deterioration of the sensitivity.

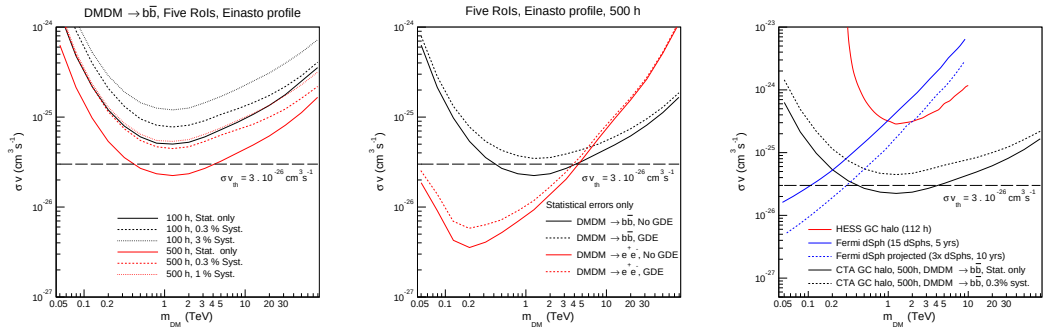

Figure 3.4: *CTA sensitivity to DM annihilation in the* ($m_{\rm DM}$, $\langle\sigma v\rangle$) *plane. Unless otherwise stated, our morphological analysis employs five adjacent RoIs, the exposure in each RoIs is 500 h, the energy threshold is 30 GeV and only the statistical uncertainties are taken into account.* ***Left panel:*** *Degradation of the CTA sensitivity for annihilating DM into* $\bar{b}b$ *pairs due to possible systematic errors in the rich observational datasets. Observation times of 100 h (black lines) and 500 h (red lines) assuming different values of systematics: 0.3% (dashed lines), 3% (dotted lines), only statistical fluctuations (solid lines) are taken into account.* ***Right panel:*** *Impact of an "extreme" GDE added on top of the CR background, on the CTA sensitivity. The sensitivity is shown for annihilating DM into* $\bar{b}b$ *(back lines) and* e^+e^- *(red lines) pairs with (dotted lines) and without (solid lines) the irreducible GDE background. See the text for further details.*

CR background for an observation time of 500 h and DM particles annihilating into $\bar{b}b$ (back lines) and e^+e^- (red lines) pairs. The CTA sensitivity still probes cross section below the thermal value for the e^+e^- channel. For the hadronic ones (e.g. $\bar{b}b$ mode), the CTA sensitivity is degraded of a factor 2 making the reach of the thermal cross section no longer possible. Nevertheless, since we assume that the GDE is *isotropic*, it is worth stressing again that we are overestimating the γ-ray contamination in all RoIs. In fact, if we consider an accurate mapping of the GDE in our RoIs (like the one used in Ref. [319] in their *optimistic scenario*), we find that the impact of the GDE in the final results is not very pronounced. This comes from to the fact that in all the regions used in our analysis, the diffuse γ-rays contamination is smaller than the residual CR background extracted from a full CTA Monte Carlo simulation.

The CTA sensitivity to DM annihilations is computer in several primary channels and low energy contributions of the γ-rays fluxes due to inverse Compton Scattering (ICS) on the ambient photon background of the $e^{\pm}$ from annihilating DM are taken into account. This is particularly relevant for the determination of the CTA sensitivity in the leptonic channels, especially for the DM DM $\rightarrow e^+e^-$ mode. The ICS emission substantially increases the CTA sensitivity for the lep-

tonic channels. Given the spectral features of the ICS emissions, the total fluxes receive a substantial contribution for photon energy just below the DM mass in case of leptonic channels (especially for the DM DM $\rightarrow e^+e^-$ and $\mu^+\mu^-$ modes). As a consequence, since the IC secondary emission is well inside the CTA energy window, the sensitivity to those channels is largely ameliorated. Focussing first on the purely leptonic channels, CTA would be able to exclude annihilation cross sections well below the thermal value. On a more specific level, the best sensitivity is obtained for the DM DM $\rightarrow e^+e^-$ mode ($\langle\sigma v\rangle \lesssim 5 \times 10^{-27}$ cm^3/s for m$_{DM} \simeq 200$ GeV) rather than $\mu^+\mu^-$ and $\tau^+\tau^-$, since the original $e^\pm$ population is produced at higher energies, and therefore the secondary ICS emission is well inside the CTA energy window. For the hadronic and W^+W^- channels, we get the same qualitative feature of the exclusion limits modulo a factor of $\mathcal{O}$(few) in the normalization. This can be explained by the fact that the γ-ray spectrum arising from the fragmentation of sufficiently heavy hadronic SM particles is quasi-universal. In particular, for the DM DM $\rightarrow b\bar{b}$ channel the thermal value of the cross section can be probed in the TeV mass range, where the best sensitivity is achieved at $\sigma v \simeq 2 \times 10^{-26}$ cm^3/s for m$_{DM} \simeq 1$ TeV.

The right panel of Fig. 3.4 shows the constraints for the DM DM $\rightarrow \bar{b}b$ channel with respect to the best limits to date obtained from either other analyses or targets. In particular the CTA sensitivity with no GDE and systematics will be roughly a factor 10 more sensitive for DM masses around 1 TeV. With respect to the stacking analysis on 15 dwarf Spheroidal galaxies (dSph) observations from FERMI-LAT [324], CTA becomes competitive for energies above 100 GeV and it overtakes the FERMI-LAT constraint for DM masses above 200 GeV. Furthermore, it is important to point out that CTA will still provide stronger limits above roughly 500 GeV, if the optimistic scenario of 45 observed dSphs for 10 years FERMI observations [324] will be considered. Hence, together with the optimistic FERMI observations of dSphs, CTA will be able to survey thermal DM candidates in a broad range of masses, from few hundred GeV up to several tens of TeV.

CTA observations of the Galactic centre region could be decisive for the thermal TeV-ish WIMP model provided that the instrumental/observational systematic uncertainty can be controlled to a level significantly better than what is currently achieved with ongoing IACTs.

3.1.4 Searches for Wino and Higgsino dark matter

If annihilation signal exists, the highest photon statistics is likely to be found in the Galactic Center of the Milky Way. Fortunately, the astrophysical backgrounds tend to have broad smooth spectra, which implies that the cleanest and

most convincing signal of DM annihilation in gamma rays would be a distinctive feature such as a spectral line. As shown in Sec 3.1, VHE analyses have placed strong model-independent limits on spectral lines using H.E.S.S. observations of the GC region.

Dark matter models which exhibit prominent line features in their gamma-ray annihilation signals include the prototypical and longtime-discussed Wino and Higgsino candidates. The Wino model is defined by extending the standard model by a single new electroweak triplet fermion with zero hypercharge, and the name wino refers to the fact that this particle is identical to the superpartner of the electroweak bosons. The Wino is a compelling target both due to the fact that it is arguably the simplest model of weakly interacting dark matter [85], and that it also could be the lightest superpartner, *e.g.* [325, 326, 327, 328]. Because its interactions are determined by the gauge structure of the Standard Model, the pure wino is highly predictive, since the DM mass is the only additional parameter relevant to phenomenology. In addition, one can require that the thermal relic abundance agrees with the measured value, implying a mass of ~ 3 TeV [329, 330, 331]. Maintaining the assumption of a thermal history, lower-mass winos can constitute a subdominant fraction of the DM, or a non-trivial cosmology can be invoked so that lighter winos could be all the DM. Higher-mass winos are potentially viable DM candidates if their production and depletion mechanisms in the early universe differ from standard assumptions. Besides the continuum emission of photons resulting from the decay of final state W and Z bosons, the latest computation Wino annihilation spectrum in gamma ray include: *(i)* the Sommerfeld enhancement, where a significant correction to the cross-section arises from the potential generated by the exchange of electroweak particles between the wino states; *(ii)* the resummation of Sudakov logarithms which become significant when the DM mass is well above the scale of the electroweak particles which mediate the annihilation; and *(iii)* the endpoint photons, which have $E = zm_{\rm DM}$ with $1 - z \ll 1$. At any instrument with finite energy resolution, such as CTA, these photons can become indistinguishable from the line associated with the two body final state where $z = 1$. See Ref. [332] for further details.

In the case of the Higgsino, a full calculation involving all relevant effects has not yet been performed. Partial results do exist, including the full Sommerfeld calculation [333]. The work in [334] demonstrated that the resummed endpoint contribution for the Higgsino is likely to be crucial, and to lead to a large $\mathcal{O}(1)$ correction. In what follows, just the tree-level annihilation rate, supplemented with the Sommerfeld enhancement, to produce both line photons and continuum emission are considered. In the Higgsino case, there are two additional parameters which must be specified beyond the DM mass, namely the splittings between the charged and neutral states, δm_+ and δm_N. If the splittings were purely radiative in the Higgsino case, the neutral states would be of equal mass ($\delta m_N = 0$)

and would both contribute to the DM, allowing for tree-level scattering between DM and visible particles via Z exchange. This scenario is strongly excluded by constraints from direct detection; evading this limit requires the heavier neutral state to be kinematically inaccessible in direct-detection experiments, suggesting $\delta m_N \gtrsim 200$ keV for TeV-scale DM. Such small splittings can be easily induced in supersymmetric scenarios by a tiny mixing of the Higgsino with the heavier neutralinos. For the Higgsino, consequently, there is a wide space of possible mass splittings. Given that our Higgsino spectrum is representative and not exact, two representative values following [334] are considered.

H.E.S.S. sensitivity to Wino

A realistic mock H.E.S.S.-like dataset of VHE observations of the Galactic Centre region has been carried out in Ref. [335]. Using the latest results from modern effective field theory techniques to obtain a precise calculation of the full photon energy spectrum from wino annihilation [336, 332], the implications have been explored using mock H.E.S.S. sensitivity expectations [335].

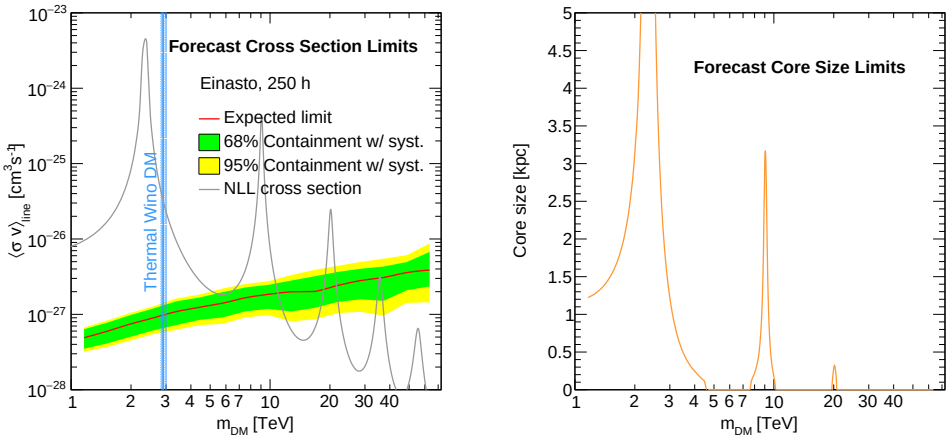

Figure 3.5: ***Left panel :*** *95% C.L. mean expected upper limits on the thermally-averaged velocity-weighted annihilation cross section $\sigma v_{\rm line}$ as a function of the DM mass mDM, together with statistical 68 and 95% containment bands including the systematic and theoretical uncertainties. The mass corresponding to a thermally-produced wino dark matter $m_{\rm DM} \simeq 2.9 \pm 0.1$ TeV is shown as a light blue vertical band. The NLL cross section for wino DM is shown in gray.* ***Right panel :*** *Mean expected lower limits at 95% C.L. on the DM core size at the Galactic Centre as a function of the DM mass $m_{\rm DM}$, required to save the wino model. Figures extracted from Ref. [335].*

The left panel of Fig. 3.5 shows the H.E.S.S. sensitivity expressed as 95%

C.L. mean expected upper limits on the velocity-weighted annihilation cross section $\langle \sigma\, v \rangle_{\rm line}$ as a function of the wino mass assuming ROIs up to 1° as used in the analysis results shown in Sec 3.1. Strong constraints could be derived from H.E.S.S. observations in case of a cuspy dark matter profile. The thermal Wino mass can be probed for a cuspy dark matter profile. The uncertainties are presently dominated by the experimental systematic uncertainties. Provided that the sources of systematic uncertainties can be controlled up to a level of the theoretical uncertainty a higher precision in the theoretical computation may be relevant in future.

For cored profiles, the limits degrade by a factor up to 200 compared to the Einasto profile assuming core radii up to 5 kpc [335]. The right panel of Fig. 3.5 shows the impact of a cored DM distribution in the GC on the Wino dark matter model. For a 2.3 TeV DM mass, DM profiles with core radii lower than 5 kpc can be excluded. For DM mass of 9 TeV, DM profiles with core radii lower than 3 kpc can be excluded, as shown in the right panel of Fig. 3.5. At the thermal DM mass of 2.9 TeV, the forecast lower limit on the core size is approximately 2 kpc.

Given the H.E.S.S. sensitivity achieved in the Galactic Centre from H.E.S.S.-I observations, Wino dark matter could be probed with current H.E.S.S. data.

Prospects for CTA for Wino and Higgsino

Given the expected performances of the Southern site of the CTA observatory which is the best site to observe the Galactic Center region under the most favorable observation conditions, new standard astrophysical emissions may likely be detected there such as the Galactic diffuse emission measured by Fermi-LAT.

Forecast sensitivities for CTA are computed on the two prototypal dark matter candidates including the irreducible background from misidentified cosmic rays from latest Monte Carlo simulations, as well as a range of estimates for the galactic diffuse emission and Fermi bubbles at TeV energies. A 3D-template likelihood ratio test statistics technique has been developed taking into account the spatial and spectral features of expected signal and background [312].

The left panel of Fig. 3.6 shows the CTA sensitivity expressed as the 95% C.L. mean upper limits on the Wino annihilation line cross section as function of its mass for 500 h of CTA observations in the 5° of the GC. There is an improvement of roughly an order of magnitude in $\sigma v_{\rm line}$. The Wino model can be severely constrained by future CTA observations up the ten TeV masse range for cored dark matter profile as large as 5 kpc. The right panel of Fig. 3.6 shows the impact on the astrophysical background on the expected CTA sensitivity for Wino dark matter. The most impactful background component is the Fermi

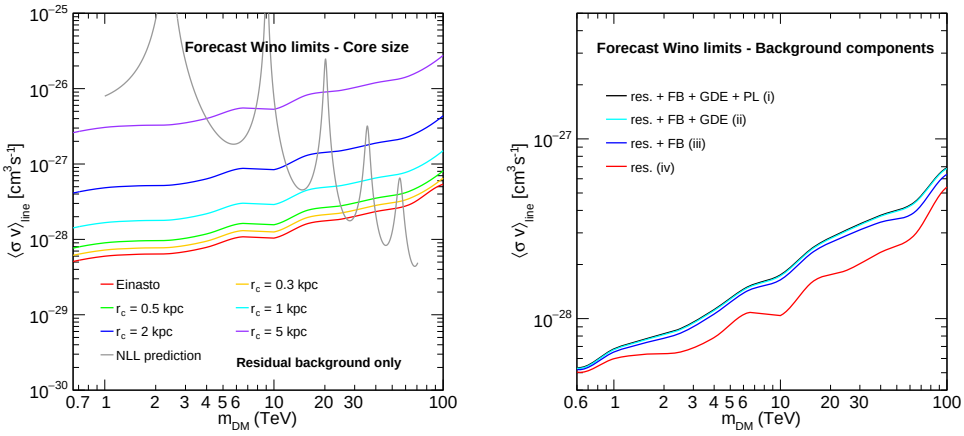

Figure 3.6: *95% C.L. mean expected upper limits on the Wino annihilation cross section as function of its mass for 500 h of CTA observations towards the GC.* ***Left panel:*** *The predicted NLL cross section is show (solid gray line) and the thermal Wino DM mass is marked (cyan solid line and bands). The only background considered here is the residual background. The full Wino spectrum is included in the expected signal. The limits are shown for the Einasto and cored DM profiles of size from 200 pc to 5 kpc.* ***Right panel:*** *Impact of the standard gamma-ray emissions that contribute to the background and the continuum and endpoint contributions to the Wino spectrum. The limits are shown for residual background only (red solid line) and with additional Fermi Bubbles emission (blue solid line), GDE gamma rays (cyan solid line) and VHE Fermi-LAT point-like (PL) sources (black solid line). Figures extracted from Ref. [312].*

Bubbles using an optimistic spectral model, while the soft model has a negligible impact on the limits. The Fermi-LAT pointlike sources have a negligible effect.

The left panel of Fig. 3.7 shows the forecast 95% C.L. upper limits on σ_v for a Higgsino candidate. The limits improve with respect to the simple line in the low masses where the continuum contribution dominates over the line feature at the end of the spectrum. The right panel of Fig. 3.7 shows the impact of a cored dark matter distribution in the Galactic Centre for core size from 200 pc to 5 kpc.

Wino dark matter can be severely constrained by future CTA observations up the ten TeV masse range for cored dark matter profile at the Galactic Centre as large as 5 kpc. Higgsino dark matter could be probed up to 10 TeV for an Einasto dark matter profile the Galactic Centre. The most impactful background is Galactic diffuse emission and the base of the Fermi Bubbles emission for the optimistic spectral model. The sensitivity can degrade up to a factor of two.

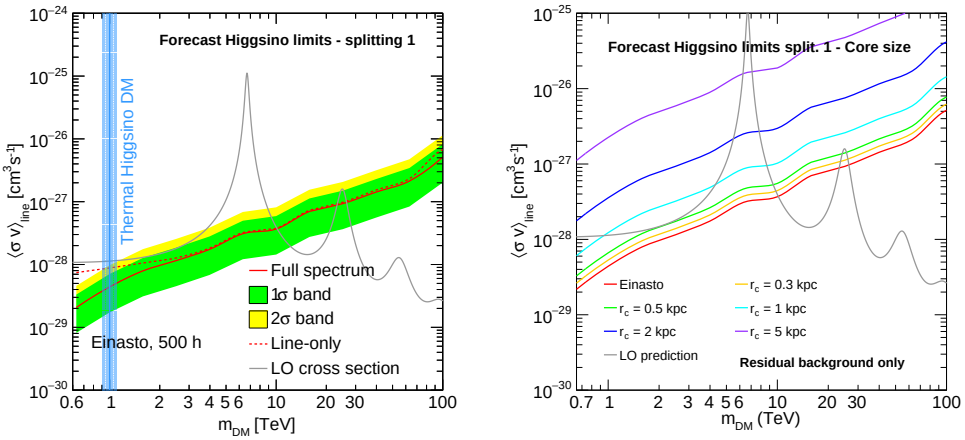

Figure 3.7: *95% C.L. mean expected upper limits on the Higgsino annihilation cross section as function of its mass for 500 h of CTA observations towards the GC.* ***Left panel:*** *The limits for an Einasto profile (red solid line) are shown together with the 1σ (green band) and 2σ (yellow band) containment bands obtained from the Asimov dataset. The theoretical tree-level cross section is overlaid in gray. The mass splitting is taken for $m_N = 200\,keV$ and $m_+ = 350\,MeV$. The thermal Higgsino dark matter mass is marked (cyan solid line and bands).* ***Right panel:*** *The limits are shown for cored DM profile of size from 200 pc to 5 kpc. Figures extracted from Ref. [312].*

H.E.S.S. constraints and CTA sensitivity in the pMSSM

Beyond the search for WIMP pure states, the H.E.S.S. limits and CTA sensitivity on the velocity-weighted annihilation cross section can be confronted to predictions in the framework of supersymmetric models. Neutralino dark matter in a phenomenological Minimal Supersymmetric Standard Model (pMSSM) can be tested using the latest constrained obtained by H.E.S.S. using observations of the Galactic centre region [300, 301]. The CTA sensitivity computed in inner 5° of the Galacitc centre is applied to a numerical scan of the pMSSM. See Ref. [337] for more details.

Figure 3.8 shows the 95% C.L. upper limits of H.E.S.S. on the annihilation cross section versus the neutralino mass. The distribution of pMSSM models including all relevant experimental constraints and theoretical developments is plotted. Assuming an Einasto DM profile at the Galactic Center, Wino dark matter is strongly constrained by present H.E.S.S. limits. The CTA sensitivity provides a significant improvement over the existing H.E.S.S. limits.

Thermally-produced Wino dark matter is strongly constrained by H.E.S.S. the

Higgsino dark matter parameter space is within the reach of CTA. For the first time Higgsino-dominated neutralino dark matter could be probed by IACTs.

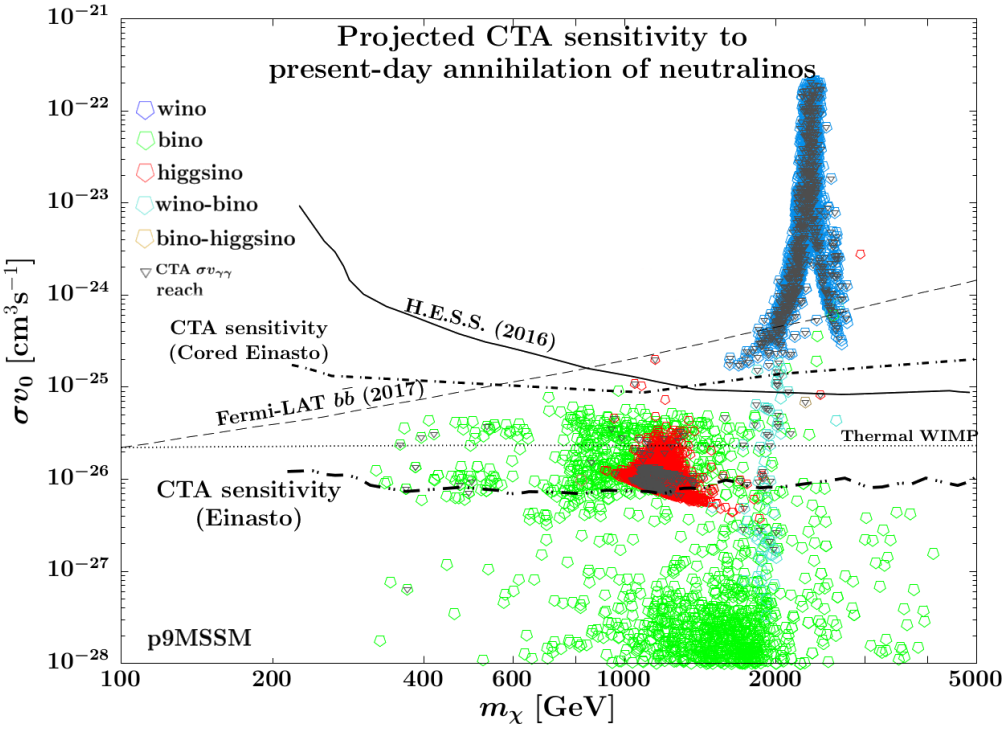

Figure 3.8: *Distribution of p9MSSM points in the plane annihilation cross section versus the lightest neutralino mass. The composition of the lightest neutralino is encoded with colors. The current upper 95% C.L. limits from H.E.S.S. applied to the p9MSSM are indicated (black solid line). The projected CTA sensitivity applied to the p9MSSM is shown as a thick (Einasto), or thin (Cored Einasto) dashed double-dotted line. All points above the line will be probed at the 95% C.L. The Fermi-LAT limits in the $b\bar{b}$ channel from dwarf spheroidal galaxy observations are shown as a dashed line. To highlight the complementarity between the continuous and monochromatic photon search, we denote the points whose $\sigma v_{\gamma\gamma}$ is within reach (assuming Einasto halo profile) by CTA by dark gray triangles. Figure extracted from Ref. [337].*

3.1.5 Discussion

Within the next few years, searches with H.E.S.S. observations are expected to explore in-depth the WIMP paradigm for TeV DM particles via the long-term Inner Galaxy Survey programme carried out since 2016.

Expected background determination through blank-field observations at high latitudes in the same observation condition as for the Galactic Center observations presently reaches a 10-to-20% uncertainties. Future directions for improving the H.E.S.S. potential will rely on the development of accurate simulations of the residual background in the Galactic Center region, with a proper description of the NSB spatial dependency which limits so far the background measurement accuracy to a few percent systematic uncertainty. If such simulations can be achieved with sufficient accuracy, H.E.S.S. observations will enable to probe dark matter for kpc-sized profiles. Regarding the configuration for the array, stereo observations are the best suited for the WIMP dark matter, the mass range up to a few hundred GeV being well probed by Fermi-LAT observations of dwarf satellites of the Milky Way.

The H.E.S.S. observations make it real to probe WIMP dark matter candidates with enhanced gamma-ray line-like feature in their annihilation spectrum, a quite generic feature for prototypal TeV WIMP. The sensitivity achieved by H.E.S.S. observations in the Galactic Centre proves to be sufficient to test thermal Wino dark matter for dark matter profiles extending up to a few kiloparsecs. The future searches using the extended capabilities of CTA with the planned survey of the inner several degrees of the Galactic Center will be decisive for Wino dark matter. While the Higgsino models could not be probed as a whole, strong constraints could be set on this dark matter model for core size up to several kpc by CTA..

In order to probe the thermal value of the annihilation cross-section over a broad range of DM masses, deep observations of the GC over several degrees in radius (at least up to 5 degrees) with CTA are required with uniform exposure and the best possible control of systematic uncertainties. A key point is the precision of the residual background determination which could limit the CTA reach. Beyond the ON-OFF method for background measurement on a run-by-run basis that proved to be successfully applied in the context of H.E.S.S. searches, data-driven Monte Carlo simulations of the expected background taking into account the instrumental and observational characteristics of each observation run are a promising avenue in order to keep the systematic uncertainties to a level that does not prevent from spoiling the projected CTA sensitivity.

Near-future analyses will make use of multi-template analyses techniques including the spectral and spatial features of all the relevant astrophysical emissions in the Galactic Center region. Such analyses will be crucial tests of WIMP dark matter provided that accurate determination of the residual background through dedicated Monte Carlo simulations implementing the most precise information on the instrumental and observational conditions of the data taking.

If these requirements are found to be successfully achieved, CTA will give crucial informations for TeV-ish WIMP dark matter in the next decade. Fur-

thermore, in the *optimistic scenario* where the LHC will discover new physics in which thermal DM candidates are present, CTA will be probably the only player that could cross-check such possible results against an astrophysical environment.

3.2 Dwarf galaxy satellites of the Milky Way

Nearby dwarf galaxies (dSph) in the Local Group are the subject of extensive observation campaigns with current IACTs. Among the dSphs observed by H.E.S.S. are the Sagitttarius dwarf galaxy [338], the Canis Major overdensity [227] and the classic dwarf galaxies Sculptor and Carina [339], and more recently Fornax and Coma Berenices [316]. Other dSphs visible in better observation conditions from the Northern hemisphere by MAGIC and/or VERITAS are Draco, Ursa Minor, Bootes 1. No significant gamma-ray signal has been detected from any of observations performed by IACTs and dark matter constraints are expressed in terms of upper limits on the velocity-weighted annihilation cross section versus the dark matter particle mass assuming plausible dark matter halo profiles.

3.2.1 The example of the classical dwarf galaxy Sculptor

Given the hundreds of member stars identified for Sculptor located at about 80 kpc from the Sun, a large variety of investigated DM halos permits to have a handle on the astrophysical uncertainties introduced by the modelling of the DM distribution. Using two RGB (Red Giant Branch) stellar populations to partially break the Jeans degeneracy in the DM halo modelling [340], the DM halo mass content of Sculptor dSph as well as its profile parameters have been estimated in Refs. [341, 342], Various dark matter halos are used to be able to estimate the knowledge of the dark matter distribution in Sculptor. In addition, two different assumptions for the stellar velocity dispersion anisotropy parameter β are explored in [342]: a radially constant velocity dispersion anisotropy, and a Osipkov-Merritt (OM) velocity dispersion anisotropy [343, 344]. The astrophysical factor is computed for eight different dark matter halos and the derived values spread over a factor 20 in magnitude, which encompasses a large class of models and give a realistic estimate of the systematic uncertainty from the halo modelling. See Ref. [339] for more details.

For a given dark matter profile of Sculptor, constraints have been derived from H.E.S.S.-I observations towards Sculptor. Figure 3.9 shows the dark matter constraints from H.E.S.S. observations towards Sculptor expressed in terms of exclusion limits at 95% C. L. on the velocity-weighted annihilation cross section. They lie at about 10^{-23} cm^{3}s^{-1} for 1 TeV dark matter masses. Unless a few

order-of-magnitude enhancement is expected on the predicted dark matter signal, current observations with hundreds of hours could not test the most natural value of $\langle\sigma v\rangle \simeq 3\times10^{-26}$ cm^{3}s^{-1}.

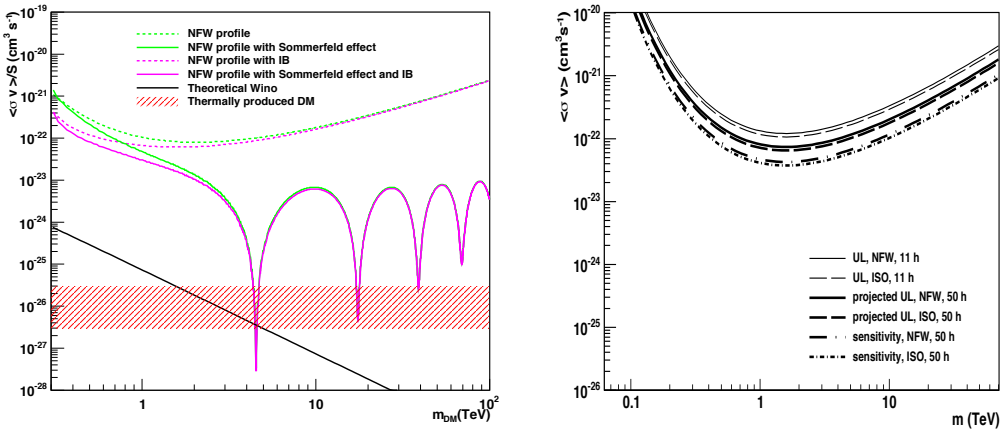

Figure 3.9: *Dark matter constraints from H.E.S.S. observations towards classical dwarf galaxies expressed in terms of 95% C.L. upper limits on $\langle\sigma v\rangle$ versus the dark matter particle mass.* ***Left panel:*** *The constraints enhanced by the Sommerfeld effect (green solid line) and the internal Bremsstrahlung (magenta dashed line) for a NFW profile of Sculptor are shown. The predicted $\langle\sigma v\rangle_0$ for a pure wino (solid black line) as well as the typical cross section for a thermally-produced DM (dashed red area) are also plotted. Figure extracted from [345].* ***Right panel:*** *95% C.L. upper limits on $\langle\sigma v\rangle$ as a function of the dark matter mass for NFW (solid line) and isothermal (ISO; dashed line) DM halo profiles, respectively. The projected upper limits are displayed for 50 hour observation time. The sensitivities at 95% CL for 50 hour are also shown for NFW (long-dashed dotted line) and ISO (dashed dotted line) dark matter halo profiles. The parametrization of the self-annihilation gamma-ray spectrum is taken from Ref. [346] for a neutralino annihilating into W and Z pairs. Figures extracted from Ref. [347].*

Additional effects may substantially increase the expected dark matter signal as discussed in Sec. 2.1.3. The Sommerfeld effect is particularly relevant in objects like dwarf galaxies since it is most efficient in the coldest structures. Assuming that the DM mean velocity inside the halo is the same as for the stars[1], the relative velocity between the DM particles can be as low as 10^{-5}c. An example

[1]This assumption is plausible due to the large relaxation time scales of galaxy clusters, galaxies and dwarf galaxies. The relaxation time being sufficiently long, the velocity dispersion of the tracers was not significantly perturbed by other objects in the system. The velocity dispersion is then still very close to the initial value, which can be assumed to be the same for DM and other gravitational bound objects.

of the Sommerfeld effect is shown in the right panel of Fig. 3.9 assuming the dark matter particle is a wino that purely annihilates in W^+W^- pairs through the Z gauge boson. A series of resonances allow the exclusion for specific dark matter masses at the level of $\langle\sigma v\rangle\sim 10^{-26}$ cm^{3}s^{-11}. Outside the resonances, the constraints are improved by a factor of about 10 in the TeV mass range. The electromagnetic radiative correction to the main annihilation channels into charged particles can give a moderate enhancement to the expected dark matter signal due to internal Bremsstrahlung. This contribution to the annihilation spectrum can be appreciated on the exclusion limits presented in the right panel of Fig. 3.9. These corrections manifest as a bump-like feature close to the dark matter mass and thus contribute much more close to the energy threshold. As the dark matter mass increases, it becomes dominated by the contribution of the gamma-ray continuum.

3.2.2 The tidally-disrupted dwarf galaxy Sagittarius

Since the expected dark matter flux is inversely proportional to the square of distance, one would expect the best dwarf spheroidal galaxies targeted for observations to be the nearest one. However, such dwarf galaxies are also the closest to the Galactic Center and may experience strong tidal effects from the Milky Way.

The Sagittarius dSph is the only satellite galaxy in the MW that shows clear evidence of ongoing tidal mass stripping [348] in the form of an associated tidal stream [349, 350, 351, 352, 353, 354, 355]. The core of Sagittarius dSph is located at l = 5.6° and b = -14° in Galactic coordinates at a distance of about 24 kpc from the Sun. Sagittarius has made at least ten Milky Way crossings and should thus contain a substantial amount of DM to avoid having been entirely disrupted. Velocity dispersion measurements on M giant stars with 2MASS yields a light to mass ratio of about 25 [356]. The Sgr dSph core is positioned behind the bulge of Milky Way but outside the Galactic plane, thus reduced foreground gamma-ray contaminations are expected.

The observations of Sagittarius started in 2006 and the first constraints have been published in Ref. [338] with the mass model available at that time. Since then, it has been shown that one could take advantage of this effect to trace back the evolution history of the object [357]. During the orbital motion of a dwarf galaxy, multiple crossings of the dwarf galaxy through the galactic disc of the Milky Way give rise to the formation of tidal streams, a careful study of which make possible to infer the gravitational potential of the dwarf galaxy and thus

[1]Note here that the Sommerfeld effect is taken into account in the limit and not in the predicted cross section.

the DM halo potential. Furthermore, measurements of stars within Sgr dSph and the luminosity of its core and surrounding debris, allows the estimate of the DM content prior to tidal disruption [358].

The proximity of the Sgr dSph to the Milky Way together with the fact that this galaxy is shedding stars to tides complicates its dynamical modelling: *(i)* the distribution of dark matter and stars has been clearly altered from its original configuration by tidal mass stripping. Given that the actual amount of stars and dark matter in the tidal tails is unknown [358], the original mass, luminosity and size of the Sgr dSph remain fairly uncertain quantities; *(ii)* the assumption of dynamical equilibrium may not be adequate, specially in the outskirts of the galaxy where the population of unbound stars may dominate in number over that of bound members [359]. One can assume that the external tidal field does not influence the kinematics of stars that locate the central region of the dSph, and ignoring the effects of tidal stripping on the outer ($r \gg r_s$) dark matter halo profile, one can use the Jeans equations to search the DM halo parameters that best fit the stellar central velocity dispersion for a given King core radius of this object. The King-NFW degeneracy gives rise to a family of NFW halo models which can reproduce the stellar dynamics [360]. One way to break this degeneracy is using the relationship between the virial mass and concentration found in cosmological N-body simulations [361]. Using this procedure on the SDSS survey data provides a value of $r_s = 1.3$ kpc. Considering the scatter on the relationship between virial mass and concentration, the 2σ error on r_s is found to be $\sim$0.2 kpc. This correspond to the family of models with ρ_s spanning from 7.5×10^{-3} to 1.3×10^{-2} $\mathrm{M_\odot pc^{-3}}$. An independent analysis in Ref. [362] provides similar values for these parameters. In the latter case the astrophysical factors are found to be of a few higher than the ones used here.

However, numerical N-body models that aim to describe the observed structural and kinematical distributions of stars in the tidal tails as well as the remnant core provide a more consistent approach to the dynamical analysis of the Sgr dSph. Yet, most of the existing N-body models of this galaxy assume for simplicity that dark matter and stars share the same spatial distribution (the so-called ″mass-follows-light models′″), an assumption that is not supported by detailed kinematic data of dwarf spheroidal galaxies (e.g. Ref. [236]). An exception to date corresponds to recent N-body models constructed in Ref. [363], who explore the possibility that the Sgr dSph may have originally been a rotating galaxy. In these models the galaxy is composed of an exponential stellar disk embedded in an extended DM halo. The DM density profile is parameterized as a cored isothermal profile. The DM halo mass can be estimated using the initial luminosity and a given mass-to-light ratio. Using the results from Ref. [358] the initial luminosity is estimated to be $\sim 10^8\,\mathrm{L_\odot}$. Assuming a mass-to-light ratio of 25 [364], the DM halo mass is found to be $m_\mathrm{h} = 2.4 \times 10^9\,\mathrm{M_\odot}$. To account for the

initial tidal disruption of the Sgr dSph halo by the Milky Way, a truncation of the halo profile is imposed at $r_{\rm cut} = 12\, r_{\rm c}$. The evolution of Sgr in the Milky Way potential is obtained via a N-body model of Sgr dSph [365]. The evolution code allows to recover the actual DM profile by using the constraint of the observed stellar distribution. More details on the modelisation and halo parameters can be found in Ref. [347].

The right panel of Fig. 3.9 shows the upper limits of H.E.S.S. on $\langle \sigma v \rangle$as a function of the DM mass. Using the H.E.S.S. upper limits published in Ref. [338], the new upper limits are calculated for the above-mentioned NFW and ISO DM halo profiles. They reach about 10^{-23} cm^{3}s^{-1} for a DM mass of 1 TV. The projected upper limits and the sensitivity for 50 h of observation time are also shown.

Standard astrophysical gamma-ray background in Sagittarius dSph ?

dSph galaxies are commonly believed to contain very little background emission from conventional astrophysical sources at VHE energies. This assumption is based on their low gas content and stellar formation rate. However, some gamma-ray emitting sources may still exist within them: in particular from pulsars, and black hole accretion and/or jet emission processes. The Sagittarius and Carina dwarf galaxies both host globular clusters, the globular cluster M54 is located at the center of Sgr dSph, and globular clusters are known to host millisecond pulsars (MSPs). The collective emission of high energy gamma-rays by MSPs in globular clusters has been detected by Fermi-LAT [366], and emission in the VHE energy range has been predicted by several models for these objects. So far only a VHE gamma-ray emission has been detected towards Terzan 5. In addition, it has been suggested [200, 201] that globular clusters may host black holes with masses of around 10^2 to 10^4 M$_\odot$ called intermediate-mass black holes (IMBHs). Indeed, Sgr dSph may also harhor a 10^4 M$_\odot$ IMBH [367]. Their claim is based on the study of the density profile around the central point and the observed rise in the velocity dispersion of stars.

Although the millisecond pulsars of M54 could not give a VHE signal in H.E.S.S. for reasonable observation time, it may be the case in CTA with observation times of typically 200 hours. For a cosmological thermally produced DM particle and without any boost factor, the corresponding signal would have a significance of 0.1σ, after 200 hours of observation. The collective MSP signal would be a few orders of magnitude stronger than the DM annihilation signal. The emission of a putative IMBH at the centre of Sgr dSph is dominated by *pp* interactions and the flux is expected to be in the 10^{-18} - 10^{-17} erg cm^{-2}s^{-1} for reasonable parameters, too faint to be detected by CTA. For the computation of the expected conventional fluxes and more extended discussion, see Ref. [347].

More details can be found in Ref. [310]

The dark matter limits obtained by H.E.S.S. have been the first towards a dSph with a third-generation IACT. While Sagittarius dSph is quite massive and nearby, tidal stripping effects from the Milky Way make the determination of its present dark matter distribution very complex.

3.2.3 Ultra-faint dwarf galaxies detected by DES

Nearby ultra-faint dSphs are obvious targets for DM searches by current IACTs. While the systematic uncertainties on the expected DM signal from the modeling of the DM halo may dominate the statistical uncertainty related to the limited number of stellar tracers, they have estimated J-factors which are larger than the J-factors of the best classical dwarfs.

Until recently, the observation by H.E.S.S. towards ultra-faint dSphs observable was limited to Coma Berenices. Coma Berenices dSph was recently discovered in the Sloan Digital Sky Survey [368] and is located at a distance of about 44 kpc. It is one of the smallest and faintest satellites of the MW at that time and differs from the average characteristics of other dSphs in the plane of absolute magnitude vs. half-light radius [368]. However, further spectroscopic surveys reveal kinematics and metallicities expected for dSphs. Coma Berenices is claimed to be amongst the most DM dominated dSphs [369]. It is fairly regular in shape and does not show significant signs of tidal debris according to a recent photometric survey [370]. Due to its location in the sky, Coma Berenices can only be observed under high zenith angles, above $\sim$50°, which implies an energy threshold of $\sim$700 GeV) compared to $\sim$200 GeV for 20° observations. No significant VHE emission was detected. Assuming a DM matter distribution as modeled in Ref. [254] and no systematic uncertainties in the astrophysical J-factor, the constraints lie at $\langle\sigma v\rangle \simeq 10^{-22}\,\mathrm{cm^3 s^{-1}}$ for a 5 TeV mass DM [316].

New dSph are being discovered such as those by the Dark Energy Survey. Among them is the newcomer Reticulum II (DES J0335.6-5403). Indeed, given its proximity ($\simeq$ 32 kpc) and possibly high DM content, several studies [258, 371] show that it could be one of the best dSph targets for observing DM annihilation signals. Furthermore, the debate on a possible detection with Fermi of high energy γ-ray emission in the direction of this object [372, 373] (but see [371]) makes it of further interest. This larger sample of Milky Way dSph galaxies and the prospects for the detection of new ones with surveys like PanSTARRS [374, 375], Dark Energy Survey (DES) [376, 377] and Large Synoptic Survey Telescope (LSST) [378, 379, 243], are generating excitement and activity in the field.

The new Milky way satellites discovered by DES are consistent with being dSphs while a fraction of them is referred as to dSph candidates in absence of confirmation from spectroscopic measurements. They represent new promising

targets for gamma-ray searches of DM annihilation signals that can be observed with H.E.S.S.under favorable conditions. From 2017, observation campaigns have been carried out carried out by H.E.S.S. on selected DES satellites to search for DM annihilations. The selected systems are Reticulum II, Tucana II and Tucana III, Tucana IV and Grus II. While Reticulum II and Tucana II are confirmed dwarf galaxies through spectroscopic measurements, Tucana III, Tucana IV and Grus II are classified as candidate dwarf galaxies. The determination of the DM density distribution in these dSphs is subject to uncertainties that affect the J-factor estimates. Due to the small sample of stellar tracers in dSph, the statistical uncertainty on the J-factor is higher for ultra-faint candidates than for classical ones such as Sculptor or Draco dSphs.

The H.E.S.S. observations were carried out with the full five-telescope array towards Ret. II, Tuc II, Tuc. III in 2017 and 2018 and Grus II in 2018. No significant signal has been detected towards any of the objects. A 2 dimensional (2D)-binned Poisson maximum likelihood analysis is used to derive upper limits on the $\langle\sigma\rangle$ as a function of the dark matter mass. Fig. 3.10 shows the 95% C.L. observed upper limits together with the expectations towards the individual objects and combined limits using observations towards all objects. In the $\gamma\gamma$ channels, the limits reach $\sim 2 \times 10^{-26}$ cm^{3}s^{-1} around for a dark matter of 500 GeV. Further details can be found in Ref. [312] and the forthcoming paper.

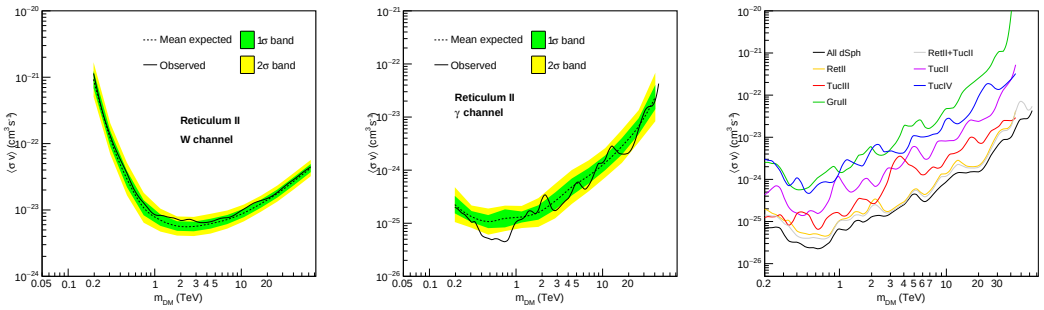

Figure 3.10: *95% C.L. upper limits on the annihilation cross section for Reticulum II in the W^+W^- (left panel) and $\gamma\gamma$ (middle panel) annihilation channels without the statistical uncertainty on the J factor. Observed limits (solid lines) together with mean expected (dotted lines) with 1σ (green area) and 2σ (yellow area) containment bands are shown. The combination of the limits is shown on the right panel. Figures extracted from Ref. [312].*

These limits are the first obtained so far with IACT observations. They are the most constraining in the TeV dark matter range.

Dedicated high-accuracy spectroscopic measurements of the stellar members

will decisively help to better determine the J-factors in the DES dSph satellites. Further work is also needed to carefully bracket the systematic uncertainties arising from the method used to model the DM halo of ultra faint dSphs and satisfactorily plan upcoming searches with current IACTs and propose a defendable selection for future observations with CTA.

3.2.4 Prospects with CTA

The Fermi satellite [380] and the IACTs have carried out various observational campaigns towards nearby dSphs, and no significant γ-ray emission has been detected so far.[1] At low energies ($E \lesssim 300$ GeV), the recent bounds on the annihilation cross section, coming from a 6-year FERMI data analysis of 15 dSphs, rule out the thermal freeze out value up to DM masses of roughly 100 GeV [317]. At higher masses, the constraints imposed by H.E.S.S. [227, 338, 339, 316], MAGIC [381, 382, 315], and VERITAS [383, 384], complement the bounds of Fermi-LAT for heavy DM candidates. In particular, the latest constraints from H.E.S.S. [316], coming from the observation of a subset of 4 dSphs, plus the Sgr dwarf, rule out a DM annihilation cross section of the order of $10^{-23}\,\mathrm{cm}^3\,\mathrm{s}^{-1}$, in the DM mass window of $1 \to 20$ TeV.

CTA will bring up to a factor of ten improvement in terms of flux sensitivity compared to currently operating IACTs [385], with a factor two to three in angular and energy resolutions. This will be fundamental for two main reasons: *i*) for well-motivated multi-TeV WIMP DM candidates (e.g. Wino and Higgsino DM, Minimal DM 5-plet), the annihilation cross sections into SM particles could receive a significant boost at low velocity (e.g. in dSphs $v \sim 10$ km/s) due to Sommerfeld corrections by orders of magnitudes [329, 386, 86, 387]. Therefore, a gain in sensitivity with respect to currently operating IACTs, can be sufficient to probe almost the entire parameter space of many well motivated WIMP models at the TeV-scale. *ii*) Given the angular resolution of CTA, dSph galaxies will be no longer point-like objects. This is important because one can then implement a spatial analysis of the likelihood, which will improve the CTA sensitivity.

A few years ago, the prospective studies started and first computation of the CTA sensitivity towards the most promising classical and ultra-faint dSphs have been published in 2013 [388]. More recently, as shown in Ref. [311], dSph galaxies are extended objects for CTA: in particular, the dSph galaxies with flat J-factor profiles (e.g. Draco, Ursa Major II) are more extended objects in gamma-rays than dSphs with steep profiles (e.g. Ursa Minor and Coma Berenices). Sensitivity

[1] A $3.2\,\sigma$ detection of a γ-ray excess at energies between 2 to 5 GeV has been reported from an analysis of pass 7 data from FERMI [372, 373], but the significance of this detection is only $1.65\,\sigma$ significant with the pass 8 data [371].

prospects have been carried out. Details on the analysis methodology can be found in Ref. [311].

Fig. 3.11 shows the sensitivity for 500 h of observation in different annihilation channels for two classical and two ultra-faint dSph galaxies. For all dSphs, the strongest sensitivity is obtained for the DM DM $\to \tau^+\tau^-$ primary annihilation mode (blue lines) for $m_{\rm DM} \simeq 300$ GeV. In particular, for the best classical dSph, Ursa Minor (left panel), the CTA sensitivity reaches $\langle\sigma v\rangle \simeq 1 \times 10^{-24}$ cm^{3}s^{-1}. In

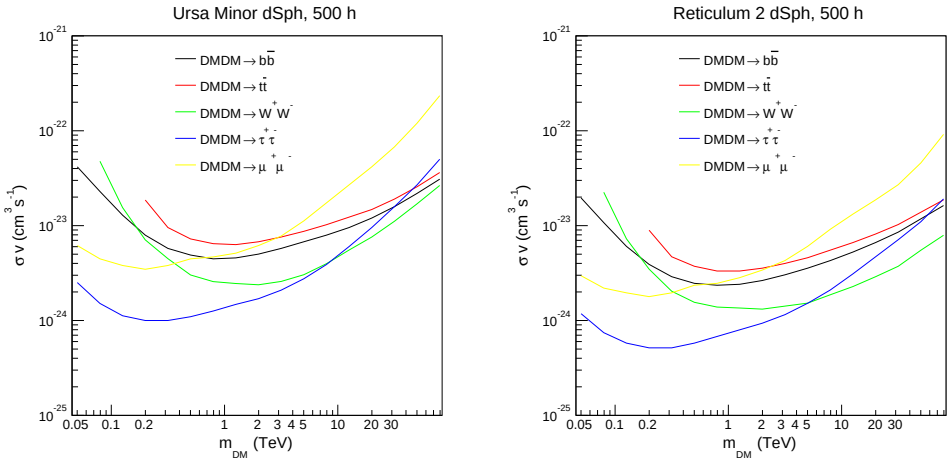

Figure 3.11: *CTA sensitivity to DM annihilation towards the classical dSphs Draco (upper left panel) and Ursa Minor (upper right panel), and the ultra-faint dSPgs Reticulum II and Several primary channels are considered: DM DM $\to b\bar{b}$ (black lines), $t\bar{t}$ (red lines), W^+W^- (green lines), $\mu^+\mu^-$ (yellow lines), and $\tau^+\tau^-$ (blue lines), and an observation time of 500 h. The bounds are obtained by implementing a 2D statistical approach based on a likelihood ratio test statistic [113]. Figure extracted from Ref. [309].*

the right panel the sensitivity towards the very promising newcomer Reticulum II is shown. The bounds are quite strong reaching $\langle\sigma v\rangle \simeq 5.1 \times 10^{-25}$ cm^{3}s^{-1} for Reticulum II. For the DM DM $\to \mu^+\mu^-$ channel (yellow lines), the CTA sensitivity is weaker and the best limit is obtained by looking at Reticulum II ($\langle\sigma v\rangle \simeq 1.8 \times 10^{-24}$ cm^{3}s^{-1} for $m_{\rm DM} \simeq 200$ GeV).

Todate, the best dSphs for studying VHE γ-rays from DM annihilations are Ursa Minor (best "classical" dSph), Ursa Major II, and the newcomer Reticulum II (best "ultra-faint" ones). For all dSphs, the strongest sensitivity is achieved for the DM DM $\to \tau^+\tau^-$ primary annihilation mode at $m_{\rm DM} \simeq 300$ GeV. In particular, with 500 h of observation towards Reticulum II, one can probe annihilation cross section larger than 5×10^{-25} cm^{3}s^{-1}. For the hadronic channels and the DM DM $\to W^+W^-$ mode, the best sensitivity is again achieved towards Reticulum II at $m_{\rm DM} \simeq 1$ TeV. More specifically, the best sensitivity is obtained

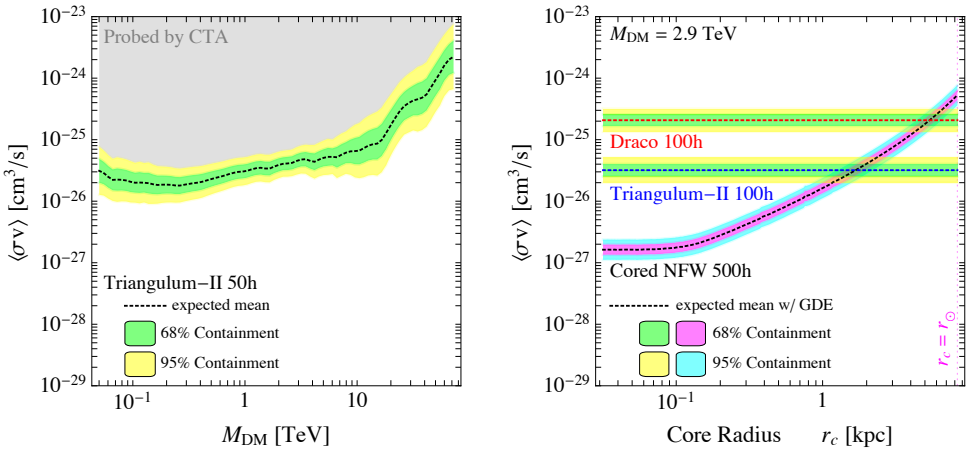

Figure 3.12: *CTA sensitivity to DM line signals towards the classical dSph Draco and the ultra-faint one Triangulum II and comparison with Galactic Center sensitivity.* ***Left panel:*** *CTA sensitivity to monochromatic photons from the GC (100 hours of observation), Triangulum-II (50 hours) and Draco (50 hours), as a function of the core radius of the NFW DM profile of the Milky Way, up to the Sun position, for a DM mass of 2.9 TeV (Wino thermal mass).* ***Right panel:*** *CTA sensitivity to monochromatic gamma rays from the GC (100 hours of observation), Triangulum-II (50 hours) and Draco (50 hours), as a function of the core radius of the NFW DM profile of the Milky Way, up to the Sun position for a DM mass of 2.9 TeV. Figures extracted from Ref. [272].*

for the DM DM $\rightarrow W^+W^-$ primary mode ($\langle\sigma v\rangle \simeq 1.3 \times 10^{-24}$ cm^{3}s^{-1} in the multi-TeV mass range). This is very interesting, because well-motivated heavy DM candidates with electroweak interactions possess annihilation cross sections towards dSph galaxies of the same order of magnitude, thanks to the non-perturbative Sommerfeld effect that can significantly boost the DM annihilations into all electroweak bosons (W^+W^-, ZZ, $Z\gamma$ and $\gamma\gamma$). The left panel of Fig. 3.12 shows the CTA sensitivity in the $\gamma\gamma$ annihilation channels for Triangulum II[1]. The right panel of Fig. 3.12 shows a comparison of the CTA sensitivity for Thermal Wino dark matter between Triangulum II and the Galactic Centre as a function of the core radius of the DM distribution in the Galactic Centre. Using th most recent determination of the J-factor of Triangulum II, searches towards dSph are competive with the Galactic Centre one for several kpc core sizes.

For the upcoming searches with CTA it would be of primary interest to perform: i) a real assessment of the systematic uncertainties in the determination of

[1]Note however that recent estimate of the J-factor of Trinagulum II makes the senstitivity deteriorated by a factor of about 10.

the J-factor towards our best dSphs, because in this way one can control with an unprecedented level of accuracy the normalization of the DM signal; ii) gamma-ray line searches in the DM spectra at VHE (above few TeV) towards the best dSphs by either the currently operating IACTs or by the forthcoming CTA.

3.3 Dark matter substructures in the Galactic halo

Observations with IACTs can be efficiently used for non-targeted searches. Space-based instruments such as the Fermi satellite can much more easily perform blind searches for DM subhaloes with a regular scanning of the entire sky thanks to their large field of view. Some prospect regarding searches with Fermi can be found in Refs. [389, 390, 391] and analyses based on actual data were released in Refs. [392, 393, 394].

The wide-field survey with H.E.S.S. has been conducted with the data of the Galactic plane survey. They have been used to perform for the first time a blind search for DM substructures with a wide-field survey with IACTs in Ref. [395]. Two substructure scenarios have been considered here: DM spikes around intermediate mass black holes [217] and more conventional CDM subhalos obtained by the cosmological N-body simulation Via Lactea II [20]. Note that the former substructure scenario is rather optimistic since the abundance and the properties of intermediate-mass black holes and of the DM spikes around them remain poorly constrained. The latter scenario may be considered more conventional as substructures in the form of subhalos in the Galactic halo are a generic prediction of cosmological N-body simulations that seek to explain galaxy structure formation.

3.3.1 Wide-field searches with H.E.S.S.

Data collected during the Galactic plane survey with the four telescope H.E.S.S. array have been used to compute wide-field sensitivity map. Conventional astrophysical models of TeV emission are available for these sources and the search is focused on regions where no standard astrophysical emitters have been detected by H.E.S.S. The position of the DM subhalos is not known and the background measurement cannot rely on standard background technique. The background is estimated using the template model method as explained in Ref. [395]. This allows to estimate the background level at each sky position. For the method defined to perform flux sensitivity map computation, see Ref. [395]. The top panel of Fig. 3.13 shows an example of the observed sensitivity map in the Galactic plane with 2004-2007 dataset from Galactic longitudes $l = -30^\circ$ to

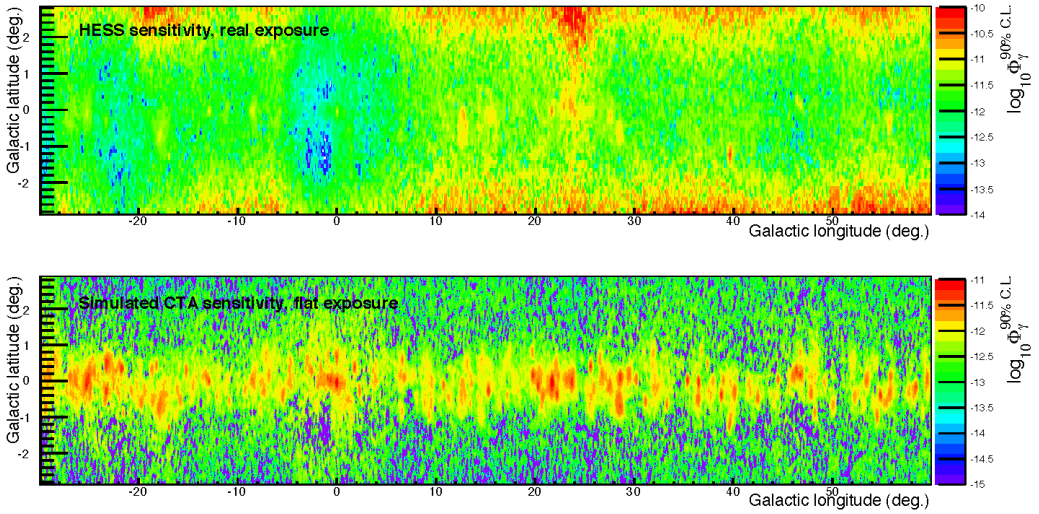

Figure 3.13: ***Top panel:*** *H.E.S.S. sensitivity map in Galactic coordinates, i.e. 90% C.L. limit on the integrated gamma-ray flux above 100 GeV, for dark matter annihilation assuming a dark matter particle of mass m_χ = 500 GeV and annihilation into the $b\bar{b}$ channel. The flux sensitivity is correlated to the exposure and acceptance maps. In the Galactic latitude band between -2° and 2°, the gamma-ray flux sensitivity reaches $10^{-12} cm^{-2} s^{-1}$.* ***Bottom panel:*** *A simulated flux sensitivity map for a CTA-like array is obtained for a flat exposure of 10 h.*

$l = +60°$ and Galactic latitudes $b = -3°$ to $b = +3°$, for a dark matter particle of 500 GeV mass annihilating into the $b\bar{b}$ channel. The H.E.S.S. sensitivity depends strongly on the exposure time and acceptance maps which are related to the choice of the pointing positions in the Galactic Plane survey. The flux sensitivity varies along the latitude and longitude due to inhomogeneous coverage of the Galactic plane. By construction, the sensitivity map depends on the dark matter annihilation spectrum. However, the spectrum is balanced by the effective area which mainly drives the result of the computation of the integrated flux. The particle mass does not to bring about strong variations in the map as long as the mass is larger than the effective energy threshold of ∼100 GeV. In the band between $-2°$ and $2°$ in Galactic latitude, a DM annihilation flux sensitivity at the level of 10^{-12} cm^{-2}s^{-1} is achieved. Deeper observations of the GC and at Galactic longitude of $\sim -20°$ allow the flux sensitivity of $\sim 5 \times 10^{-13}$ cm^{-2}s^{-1} for a 500 GeV DM particle annihilating in the $b\bar{b}$ channel.

This flux upper limit map has been the first computed with H.E.S.S. data in a few hundred degree squared field of view.

3.3.2 Intermediate mass black holes

In order to study the consequences of a wandering population of Galactic IMBHs for indirect dark matter searches H.E.S.S. data have been confronted to predicted signals from mock IMBH catalogs of Ref. [217]. Stochastic realizations of Milky Way-like halos at $z = 0$ are obtained by populating halos with black holes at high redshift following the prescriptions of scenarios A and B and evolving them forward to determine the properties of satellite black holes now. See Sec. 2.3.3 for assumptions about the IMBH initial mass function and halo profile. The analysis has been based on a statistically large sample of black hole population in Milky Way-like halos of this Milky Way mass.

The right panel of Fig. 3.14 shows the exclusion limit at the 90% C.L. on σv as a function of the neutralino mass $m_{\rm DM}$. The neutralino is assumed to annihilate into $b\bar{b}$ and $\tau^+\tau^-$ with 100% BR, respectively. For neutralino masses in the TeV energy range, the limits for the mini-spike scenario B on σv are at the level of 10^{-28} cm^{-3}s^{-1} for the $b\bar{b}$ channel.

For the first time, a subhalo clumpiness scenario has been tested in a large field of view with an IACT and first experimental constraints with an IACT array on a dark matter mini-spike scenario from Ref. [217] has been derived. For further results and extended discussion, see Ref. [395].

3.3.3 Dark matter subhalos of the Milky Way

Using flux sensitivity maps, one can compute, for a fixed set of particle physics parameters, the probability for a subhalo to lie in the survey region with a flux larger than the H.E.S.S. sensitivity at its position in the sky. About 168±44, out of the $\sim 10^4$ resolved subhaloes contained in the Milky Way lie in the the Galactic survey field of view shown in Fig. 3.13. In order to compute a 90% C.L. limit on $\langle \sigma v \rangle$, the mass of the DM is kept fixed and the value of the cross section for which 2.3 subhaloes are visible on average in the sensitivity map accordingly computed for the given mass and annihilation spectrum, is searched.

The right panel of Fig. 3.14 shows the 90% C.L. exclusion limit on $\langle \sigma v \rangle$as a function of the DM particle mass considering $b\bar{b}$ and $\tau^+\tau^-$ annihilation spectra with 100% branching ratio, respectively. The limits on the annihilation cross section reach a few 10^{-24} cm^{3}s^{-1} at 1 TeV for the $\tau^+\tau^-$ spectrum. The dashed region corresponds to cosmologically relevant values for the annihilation cross section. The obtained constraints are 2 orders of magnitude above this region.

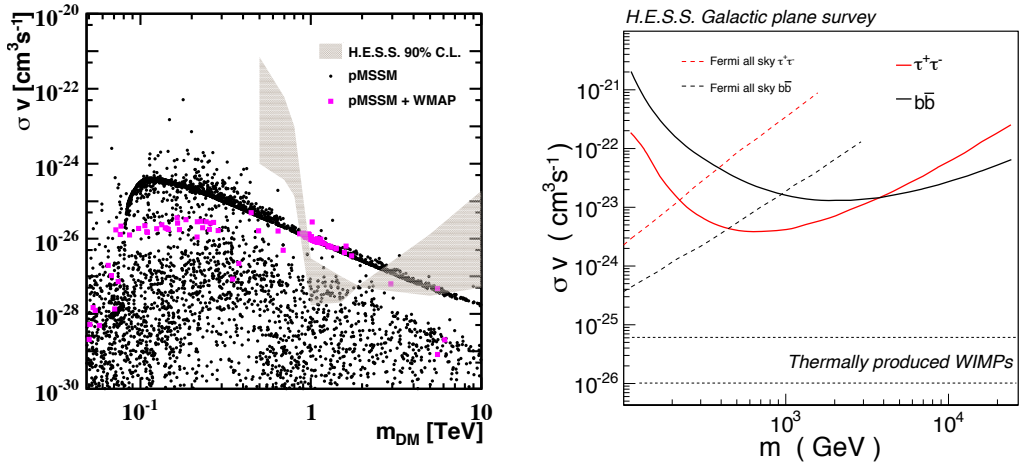

Figure 3.14: ***Left panel:*** *Constraints on the IMBH gamma-ray production scenario B for different neutralino parameters, shown as 90% C. L. upper limits on the annihilation cross section σv as a function of the mass of the dark matter particle $m_{\rm DM}$ form the H.E.S.S. Galactic plane survey. The dark matter particle is assumed to be a neutralino annihilating into $b\bar{b}$ or $\tau^+\tau^-$ pairs. SUSY models from the pMSSM models (black points) are plotted together with those satisfying the WMAP constraints on the dark matter particle relic density (magenta points). Figure extracted from Ref.[395].* ***Right panel:*** *H.E.S.S. constraints from DM subhaloes provided by the Via Lactea-II simulation expressed as 90% C. L. upper limit on σv versus the DM particle mass m. The DM particle is assumed to annihilate into purely $b\bar{b}$ and $\tau^+\tau^-$ pairs, respectively. The region of natural values of the velocity-weighted annihilation cross section of thermally produced WIMPs is also plotted (dashed regions). Figure extracted from Ref. [396].*

Prospects for CTA and discussion

Larger scans of the sky will likely be carried by CTA. In particular, a more extended survey of the order of a quarter-sky size is foreseen [309]. Here, the CTA sensitivity to DM annihilations is computed in the context of such an ambitious program. A large survey increases the probability to find bright subhalos in the field of view, which thus translates into better constraints. For a H.E.S.S.-like Galactic plane survey, an exposure of 10 h in each pixel corresponds to a total observation time for building up the survey of ∼400 h. Assuming a supernovae remnant source model for the gamma-ray emission and a radial source distribution, the distance and the gamma-ray flux are calculated. The Galactic plane is then randomly populated according to the spatial distribution of sources observed by the H.E.S.S. Galactic Plane survey. So the gamma-ray flux source distribution measured by H.E.S.S. is extrapolated to CTA performance. This

extrapolation results in the prediction for the discovery of a few hundreds of new sources in the Galactic survey field of view. The presence of these new sources deteriorates the DM flux sensitivity accordingly. For further details on the procedure see Ref. [397]. The bottom panel of Fig. 3.13 shows an example of a CTA survey of the Galactic plane. A flat exposure of 10 hours in each position of the map is assumed. This value allows us to match the total amount of time for the CTA survey to the 400 hours which were needed by H.E.S.S. to survey this region of the sky. The flux sensitivity for CTA ranges from 10^{-12} cm^{2}s^{-1} in the region where the new sources are present to a few 10^{-13} cm^{2}s^{-1} on average at higher latitudes. The left panel of Fig. 3.15 shows that the exclusion limits are improved by a factor of 10 than those obtained with H.E.S.S. In the cases of the $b\bar{b}$ and $\tau^+\tau^-$ reaching $\langle\sigma v\rangle$ values of a few cm^{2}s^{-1}. In addition, the flux sensitivity along the Galactic plane will be limited by the population of newly detected sources at a flux level of 10^{-12} cm^{2}s^{-1}.

In addition to the numerous sources that will be detected by CTA, the Galactic plane might also not be the best place to look for subhalos since they could have been tidally affected by the disk. On the other hand, the VL-II subhalo distribution is peaked towards the center of the Milky Way. For this study, a quarter-of-the-sky survey region is chosen to be from -90° to +90° in Galactic longitude and from -45° to +45° in Galactic latitude, excluding the Galactic plane between ±1.5°. Inside this region, the distribution of the number of subhaloes from the simulation has an average value of 3907, and a rms of 324. The fact that this extended survey leads to better constraints is illustrated in Fig. 3.15. The sensitivity is assumed to be constant on the entire field of view. Its value is calculated from the previous CTA sensitivity map averaged for Galactic latitudes above 1.5° and corrected for a shorter exposure. A 5 h exposure time in each pixel leads to a flux sensitivity of the order of 5×10^{-13}cm^{2}s^{-1} for a WIMP mass of 500 GeV. The right panel of Fig. 3.15 shows the 90% C.L. exclusion limit on $\langle\sigma v\rangle$ as a function of the DM particle mass for a quarter-of-the-sky survey. Annihilation cross sections of a few $10-26$ cm^{3}s^{-1} are reached in the 200 GeV - 3 TeV mass range in the case of annihilation into $\tau^+\tau^-$ channels.

The two IMBH scenarii presented in Sec. 2.3.3 are nowadays strongly constrained by gamma-ray measurements such as EGRET [228], and *a fortiori* Fermi-LAT, and H.E.S.S. measurements. While it has been recognized that EGRET should have seen IMBHs, the absence of detection was not taken into account in the prediction [217]. All available measurements in gamma-rays, neutrinos, electrons and positions will definitely help in constraining IMBH formation scenarii to make realistic prediction for indirect detection.

The spatial distribution of dark matter clumps is biased away from the smooth central dark matter distribution of the host halo, i.e., the majority of clumps

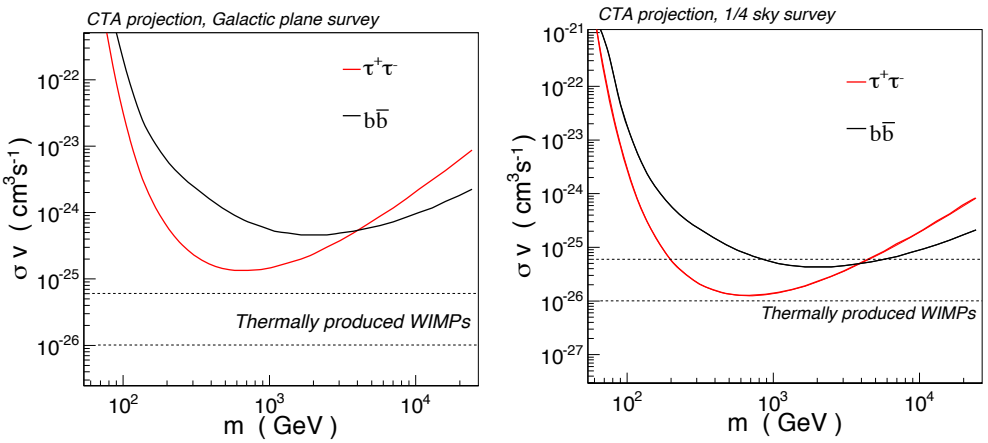

Figure 3.15: *CTA sensitivity in a wide-field-of-view surveys in term of 90% C. L. sensitivity curves on σv versus the DM particle mass m. The limit is calculated from the DM subhalo distribution provided by the Via Lactea II simulation for a CTA Galactic plane survey (left panel) and a quarter-of-the-sky survey (right panel), respectively. The DM particle is assumed to annihilate into pure $b\bar{b}$ and $\tau^+\tau^-$ pairs respectively. The region of natural σv values for thermally produced WIMPs is also plotted.*

populate outer halo regions ($r > 100$ kpc). Lacking identification in optical surveys, a quarter-of-the-sky survey in VHE gamma rays is a prime channel for detecting dark clumps. They would show the unique spectral gamma-ray signature of dark matter annihilation or decay.

Near-future experiments will be able to probe the subhalo population above 10^5 $M_\odot$ using gravitational milli-lensing of background objects [398], while the statistical properties of lighter clumps (down to Solar mass scale) in the Solar neighborhood could be measured from gravitational nano-lensing [399, 400]. Additional statistical techniques to estimate the presence and properties of moving sources contributing to a diffuse background emission are being investigated as well as shown in Ref. [401]. Dark clumps orbiting in the solar vicinity also affect the kinematics of stellar streams. A peculiar distribution of gaps would be imposed on local stellar streams by impacting clumps of all mass scales. First studies of local streams have already hinted at clump impacts [402], while further studies are ongoing or proposed [403, 404, 405, 406, 407].

3.4 Galactic globular clusters

Several Galactic Globular Clusters (GCs) have been observed with ground-based Cherenkov telescopes and upper limits on γ-ray emission from standard astrophysical processes have been reported on Omega Centauri, 47 Tucanæ, M 13, M 15 and M 5 [408, 409, 410]. The only tentative detection at VHE is towards Terzan 5 [294], a possible significant excess is possibly becoming significant towards 47 Tucanæ. If globular clusters formed in DM minihaloes (see Sec. 2.3.2), they were DM-dominated in their primordial stage and may be today potential targets for indirect DM searches [411].

The Galactic Globular clusters M 15 and NGC 6388 observed by H.E.S.S. have been studied in the context of dark matter searches. M 15 is a metal-poor GC, [Fe/H]$\simeq$-2.37 [412], while NGC 6388 is metal-rich, [Fe/H]$\simeq$-0.55 [412], the DM minihalo scenario is then better motivated for M 15 than NGC 6388. However, NGC 6388 might host a $\gtrsim 10^3\,\mathrm{M}_\odot$ black hole [200]. Such massive ($\gtrsim 10^3$ $\mathrm{M}_\odot$) black holes are not easily formed in star-forming events [413] which may suggest a primordial formation origin.

3.4.1 NGC 6388 and M 15 halo modelling

NGC 6388 located at 11.5 kpc from the Sun is one of the best known Galactic GC. Given the Galactic latitude of the two Galactic GCs, no contamination by diffuse TeV gamma-ray emission is expected. Using the high-resolution HST and WFI observations at ESO, the surface brightness density of stars significantly deviates from a flat core in the inner part, which is compatible with the existence of an IMBH with a mass of $\sim 5\times10^3\,\mathrm{M}_\odot$ [200]. A power law with a slope of -0.2 is detected in the surface brightness density profile, which suggests the presence of a central IMBH [414, 415, 416]. The *Chandra* satellite has detected three X-ray sources, coincident in position with the centre of gravity of NGC 6388 located with an uncertainty of $0.3''$. One of these may be the X-ray counterpart of the putative IMBH [417].

M 15 (NGC 7078) is a well-studied Galactic GC. The surface brightness density of the GC M 15 suggests the presence of a stellar cusp in the inner part, at least down to distances of a few $10^{-2}\,\mathrm{pc}$ [418]. M 15 may thus harbor an IMBH [419, 420] in its center. However, the study on millisecond pulsars in M 15 sets an upper limit of $10^3\,\mathrm{M}_\odot$ on the mass of a hypothetical central BH [421]. In what follows, no central back hole is assumed for the modelling of M 15. The relevant structural properties of NGC 6388 and M 15 for our purpose can be found in Tab. 1 of Ref. [422].

The H.E.S.S. observations of NGC 6388 were taken between June 2008 and July 2009 with a total exposure time of 27 hours, and those of M 15 in 2006

and 2007 resulting in 15 hours. The core of the globular clusters is very small in comparison to the H.E.S.S. point spread function and standard pointlike analysis is applied to data as presented in Ref. [422]. No significant gamma-ray signal at the nominal position of NGC 6388 and M M15, respectively, is found.

The relaxation time (see defined appendix of Ref. [422]) has a much smaller value, $T_r \sim 10^7$ yr, in globular clusters than in galaxies, where it is typically of the order of 10^{13} yr [**?**]. Since GCs are among the oldest objects known, their present DM density strongly depends on their history and evolution. During infall events such as core collapses [423], the DM is compressed towards the center following the AC scenario [197, 196] (referred to hereafter as the AC NFW profile). However, the kinetic heating of DM particles by stars [185] tends to wash out the adiabatic contraction effect over a timescale of the order of $\mathrm{T_r}$. Both effects were taken into account in the modelling of M 15 and NGC 6388, following the approach of Refs. [424, 425].

As mentioned in Sec. 2.3.2, the primordial formation scenario of globular clusters [190] assumes that globular clusters were formed in extended DM haloes. The DM halo profile of a globular cluster is thus modelled assuming an initial Navarro-Frenk-White (NFW) profile [16]. This DM halo is parameterized by a virial mass[1] $M_{\rm vir}$ and a concentration parameter $c_{\rm vir}$. The normalization parameter $\rho_{\rm s}$ and the scale radius $r_{\rm s}$ can be related to the virial mass and the concentration parameter using the following relations provided in Ref. [16] The present baryonic mass of the GC provides a lower bound on its virial mass. For $M_{\rm vir}$ larger than 10^8 $\mathrm{M_\odot}$ the GC would be expected to spiral towards the center of the Milky Way in less than the age of the Universe. Conservative values for $M_{\rm vir}$ lie therefore in the range $[5 \times 10^6 - 5 \times 10^7]$ $\mathrm{M_\odot}$ [411], corresponding[2] to $\mathrm{c_{vir}}$ between ∼48 and 65. Here, initial DM halos of GCs are modelled with $\mathrm{M_{vir}} = 10^7$ $\mathrm{M_\odot}$. The value of $c_{\rm vir}$ used in the model of NGC 6388 is calculated from Ref. [18]. For M 15, the value of $c_{\rm vir}$ is taken from Ref. [411].

The presence of a central BH changes the DM and stellar densities in regions where the BH dominates the gravitational potential, *i.e.* for distances to the BH lower than the radius of gravitational influence ${r_{\rm h}}^3$. The adiabatic growth of the BH leads to a spiked DM distribution with an index of 9/4 for an initial DM distribution with an index of 1, as for the NFW profile. This profile is referred to as the IMBH NFW profile. The spike is smoothed by the kinetic heating of DM by stars over the timescale $T_{\rm r}$, forming a density profile proportional to $\mathrm{r}^{-3/2}$

[1] $\mathrm{M_{vir}}$ is defined as the mass inside the radius $\mathrm{R_{vir}}$ assuming a mean density equal to 200 times the critical density of the Universe [426].

[2] $\mathrm{M_{vir}}$ and $\mathrm{c_{vir}}$ are strongly correlated [16, 18]. In Ref. [18], $\mathrm{c_{vir}} = 9 \times (\mathrm{M_{vir}}/1.5 \times 10^{13}\mathrm{h}^{-1}\mathrm{M_\odot})^{-0.13}$ where h is the present day normalized Hubble constant [426].

[3] The radius of gravitational influence of a BH is defined by the equation $\mathrm{M}(< \mathrm{r_h}) \equiv \int_0^{\mathrm{r_h}} \rho(\mathrm{r}) \mathrm{d}^3\mathrm{r} = 2\,\mathrm{M_{BH}}$.

called a *DM crest* [424], which corresponds to the profile today. An enhancement of few tens can be expected for the final dark matter profile.

Modelling of the M 15 dark matter halo

First, the initial dark halo is assumed to be adiabatically compressed during the collapse of the core of M 15. The model used for the initial DM and baryon densities is described in Ref. [411]. The final baryon density is the observed mass density taken from Ref. [427]. The DM is compressed during the baryonic collapse. The timescale for the collapse is $\simeq 100\, T_{\rm r}$, where the relaxation time $T_{\rm r}$ is given by [423] :

$$T_{\rm r} = \frac{3.4\times 10^9}{\ln\Lambda}\Big(\frac{v_{\rm rms}}{\rm kms^{-1}}\Big)^3\Big(\frac{m}{\rm M_\odot}\Big)^{-2}\Big(\frac{n}{\rm pc^{-3}}\Big)^{-1}{\rm yr}\ . \tag{3.1}$$

In Eq. (3.1), $v_{\rm rms}$ is the velocity dispersion, n is the stellar density and $\ln\Lambda$ is the usual Coulomb logarithm. In the case of the center of M 15, taking $v_{\rm rms} = 10.2\pm1.4\,{\rm kms^{-1}}$ ([418], $\ln\Lambda = 13.1$ and adopting a typical stellar mass value of $m = 0.4\,{\rm M_\odot}$ ([418], one finds $T_{\rm r} \simeq 7\times10^4$ yr. $T_{\rm r}$ is an increasing function of the distance r to the center of the M 15. For $r \gtrsim r_{\rm heat} = 5\,{\rm pc}$, the relaxation time is larger than the age of the Universe. The central value of $T_{\rm r}$ and the position of $\rm r_{heat}$ have only weak dependencies on the actual values of $v_{\rm rms}$ and n when the latter are varied in their uncertainty ranges. Because of adiabatic contraction, the DM evolution takes place in less than a few orbital periods. The orbital period of a star orbiting the core of M 15 is of the order of 1000 yr, which is much less than $T_{\rm r}$. The adiabatic contraction method should thus be valid. At the same time, the DM is heated up by stellar matter. This process is described in Ref. [185]. DM is scattered by stars in a few $T_{\rm r}$, leading to a depletion of the core. For $r \gtrsim 5\,{\rm pc}$, the DM distribution is not affected by heating. The DM scattering is taken into account with the procedure described in Ref. [425]. A DM mass density of $\rho_{\rm M15} \sim 35\,{\rm M_\odot pc^{-3}}$ is obtained at the radius where the heating time is comparable to the age of the universe. For $r \lesssim 5$ pc, the DM halo is swept out by heating and the DM mass density was assumed to take the constant value $\rho_{\rm M15}$. The DM mass density of M 15 called final profile is shown on the left panel of Fig. 3.16. The DM halo of M 15 differs from the model published in Ref. [411], since the effect of dark matter heating by stars is considered in addition to the effect of adiabatic contraction.

The dark matter halo modeling of the NGC 6388

The first step is the adiabatic contraction of the DM halo by the IMBH and baryons. An initial baryon fraction of 20% is assumed with the same spatial

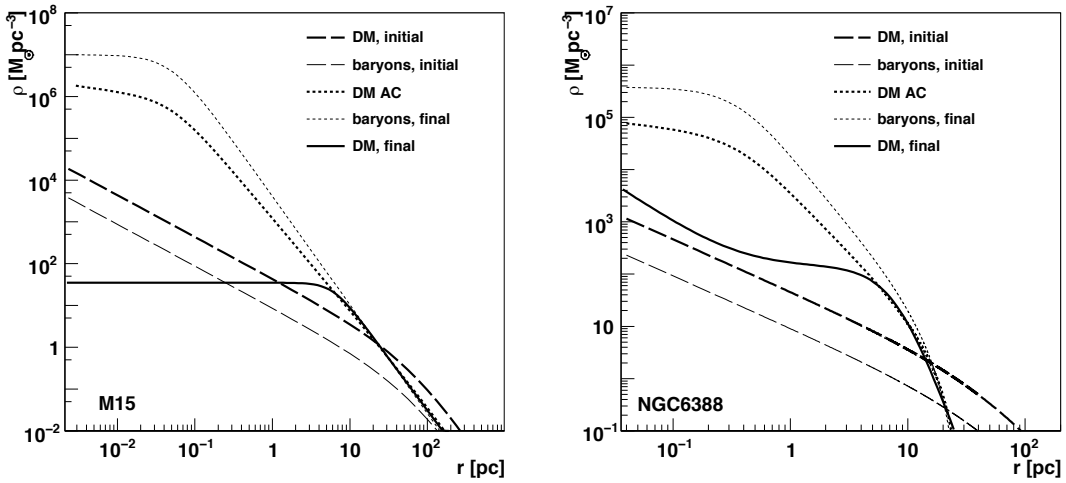

Figure 3.16: *Dark matter and baryonic density distributions in M15 and NGC 6388* ***Left panel:*** *The dark matter density before (thick dashed line) and after (thick dotted line) the AC by baryons is shown for M 15. The initial DM distribution follows an NFW profile with $M_{\rm vir} = 10^7\ M_\odot$. The initial (thin dashed line) and final (thin dotted line) baryonic densities are displayed. The final DM density distribution after the effect of the kinetic heating by stars is presented (thick solid line). See the text for more details.* ***Right panel:*** *Dark matter density before (thick dashed line) and after (thick dotted line) the AC by baryons is shown for NGC 6388. The initial DM distribution follows an NFW profile with $M_{\rm vir} = 10^7\ M_\odot$. The initial (thin dashed line) and final (thin dotted line) baryonic densities are displayed. The final DM density distribution after the effects of the adiabatic growth of the IMBH at the center of NGC 6388 and the kinetic heating by stars is presented (thick solid line).*

distribution as the DM. The AC scenario gives the resulting DM distribution knowing the measured baryonic mass profile. This DM halo profile is called AC NFW profile. The surface density profile of NGC 6388 is well fitted by a modified King model including a black hole, characterized by a core radius $r_{\rm c} = 7.2''$ and a concentration $c = 1.8$ [200]. Using these parameters, the numerical integration of the Poisson equation yields the behavior of the gravitational potential from which it is straightforward to compute the baryonic density profile. The initial NFW profile is characterized by $\mathrm{M_{vir}} = 10^7\,\mathrm{M_\odot}$. Since the mass of the IMBH is just a small fraction of the total mass in the core of NGC 6388, the dynamics of DM is influenced mainly by baryonic matter, except in the immediate vicinity of the black hole. Using a central velocity dispersion of $v_{\rm rms} = 18.9{\pm}0.8\ \mathrm{kms}^{-1}$ [428] and $\ln\Lambda = 14.7$, the central relaxation time is found to be $T_{\rm r} \simeq 8{\times}10^6$ yr. The orbital period of a star orbiting the core of NGC 6388 is 5000 yr, so that the AC method

is again valid. The relaxation time is larger than the age of the Universe for $r > r_{\rm heat}$. The distribution of the DM density around the black hole (for $\mathrm{r} \lesssim \mathrm{r_h}$) is changing with time, but tends to a power law with index 3/2 after a few $T_{\rm r}$. The final DM distribution is thus obtained by extending the prescription in Ref. [425]. Far from the center of the cluster, the stellar density is low and thus the heating time becomes large so that the DM distribution is unaffected. A mass density of $\sim$140 $\mathrm{M_\odot pc^{-3}}$ is obtained at the radius $r_{\rm heat} \sim 4\,\mathrm{pc}$ where the heating time is comparable to the age of the Universe. In the region between $r_{\rm h} < r < r_{\rm heat}$, the DM density is expected to be described by a smooth curve similar to Fig. 1 of Ref. [424]. In the modelling for NGC 6388, the DM density was conservatively assumed to take a constant value of $140\,\mathrm{M_\odot pc^{-3}}$ in the region $r_{\rm h} < r < r_{\rm heat}$. For $r < r_{\rm h}$, the DM density is given by $\rho(\mathrm{r}) = 140\,\mathrm{M_\odot pc^{-3}}\,(\mathrm{r/r_h})^{-3/2}$. The final profile for the DM distribution of NGC 6388 is shown in the right panel of Fig. 3.16. At the position of NGC 6388, the DM density from the smooth Galactic halo assuming a NFW profile is $\sim$0.03 $\mathrm{M_\odot pc^{-3}}$.

The astrophysical factors are then calculated for the above mentioned DM halo profiles. In the case of the IMBH NFW and final DM profiles for NGC 6388, the calculation of the astrophysical factor requires a minimum cutoff for the integration radius. For the IMBH NFW and final profiles, the integral diverges as $r_{\rm min}^{-3/2}$ and $\log(r_{\rm min}^{-1})$ respectively, where $r_{\rm min}$ is the inner radius. $r_{\rm min}$ is usually taken as $\mathrm{Max}[r_S, r_A]$ where $r_S \equiv 2GM_{\rm BH}/c^2$ is the Schwarzschild radius of the black hole and $r_{\rm A}$ is the self-annihilation radius calculated for an annihilation time of 10 Gyr. Typical values of m_{DM} and $\langle\sigma v\rangle$ give $\mathrm{r_A} \simeq 10^{-5}$ pc so that $r_{\rm min} = r_{\rm A}$. The value of the astrophysical factor for the final profile is insensitive to the assumed value of $r_{\rm min}$. The evolution of M 15 leads to a depletion of DM, implying a decrease of $\bar{J}$. In the case of NGC 6388, the effect of the BH in the stellar environment boosts $\bar{J}$ to a value higher than that obtained for the initial NFW profile.

3.4.2 Constraints and discussion

The left panel of Fig. 3.17 shows the 95% C.L. exclusion limits for NGC 6388 on $\langle\sigma v\rangle$ for the initial and the final profiles, respectively. The limits are one-to-three orders of magnitude above the natural value of the velocity-weighted annihilation cross section for thermally-produced DM. The right panel of Fig. 3.17 shows the H.E.S.S. 95% C.L. exclusion limits for M 15 for the initial and final DM profiles, as well as those obtained with the Whipple Cherenkov telescope (blue area) in [411]. The H.E.S.S. limits reach $\langle\sigma v\rangle \sim 5 \times 10^{-23}\,\mathrm{cm^3 s^{-1}}$ and $\langle\sigma v\rangle \sim 5 \times 10^{-24}\,\mathrm{cm^3 s^{-1}}$ around $m_{\rm DM} = 2$ TeV for the initial NFW profile and the final profile respectively. For comparison, the exclusion limit obtained for H.E.S.S. using the DM halo modelling of [411] are also shown (gray area).

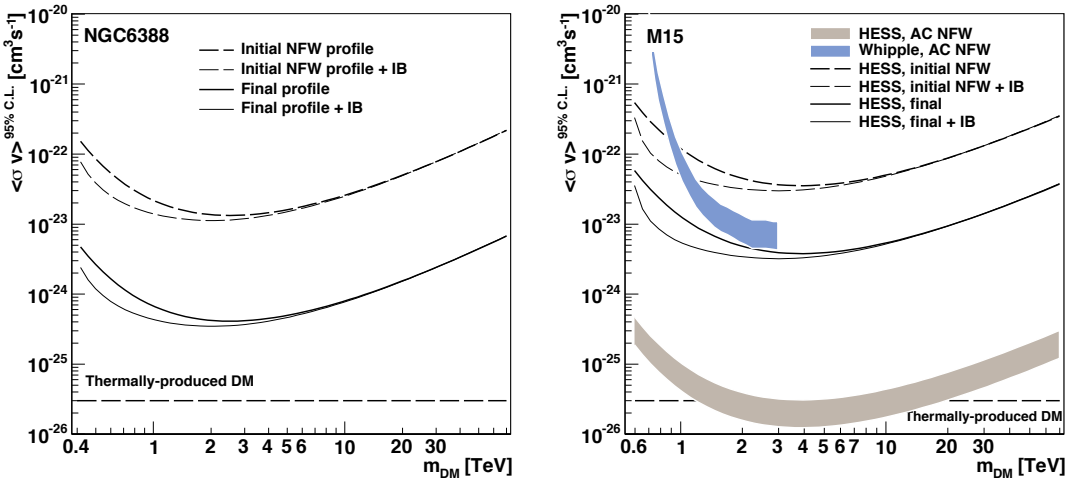

Figure 3.17: *H.E.S.S. upper limits at 95%C.L. the velocity-weighted annihilation cross section $\langle\sigma v\rangle$vs. the DM mass $m_{\rm DM}$ for the Galactic globular clusters NGC 6388 (left panel) and M 15 (right panel). The thickness of the drawn lines for M 15 represents the astrophysical uncertainty induced by the plausible mass range for the initial virial mass. The natural value of $\langle\sigma v\rangle$for thermally-produced DM is also displayed (long-dashedline).The contribution from internal bremsstrahlung and final state radiation to the annihilation spectrum is also shown(dashed/solid thin lines). See text details on the DM halo profiles. For M 15, the H.E.S.S. limits for the AC NFW profile used in Ref. [411] together with the Whipple exclusion limits [411] are also plotted (blue area).*

The DM halo in globular clusters can be modelled taking into account all relevant astrophysical effects affecting the hypothetical initial DM halo: the adiabatic contraction of DM by baryons, the adiabatic growth of a BH at the center of the DM halo, and the very efficient scattering of DM by stars in such a dense stellar environment. This effect is of crucial importance to model DM halos in these baryon-dominated environments and leads to a depletion of DM during the evolution of the globular cluster.

The formation scenario of globular clusters is still very uncertain. Although the possibility of their formation in DM mini halos is not excluded, more conventional scenarii include formation in merging and interacting galaxies, with the possibility of formation at the present epoch [189]. Interestingly, high-energy gamma-ray signals have been detected towards Galactic globular clusters with a large population of millisecond pulsars with Fermi-LAT observations [366]. In particular, a VHE emission has been detected by H.E.S.S in the direction of

Terzan 5 [429]. The collective emission from a population of millisecond pulsars may likely be a prime scenario to explain the emission at VHE gamma-ray energies.

3.5 The galaxy cluster Fornax

3.5.1 H.E.S.S. observations and halo modelling

The Fornax (distance = 19 Mpc), Coma (distance = 99 Mpc) and Virgo (distance = 17 Mpc) galaxy clusters are in principle promising targets for dark matter searches through gamma-rays [275]. The radio galaxy M 87 at the center of Virgo provides a strong astrophysical gamma-ray signal [430], showing flux variabilities from daily to yearly timescales that exclude the bulk of the signal to be of a DM origin. Since a DM gamma-ray signal would be hard to disentangle from this dominant standard astrophysical signal, Virgo is not a prime target for DM searches, even though a DM signal may be hidden by the dominant gamma-ray signal from standard astrophysical sources. Given the location of H.E.S.S., Fornax is the preferred galaxy cluster target for dark matter searches because the most favorable observation conditions can be achieved in its direction.

The ΛCDM prediction of cuspy DM halo profile is a priori more robust for large-scale structures where the impact of baryonic physics is expected to be modest compared to the case of galaxy-scale structures. NFW profiles are currently used to model the DM distribution in galaxy clusters. However, in scenarios where the baryon infall in the DM gravitational potential efficiently transfers energy to the inner part of the DM halo by dynamical friction, a flattening of the density cusp into a core-halo structure is expected. The halo can be modeled using the Burkert parametrization.

A commonly-used approach for the determination of the DM halo in galaxy cluster comes from X-ray measurements of the gravitationally bound hot intracluster gas. From the HIFLUGCS catalog [281], the virial mass and radius of Fornax are found to be $M_{vir} \sim 10^{14}$ $M_\odot$ and $R_{vir} \sim 1$ Mpc (corresponding to about 6° in angular diameter), respectively. Under the assumption of a NFW halo profile in ΛCDM cosmology, a relation between the virial mass and the concentration parameter $c = R_{vir}/r_s$ can be found, see, for instance, Ref. [431]. The halo parameters can thus be expressed in terms of ρ_s and r_s. This model is hereafter referred as to RB02. A similar procedure was applied in the Fermi-LAT DM analysis of galaxy clusters [284].

An alternative approach is to use dynamical tracers of the gravitational potential of the cluster halo, such as stars, globular clusters or planetary nebulae. This method is limited by the observability of such tracers, but can yield less

model-dependent and more robust modeling of the DM distribution. However, some uncertainty is introduced by the translation of the tracers velocity dispersion measurement into a mass profile, which usually implies solving the Jeans equations under some simplifying assumptions. From velocity dispersion measurements on dwarf galaxies observed up to about 1.4 Mpc, a dynamical analysis of the Fornax cluster conducted in Ref. [432] constrained the cluster mass. The associated DM density profile, hereafter referred as to DW01, can be well described by a NFW profile [24].

The DM distribution in the inner region of Fornax can be inferred by using the globular clusters as dynamical tracers [24]. This allowed an accurate DM mass profile measurement out to a radial distance of 80 kpc from the galactic cluster centre, corresponding to an angular distance of $\sim$0.25°. The resulting velocity dispersion measurements can be well fitted by a NFW DM halo profile. This density profile (hereafter referred as to RS08) determination is in good agreement with the determination inferred from ROSAT-HRI X-ray measurements [433]. Detailed analysis using subpopulations of globular clusters done in Ref. [25] showed that both a NFW and a Burkert DM halo profiles can equally well fit the globular cluster velocity dispersion measurements. Representative DM halo profiles using different sets of globular clusters samples, hereafter referred as to SR10 a6 and SR10 a10, are extracted from Table 6 of Ref. [25].

Using the dark matter halo parameters derived from the above-mentioned methods, values of J were derived for different angular integration radii. Most often the smallest possible angle is used in the search for dark matter signals in order to suppress background events. However, since a sizable contribution to the gamma-ray flux may also arise from dark matter subhalos located at larger radii (see Sec. 2.1.3), integration angles up to 1.0° were also considered. The choice of the tracer samples induces a spread in the values of the astrophysical factor up to one order of magnitude. Note that the measurements of Ref. [24] and Ref. [25] trace the DM density distribution only up to 80 kpc from the center. In consequence the derived values of the virial mass and radius are significantly smaller than those derived from X-ray measurements on larger distance scales (see for instance Fig. 22 of Ref. [25]. Thus the DM density values may be underestimated for distances larger than about 100 kpc. However, for a NFW profile about 90% of the DM annihilation signal comes from the volume within the scale radius r_s. Therefore, even for NFW models with large virial radii such as RB02 and DW01, the main contribution to the annihilation signal comes from the region inside about 98 kpc and 220 kpc, respectively.

3.5.2 Constraints on annihilating dark matter

No significant excess was found above the background level in any of the integration regions from 0.1° to 1°. Flux constraints are derived from $\sim 10^{-12}$ to $\sim 10^{-11}$ cm^{-2}s^{-1} for 0.1° and 1° integration regions, respectively. Together with the J-factor determination, constraints on $\langle \sigma v \rangle$ are obtained.

Studies conducted in Refs. [275, 273, 434] have computed the cosmic-ray induced gamma-ray flux from pion decays using a cosmological simulation of a sample of 14 galaxy clusters [435]. Since the electron induced gamma-ray flux from inverse Compton is found to be systematically subdominant compared to the pion decay gamma-ray flux [275], this contribution is not considered. Using the results in Ref. [273], the gamma-ray flux above 260 GeV for Fornax is expected to lie between a few 10^{-15} cm^{-2}s^{-1} and 10^{-14} cm^{-2}s^{-1} for an opening angle of observation of 1.0°. The flux is about 2-to-3 orders of magnitude lower than the flux upper limits, thus this scenario cannot be constrained.

Fig. 3.18 shows the exclusion limits as a function of the DM particle mass for different DM halo profile models (left) and various annihilation channels (right). Stronger constraints are obtained for masses below 1 TeV in the $\tau^+\tau^-$ where the 95% C.L. upper limit on $\langle \sigma v \rangle$reaches 10^{-23} cm^{3}s^{-1}. In the annihilation of DM particles to charged final states, internal bremsstrahlung processes can contribute significantly to the high-energy end of the gamma-ray spectrum. The internal bremsstrahlung affects the exclusion limits mostly in the low mass DM particle regime, where its contribution to the total number of gamma-rays in the H.E.S.S. acceptance is the largest.

Some dark matter models predict the annihilation to occur predominantly to lepton final states [127, 437]. The subsequent muon decay into positrons and electrons may lead to an additional gamma-ray emission component by Inverse Compton (IC) up-scattering of background photons, such as those of the cosmic microwave background (CMB). If the electron/positron energy loss time scale is much shorter than the spatial diffusion time scale, the IC contribution to the gamma-ray flux may be significant. In galaxy clusters, the energy loss term is dominated by the IC component. The total gamma-ray spectrum is then given by the FSR and IC components. The FSR parametrization is extracted from Ref. [438]. The IC component of the annihilation spectrum was calculated following the method described in Ref. [439]. The energy E_γ^{IC} of the IC emission peak is driven by electrons/positrons of energy $E_\mathrm{e} \simeq m_\mathrm{DM}/2$ up-scattering target photons in a radiation field of average energy $\epsilon = 2.73$ K and is given by $\mathrm{E}_\mathrm{IC}^\gamma \simeq \epsilon(\mathrm{Ee/me})^2$. Consequently, the enhancement of the gamma-ray flux in the H.E.S.S. energy range is found to lower the exclusion limits only for very high DM masses, $\mathrm{m_{DM}}$ >10 TeV [285]. The limits are enhanced by a factor of ∼10. Due to the IC component, below a few tens of TeV the Fermi-LAT

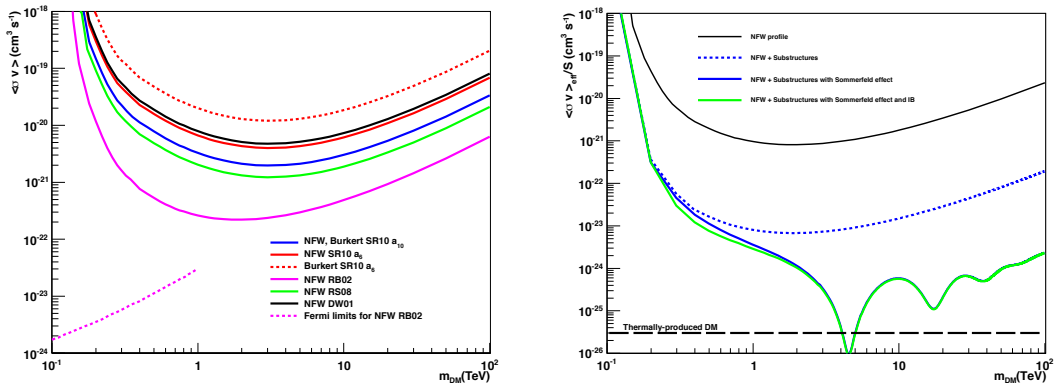

Figure 3.18: *Upper limit at 95% C.L. on the velocity-weighted annihilation cross-section $\langle\sigma v\rangle$as a function of the DM particle mass towards the cluster of galaxies Fornax with H.E.S.S.* ***Left panel:*** *Various DM halo profiles are considered: NFW profiles, SR10 a_{10} (blue solid line), DW01 (black solid line), RB02 (pink solid line) and RS08 (green solid line), and Burkert profiles, SR10 a_6 (red dotted line) and a_{10} (blue solid line). DM particles are considered to annihilate purely into $b\bar{b}$ pairs for an integration angle $\theta_{\rm max}$ = 0.1°. The* Fermi*-LAT upper limits [436] for the NFW profile RB02 are also plotted.* ***Right panel:*** *Exclusion limits including the Sommerfeld effect and the effect of halo substructures. The upper limits at 95% C.L. are computed for $\theta_{\rm max} = 1.0°$, the W^+W^- channels and the RB02 halo model. The solid green and blue lines show limits for the case of Wino dark matter annihilation enhanced by the Sommerfeld effect, with and without including Internal Bremsstrahlung, respectively. Figures extracted from Ref. [285].*

results provide stronger limits than the H.E.S.S. results. However, since for DM particle masses above 10 TeV the IC emission peak falls out of the Fermi-LAT energy acceptance, the IC spectra becomes harder in the same energy range. The Fermi-LAT limits for DM particle masses above 10 TeV would tend to raise with a stronger slope than the slope in between 1 and 10 TeV. Thus H.E.S.S. limits would well-complement the Fermi-LAT constraints in the DM mass range higher than 10 TeV. In the TeV range the 95% C.L. upper limit on the annihilation cross-section reaches $\sim 10^{-22}$ cm^{3}s^{-1}. In the right panel of Fig. 3.18, the joint enhancement due to the Sommerfeld effect[1], the IB and the substructures contributions is shown. In the most optimistic model, with the largest enhancement by substructures and the Sommerfeld effect, the 95%

[1]In the Fornax galaxy cluster, the velocity dispersion and hence the mean relative velocity of test masses such as stars, globular clusters or galaxies is of the order of a few 100 km s^{-1} [25], hence $\beta =< v_{\rm rel} > /c \approx 10^{-3}$. We assume that the same velocity distribution holds true for DM particles.

C.L. upper limit on $\langle\sigma v\rangle$ reaches 10^{-26} cm^{3}s^{-1}, thus probing natural values for thermally-produced DM.

The constraints with IACTs on annihilating dark matter are orders of magnitude above the natural scale. Assuming boost factors from substructures in the galaxy cluster halo makes them relevant for TeV dark matter. However, the expectations for the substructure boost in galaxy clusters are subject to strong debate.

3.5.3 Decaying dark matter and prospects with CTA

Galaxy clusters are a promising target for decaying DM. While the signal originating from annihilating DM scales with the square of the DM density, for decaying DM the dependence is on the first power. As a consequence, dense DM concentrations shine above the astrophysical backgrounds if annihilation is at play, but remain comparatively dim if DM is decaying. Decaying DM wins instead, generally speaking, when large volumes are considered.

The selection of the galaxy cluster for decaying DM searches goes along the same line as for annihilating DM ones. From the H.E.S.S. observations, the Fornax galaxy cluster is privileged as mentioned above. In contrast to annihilating dark matter for which most often the smallest opening angle provide the most sensitive searches for cuspy profiles when no substructure contribution is considered, decaying dark matter searches require optimization of the opening angle to guarantee the highest signal-to-noise ratio. The luminosity scales with the size of the solid integration angle. On the other hand, background is increasing as well. The optimization of the signal-to-noise ratio versus the opening integration angle for the dark matter halo profile RB02 provides the integration region to be 0.5∘ [143].

The decaying signal is searched for the X-ray-based determination of the DM profile (RB02 profile), which also well agrees with tracer dynamics at large distances. As an alternative choice, we also considered the DW01 profile, which is fully based on the dynamical tracers method. This generates a predicted DM gamma-ray flux 3 times smaller than RB02. The contribution of the inverse Compton emission in case of leptonic final states is considered. As opposed to dwarf galaxies, in clusters the electrons lose energy primarily through ICS on the ambient radiation field and produce additional gamma rays in the final state. This contribution is included in the computations for the $\mu^+\mu^-$ channel, but, due to the energy working range of H.E.S.S., this component becomes important only for very large DM masses above 30 TeV. For more details on the analysis and computation of the limits, see Ref. [143].

Figure 3.19 shows the 95% C.L. upper limits of H.E.S.S. and sensitivity of CTA on the decay lifetime for the RB02 halo profile for 50 h observation time together

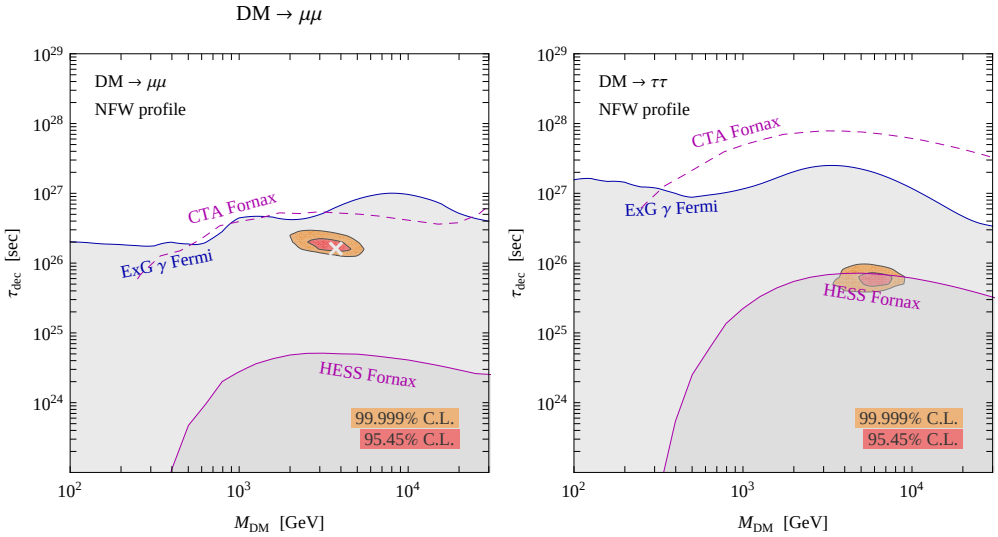

Figure 3.19: *The regions on the parameter space $m_{\rm DM}$-$\tau_{\rm dec}$ for the $\mu^+\mu-$ (left panel) and $\tau^+\tau^-$ (right panel) channels, respectively, that are excluded by the Fermi and H.E.S.S. constraints and that can be explored by CTA, together with the regions of the global fit to the charged CR data, for different decay channels. Figure extracted from Ref. [143].*

with the regions of the global fit to the charged CR data, for two decay channels. The constraints by Fermi-LAT rule out decaying half-lives of the order of 10^{26} to few 10^{27} seconds. These limits therefore exclude the decaying DM interpretation of the charged CR anomalies, (at least) for all 2-body channels. The constraints by H.E.S.S. are generally subdominant. For the $\tau^+\tau^-$ channel, they can however also probe the CR fit regions and essentially confirm the exclusion. With CTA observations of Fornax, decaying half-lives up to 10^{28} seconds for TeV dark matter masses could be probed [143].

3.6 Outlook

The near-future priority in the strategy for heavy WIMP dark matter searches with arrays of IACTs should be the discovery of the nature of dark matter with a positive detection. To this aim, the prime target is the inner galactic halo of the Milky Way. The observations should focus on the center of the Milky Way, with several hundred hours distributed in the inner several degrees of the Galactic Center in order to provide sensitivities below the thermal relic cross-section for WIMPs. Since the dark matter density in the Galactic halo is far from certain, the secondary targets are ultra-faint dwarf galaxies. The most interesting one is still subject of debate in this rapidly evolving field, both due to

the new detections of nearby ultra-faint dwarf galaxies by current optical surveys, and the progress made in the understanding of their dark matter distribution and uncertainties. While the dwarf galaxies provide an excellent environment to provide an unambiguous detection a dark matter signal, the achieved sensitivity towards these objects is still far from what can be achieved in the Galactic Center region.

The dark matter profile in the inner region of the Milky Way is uncertain. The Galactic Centre is a complex environment and a number of astrophysical processes may change the initial density. At the Galactic center, stars and the supermassive black hole dominate the gravitational potential and the dark matter distribution is expected to evolve on sub-parsec scales due to interaction with these components. Cosmological simulations including baryon feedback with improved spatial resolutions would definitely help to further investigate the dark matter distribution in the very challenging region of the inner kpc of the Galactic Centre. However, there is no consensus so far.

The inner Galactic halo is a very complex region at VHE gamma-ray energies as shown in the Chapter 4 with several extended diffuse emissions that challenge the detection of a dark matter signal. Among them are the Galactic diffuse emission, possible emission of the Fermi bubbles in the VHE range, and the TeV emission from the Galactic Center Pevatron. Future analyses will make use of multi-template analysis technique taking into account the spectral and spatial morphology of the search signal and astrophysical backgrounds. On top of that, while the expected CTA sensitivity in the Galactic Center can potentially probe the thermal relic cross-section for heavy WIMPs, significant efforts should be made to control the systematic uncertainty from the background modelling and subtraction using precise determinations of the standard astrophysical emissions, and the understanding of the instrumental and observational systematics.

Chapter 4

The Galactic Centre region in very-high-energy gamma rays

Contents

This chapter provides a short overview of very-high-energy gamma-ray astrophysics in the Galactic Centre region[1]. The main characteristics of the inner few hundred parsecs of the Galactic Centre are presented in the context of VHE gamma-ray observations. The high and very high energy observations of the Central Molecular Zone, with an emphasis on the central source HESS J1745-290 are introduced. Forecast observations of HESS J1745-290 with CTA are presented in the context of an attempt to unveil its origin. The very-high-energy diffuse emission measured by H.E.S.S. is discussed in the context of the discovery of the first Galactic PeVatron. Near-future perspectives are then presented. A significant part of the studies shown here has been carried out during the PhD theses of Aion Viana [310], Valentin Lefranc [311] and Lucia Rinchiuso [312].

4.1 Introduction

4.1.1 The supermassive black hole Sagittarius A*

As we zoom in the Galactic centre, radio wavelength observations reveal in 1974 a point like ($\sim 5''$) source Sagittarius (Sgr) A*. Observed motions of gas and stars collected over more than two decades conclusively indicate the presence of a massive object lying in the center of our Galaxy. Velocities of the gas showed that a mass of several 10^6 $M_\odot$ is located in the inner $10''$ of Sgr A*. This evidence has been confirmed by stellar motion measurements. Near-infrared high-spatial resolution observations are able to accurately measure the motions of the stars of the central stellar cluster. Using the orbital velocity and position of the stars, one can estimate the mass contained within their orbits. The enclosed mass is $\sim 4\times 10^6$ $M_\odot$[2]. The mass of the central object can be measured with great accuracy. See, for instance, Refs. [440, 441, 442, 443]. The star's orbits are consistent with a pure Kleperian motion around a point mass centered on the Sgr A* radio position. Strong constraints on the position of the Sgr A* radio source from VLBA measurements with respect to the gravitational barycentre of the galaxy are obtained. mm-wavelength VLBI observations resolved the size of the radio source down to about 20 Schwarzschild radii[3]. These observations show undoubtedly the presence of a massive black hole in Sagittarius A*. See excellent reviews in Refs. [444, 445, 446] for further details.

The distance of the Galactic centre has been measured via a wealth of methods [447]. Among them are the stellar orbits close to Sgr A*, globular cluster

[1]The search for dark matter in the Galactic Centre region is covered in Chap. 3.

[2]Following the spectacular image of the supermassive black hole in M87 and the subsequent measurements of its properties, the EHT collaboration is being focused on Sagittarius A*.

[3]The Schwarzschild radius for Sagittaris A* is 1 $R_S \simeq 4\times 10^{-7}$ pc.

distribution, RR Lyræ stars and cepheids. All the methods yield values between 7 and 9 kpc. A commonly adopted value in literature is $r_\odot = 8.5$ kpc.

4.1.2 The inner 50 parsecs of the Galactic Center

The radio image of the central 50 pc harbors a prominent radio complex Sgr A as seen in Fig. 4.1. In addition to the bright radio source Sgr A* at the dynamical centre of the Galaxy, a non-thermal source Sgr A east identified as a shell-like remnant of a supernova which occurred about 10^4 yrs, and the HII region Sgr A West with a thermal radio spectrum, also known as the *Central Cavity*. Around it is an asymmetric torus of neutral hydrogen gas and dust named as the Circumnuclear Ring (CNR) orbiting Sgr A*. The CNR asymmetric and clumpy with a sharp inner radius a $\sim$1 pc and a more blurry outer boundary at 2.5 - 3 pc to the northeast and 4.7 pc to the southwest, with an inclination of $\sim$69° to the plane of the sky, and tilt of $\sim$20° to the Galactic plane. The hydrogen density reaches 10^5 cm^{-3} with a total mass of $\sim 10^4$ M$_\odot$. An extended radio halo of 20 pc is seen from 20-cm radio observations surrounds Sgr A East shell. The Sgr A complex contains two massive molecular clouds M-0.02-0.07 and M-0.13-0.08 peaking at 3' east and 2.5' south of Sgr A*, respectively, also labelled as the 50 km s^{-1} and 20 km s^{-1} clouds. In the 10 pc region are located the Arches, Quintuplet and central stellar clusters, the latter one being coincident in position with Sgr A* with an extension of about 0.4 pc.

4.1.3 The Central Molecular Zone

The central molecular zone (CMZ) is a dense region of activity stretching of about 300 pc in Galactic longitudes. It contains about 8% of the total gas of the galaxy, a reservoir of material of about 10^7 M$_\odot$. It hosts giant molecular clouds and massive star forming clusters. Dust along the line of sight makes it obscure in visible light and only infrared, radio and some X-ray observations can penetrate. 90-cm VLA radio observations towards the GC reveal a complex structure of the CMZ [448] as shown in Figure 4.1. Several supernova remnants are identified, such as G0.9±0.1, and large concentrations of ionized/molecular gas with densities higher than 10^4 cm^{-3} such as Sgr B1, Sgr B2, Sgr C and Sgr D are visible. Several filaments, such as the radio arc, oriented perpendicular to the Galactic plane show highly polarized radio emission.

The bulk of the gas in the CMZ is in the form of molecular hydrogen which is very difficult to detect. Methods to estimate the mass of molecular hydrogen use tracer molecules whose ratio to H_2 is approximately known. The CMZ has been first mapped in the 1970s with ^{12}CO and ^{13}CO lines, however these lines suffer from background and foreground contamination from the Galactic disk making

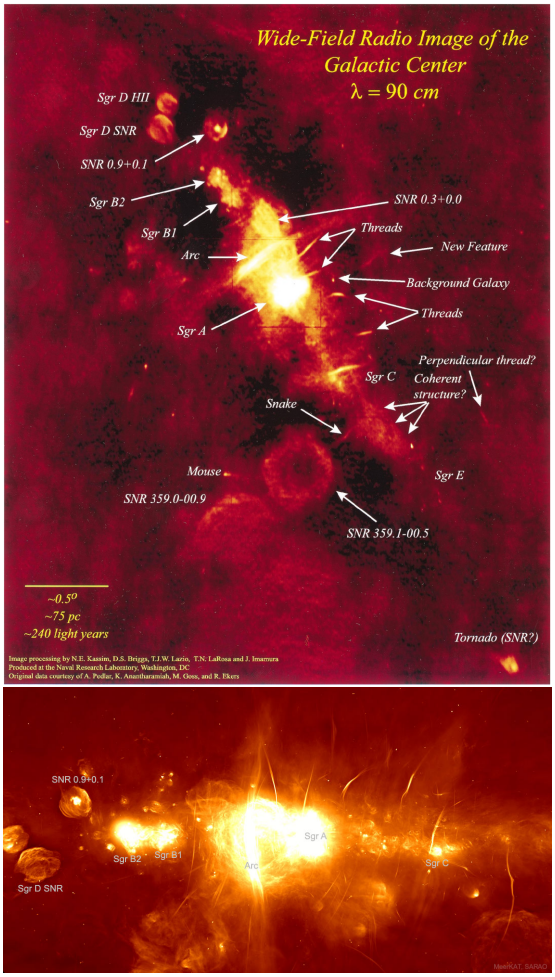

Figure 4.1: ***Top panel:*** *90-cm image of the GC region from radio observations with the VLA in equatorial coordinates. The Galactic plane is oriented from top-left to bottom-right. SNRs and PWNe are mentioned together with thread-like filaments, emitting synchrotron radiation from relativistic electrons. The GC is located in the Sgr A complex. The region from Sgr D to Sgr E is approximately 300 pc and is known as the CMZ. Figure extracted from Ref. [448].* ***Bottom panel:*** *The Galactic centre in radio from MeerKAT in Galactic coordinates.*

difficult precise mass measurements. In the velocity range of interest for the GC region, the carbon monosulfide (CS J $= 0 \rightarrow 1$) line emission is expected to be devoid of such contamination. In order to evaluate the systematic uncertainties in mass estimates, other channels, such as the line emission from transitions of $^{12}C^{16}O$ and HCN molecules, are also used. Compared to other tracer molecules, the critical density of the CS emission is relatively large and thus the CS emission is an efficient tracer to probe dense gas clouds. The total mass in the inner 150

pc of the CMZ is estimated to be $3^{+2}_{-1}\times10^7$ $M_\odot$ [449, 450]. Several parameters such as molecule density, excitation energy, absorption along the line-of-sight, influence the observability of the line emission of a molecule. One takes advantage to trace the emission from different types of molecules to get a consistent view of the CMZ gas content. The MOPRA CMZ survey measures a large number of complex molecules which complements earlier works [451] with data recently released [452].

Far infrared and sub-millimetre wavelength observations provide a tracer of dust in the CMZ, which itself traces the molecular gas content. Herschel infrared observations suggest that the mass of the molecular gas in the CMZ is about 3×10^7 $M_\odot$ [453]. A mass of 5.7×10^7 $M_\odot$ is derived form the SCUBA sub millimeter survey of the CMZ [454]. High-resolution X-ray observations conducted with the Chandra satellite revealed more than 9000 X-ray sources, some of them showing non-thermal X-ray emission from PWNe and SNRs [455].

The CMZ itself is divided into an inner disk with radius 120 pc and $\sim 4 \times 10^6$ $M_\odot$ mass, and a $\sim 1.6 \times 10^7$ $M_\odot$ outer torus. The disk/torus structure has a FWHM thickness 45 pc and a total hydrogen mass $\sim2\times10^7$ $M_\odot$ [456].

4.2 The inner 10 parsecs at very high energies

4.2.1 The central GeV-TeV gamma-ray source

Long time recognized as a possible TeV particle accelerator, the GC has been the focus of early ground-based observations by IACTs. In 2004, a VHE signal from the GC has been detected by the Whipple [457], Cangaroo-II [458] and H.E.S.S. [459] instruments. The detection of a point-like emission has been reported with no hints for flux variability. Hereafter this source is referred as to HESS J1745-290.

The Whipple instrument detected the emission at 3.7σ above an energy threshold of 2.8 TeV because of large zenith angle observations [457] due to its location in the northern hemisphere. A significant detection above 250 GeV has been reported by the Cangaroo-II instrument in Australia with a measurement of its energy spectrum steeply declining with a photon power law index of 4.6 ± 0.5 [458]. H.E.S.S. observations conducted in 2003 with two telescopes revealed a clear detection of the emission with a hard power-law spectrum of a power law of index $2.20\pm0.09_{\rm stat}\pm0.15_{\rm syst}$ with an energy threshold of 160 GeV. The H.E.S.S. result was latter confirmed with the complete array [460] and the MAGIC instrument [461]. The VERITAS collaboration recently released a new measurement of the spectrum above en energy threshold of 2.5 TeV that matches well H.E.S.S. and MAGIC results [462].

The H.E.S.S. instrument provides the most favorable view of the GC region to date due to its location in the Southern hemisphere providing a low energy threshold and good photon statistics at the highest energies. 93 hours of observations (live time) conducted between 2004 and 2006 revealed for the first time a significant deviation from a pure power law spectrum, and the spectrum is better described by a power law with an exponential energy cut-off with a photon index of 2.1 and cut-off energy at ∼15 TeV [463]. The data are equally described by a smoothed broken power law, a pure power fit to the data is rejected. Data collected from 2004 to 2013 resulting in 226 hour live time on Sgr A* confirmed this results and provided a refined measurement of the energy cut-off at ∼10 TeV in agreement with the previous measurement given the present statistical and systematic uncertainties. When compared with a pure power law, the likelihood-ratio test gives a p-value of 3×10^{-5} [296].

With the present uncertainties in H.E.S.S. measurements, a super-exponential cut-off versus an exponential cut-off power law fit to the data cannot be significantly preferred [311].

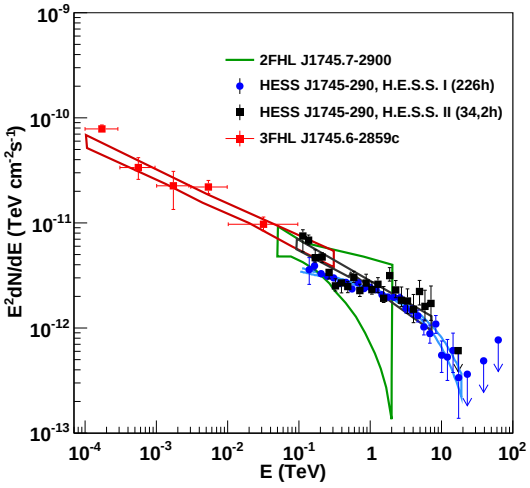

Figure 4.2: *HESS J1745-290 spectrum with H.E.S.S.-II data (black points) and 10 years of data taken with H.E.S.S. I (blue points). Also plotted are the spectrum of 2FHL J1745.7-2900 (green band) and 3FGL J1745.6-2859c (red points, red band) from the second and third Fermi-LAT catalogs, respectively. Bands give 1σ statistical error bars. Figure extracted from Ref. [311].*

With the addition in 2012 of a fifth telescope with 600 m^2 mirror area to the centre of the array, the H.E.S.S. instrument has increased the accessible energy

range, enabling observations to take place below 100 GeV. This marked the start of the second phase of H.E.S.S. This wider energy range allows an important overlap in observations with satellite instruments such as Fermi-LAT. The spectrum derived from data taken in 2013-2014 is well described by a power law model consistent with previously publish results [463, 296]. Though previous results show a significant energy cut-off in the spectrum, no significant evidence is found in the present dataset given the limited exposure compared to the much larger one from H.E.S.S.-I observations [463, 296]. Fig. 4.2 shows the spectrum of HESS J1745-290 seen with the 2013-2014 dataset together with the one seen with the full H.E.S.S.-I dataset. At low energies, the H.E.S.S. II spectrum extends down to 110 GeV, into the energy range covered by the Fermi-LAT telescope.

GeV observations

GeV observations are much prone to Galactic diffuse emission making the identification of sources in the Galactic Centre region more difficult than at VHE energies. The relative intensity of the diffuse emission is strongly reduced from the GeV to TeV energy domain, and the angular resolution improved. The identification of sources is then easier using high energy event selection but at the expense of photon statistics.

Coincident in position with the GC are the 2FHL J1745.7-2900 and 3FGL J1745.6-2859c. In the third Fermi-LAT catalog [464], HESS J1745-290 is associated with 3FGL J1745.6-2859c, recently confirmed in the fourth catalog [465]. In the second Fermi catalog, the corresponding source 2FGL J1745.6-2858, had a large enough position offset and was not firmly associated with the TeV source. The Fermi-LAT localization accuracy for a point source depends on its brightness and that of the surrounding diffuse emission, and is about 9 arcmin for 3FGL J1745.6-2859c. The spectrum of 2FHL J1745.7-2900 and 3FGL J1745.6-2859c from the second and third Fermi-LAT catalogs are shown in Fig. 4.2. Comparison of flux levels shows a good consistency between the H.E.S.S. and Fermi-LAT measurements. A power law model with an exponential energy cut-off is able to describe well the central emission in the ten MeV to ten TeV energy range. The Galactic center at GeV energies is a very complex region and detailed studies will help to further characterize the link between the GeV and TeV emissions. However, 3FGL J1745.6-2859c is likely to be the low energy counterpart of HESS J1745-290.

4.2.2 Origin of the GeV-TeV central emission ?

Significant progresses have been done to obtain a consistent picture of the GeV and TeV emission coincident in position with the GC. However, the underlying

mechanism for this point-like emission is not yet understood. Compared to radio or X-ray observations, the identification of the counterpart candidate at GeV/TeV energies is hampered by the large region covered by the gamma-ray emission in this densely populated environment.

Emission models that attempt to reproduce the GeV/TeV emission should at least possess the following characteristics *(i)* a power law spectrum from 100 MeV to 20 TeV with possibly a break at some tens of GeV, and an energy cut-off at $\sim$10 TeV, *(ii)* no hint for variability on timescale from minutes to years[1], *(iii)* The emission region of the H.E.S.S. source is point-like and coincident with the position of Sgr A*, and its intrinsic size is less than $\sim$1 arcmin. *(iv)* A possible moderate extension of the GeV source.

At TeV energies, Sgr A* is a compelling counterpart to HESS J1745-290 but two other objects in the vicinity of the black hole should be considered: the SNR Sgr A East and the PWN G359.95-0.04 [466] detected by the Chandra satellite. In addition, a cumulative emission from a large population of millisecond pulsars could also produce the gamma-ray emission [467].

Sagittarius A East

The Sagittarius A East SNR could in principle be responsible for the emission of HESS J1745-290 with protons accelerated in the extended shell of the SNR. Despite the relatively poor angular resolution of gamma-ray instruments, the position of the source centroid can be precisely defined given that the uncertainty on the centroid position scales as $\theta/\sqrt{N}$ with θ the angular resolution and N the number of gamma-ray detected. Based on precision measurements of the centroid of HESS J1745-290, Sgr A East is strongly disfavored as the main counterpart of the VHE emission. The position is coincident with the position of the supermassive black hole Sgr A* within a total error circle radius of 13″ at 68% C.L., a region which is significantly separated from the centroid of the radio emission from Sgr A East. This precision is achieved through a careful investigation of the pointing systematics of the H.E.S.S. instrument [468]. Such a conclusion cannot be drawn for the Fermi-LAT source given the limited photon statistics and systematic errors arising from the Galactic diffuse emission modelling.

G359.95-0.04

The PWN candidate G359.95-0.04 lies within the region of the HESS J1745-290 centroid position. Its position is about 9″ from Sgr A* and given the ability of

[1]The sensitivity to flare detection is limited by the photon statistics and crucially depends on the flare duration. An increase of a factor two on the quiescent flux is needed to get a significant detection for a few hour flare duration [463].

HE and VHE instruments for position measurements, it is impossible to spatially discriminate between these two objects. The X-ray spectrum steepens with distance to the pulsar location, which indicates that the electrons are cooled down by synchrotron radiation. High-energy electrons from the PWN can account for the X-ray emission of G359.95-0.04 and the VHE emission of HESS J1745-290: the dense interstellar radiation fields provide adequate conditions for the electrons to up-scatter IR target photons toVHE energies via the IC process [469]. However, with the advent of the Fermi-LAT detection, the GeV emission from this model underestimates by far the luminosity of the 2FHL J1745.7-2900 and 3FGL J1745.6-2859c Fermi sources, given the pronounced peak-like structure exhibited by the IC emission. If the HE and VHE emissions are driven by the same mechanism, a PWN scenario is likely excluded.

Sagittarius A*

Sgr A* has been suggested in a myriad of models to produce relativistic particles that give rise to high-energy γ-rays up to several ten TeV. See, for instance, Ref. [470]. Due to its low bolometric luminosity ($< 10^8$ L_{Edd}), the internal photon-photon pair production is not very effective and Sgr A* is essentially transparent for VHE gamma-rays. VHE gamma rays can be produced from compact regions close to the event horizon of the SMBH in various ways due to acceleration of protons and/or electrons and their interactions with ambient magnetic and radiation fields, as well as with the thermal plasma.

The protons accelerated in the region close to the event horizon of SMBH[1] to energies E$\sim 10^{18}$ eV, start to interact with target field photons of the compact infrared source located at $\sim$10 R_g. Despite the low luminosity of the source, the density of infrared photons appears sufficiently high for reasonably effective photo-pion interactions. Gamma-rays above 1 TeV as well as secondary electrons can effectively interact with the ambient photon and magnetic fields, and thus initiate IC and/or (depending on the strength of the B-field) synchrotron cascades. Gamma-rays produced in this way can explain the observed TeV flux, if the acceleration power of 10^{18} eV protons is about 10^{37} erg s^{-1} [470].

If the magnetic field close to the black hole is not sufficiently high to accelerate protons up to 10^{18} eV, the interaction of protons with the ambient thermal gas is the main source of production of gamma-rays from hadronic origin. Protons can be accelerated to TeV energies through strong shocks developed in the accretion flow. The gamma-ray production efficiency in this case is determined by the ratio of accretion time to the *pp* cooling time.

It has also been suggested that the bright central emission within several arcminutes around Sgr A* has a diffuse origin from runaway protons (see also

[1]The Sgr A* event horizon corresponds to its Schwarzchild radius.

Sec. 4.3.2), peaking towards the direction of the Galactic Centre because of the higher concentration there of both gas and relativistic particles [470] in the inner 10 parsecs. This interpretation would imply an extension of the spectrum of the central source to energies beyond 10 TeV, which however is at odds with the detection of a clear cut-off in the spectrum of HESS J1745-290 at about 10 TeV. Run-away protons can still be compatible with the cut-off in the spectrum of the central source which could be due to the absorption of gamma rays from interactions with the ambient infrared radiation field.

An unresolved millisecond pulsar population

The central stellar cluster is located in the inner 15 pc region of the GC. This massive stellar cluster may have formed by the merging of globular clusters. These globular clusters may harbor a large number of millisecond pulsars (MSPs). MSPs in globular clusters can accelerate electrons up to several ten TeV in the pulsar winds [471]. Given the dense interstellar radiation field with the central parsec [472] and more recently highlighted in Ref. [473], gamma-rays are expected through Inverse Compton scattering of the energetic electrons off the radiation field. The maximum energy that electrons can achieve is here not limited by the losses, even for very dense ISRF or high magnetic field, but is restricted by the physical parameters of the MSPs, *i.e.* by the Larmor radius of the electrons accelerated in the shock of the pulsar wind.

A population of MSPs has been recently advocated to account for the GeV Galactic Center excess seen in Fermi-LAT data, see, for instance, Ref. [474, 475]. In this case, the MSP scenarii may be able to reconnect the GeV and TeV emission in the central 0.1° of the GC.

A spike of dark matter

It has been argued that the source HESS J1745-290 can be explained in terms of gamma-rays issued by 10 TeV-ish DM particles annihilating into a combination of $b\bar{b}$ and $\tau^+\tau^-$ channels [476], see also Ref. [477]. However, it required a significant overall boost of the dark matter signals that can be accommodated by the contraction of the DM density around the SMBH Sgr A*, which results in what is called a dark matter spike. It can arise from the adiabatic growth of the black hole due to the scattering of DM particles with the dense stellar environment of the black hole, or from baryonic infall, as discussed in Sec. 2.2.3. These mechanisms can provide a DM annihilation signal enhancement by a factor of 100 to 1000 [478].

In case of DM annihilations, apart from the smoking-gun signature in the gamma-ray spectrum in the form of lines at the DM mass, a powerful, and maybe

more realistic, one is the presence of distinct features close to the DM mass called cutoff [479] or box-shaped [480, 481] spectral features. Recently, it has been shown that gamma-ray spectra arising from annihilations into hard channels can be better parametrized via super exponential cutoff power law functions rather than simple exponential cutoff power law functions [482], thus providing further discrimination against standard astrophysical emissions. However, the present accuracy of H.E.S.S. measurements at the energy end of the spectrum of HESS J1745-290 is not sufficient so far to significantly distinguish a exponential cutoff power law behaviour from a super exponential cutoff power law one [311].

4.2.3 Forecast observation of HESS J1745-290 with CTA

While the H.E.S.S. observations of the GC successfully revealed an energy cut-off around 10 TeV in the spectrum of HESS J1745-290, the currently-available statistics, present energy resolution and systematics uncertainties of spectral reconstruction are not sufficient to further investigate the spectral shape in the 10 TeV energy regime. Given that a super exponential cut-off in the energy spectrum of HESS J1745-290 may be hints for new physics, future observations of the GC region by CTA could provide new insights in the nature of the source.

Given the improved performances of the CTA observatory with respect to current IACTs, higher sensitivity together with improved energy resolutions of CTA could precisely distinguish between exponential and super-exponential models of emission [483]. The left panel of Fig. 4.3 shows the χ^2 of the fit of the exponential template and super-exponential template to mock data generated with the super-exponential template using the instrument response functions for the Southern site of CTA [484]. About 10 hours of observations would be able to distinguish between the two templates. The right panel of Fig.4.3 the best-fit value of the β parameter for the exponential and super-exponential templates, respectively. Estimates of β converge in $\sim$10 hours to their respective values. For further details about the generation of the mock spectral data and analysis procedure, see Ref. [483].

Provided that CTA is able to control the systematic uncertainty to a level much better than H.E.S.S., the observations by CTA of H.E.S.S. J1745-290 should help to discriminate a conventional astrophysical emission from a dark matter origin.

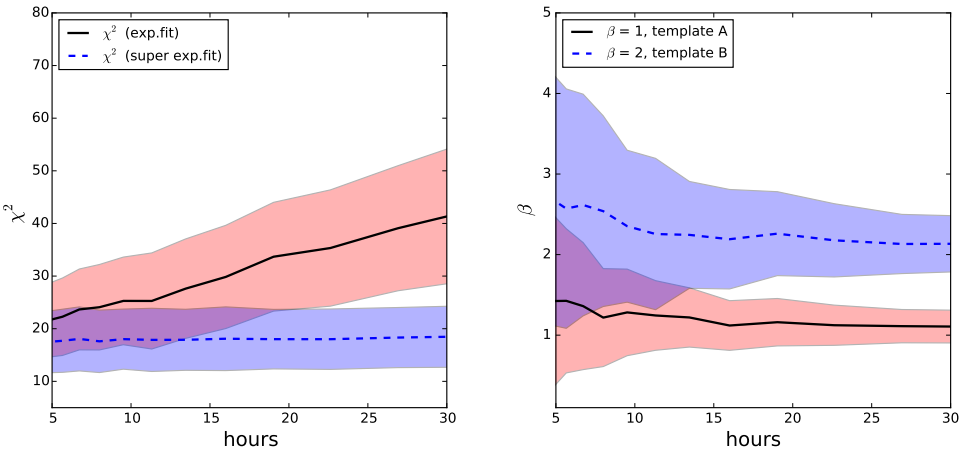

Figure 4.3: *H.E.S.S. J1745-290 seen with CTA.* ***Left panel :*** *χ^2 of the fit of the exponential template (blue dashed line) and super-exponential template (black solid line) to mock data generated with the super-exponential template. The red and the blue shaded regions denote one standard deviation regions for the exponential and the super-exponential fits.* ***Right panel :*** *Values of the energy power-law exponent β of the super-exponential fits to mock data generated with the exponential template (black solid line) and with the super-exponential template (blue dashed line). The red and the blue shaded regions denote one standard deviation regions for the fits to template A and template B correspondingly. Figures extracted from Ref. [483].*

4.3 Diffuse TeV emission

4.3.1 The Central Molecular Zone in VHE gamma rays

The detection of VHE diffuse emission in 2006 by H.E.S.S. revealed the presence of an extended emission along the Galactic plane in the central 300 pc of the GC. The spatial correlation of the TeV emission with the giant molecular clouds of the CMZ first hinted for hadronic acceleration of hadronic cosmic rays in this region [295]. The large photon statistics accumulated over the last 10 years of observations together with improvements in the methods of data analysis, enabled recently a refined study of the spectral and spatial properties of the diffuse emission of the central molecular zone. In Fig. 4.4, the VHE gamma-ray map of the CMZ shows a strong, though not linear, correlation between the brightness distribution of gamma rays and the locations of massive gas-rich cloud complexes. This points towards a hadronic origin of the diffuse emission, where the gamma rays come from decays of π_0 produced in the interactions of relativistic protons with the ambient gas. The morphology of the CMZ seen in gamma rays is both determined by the location and the particle injection rate history of the cosmic-

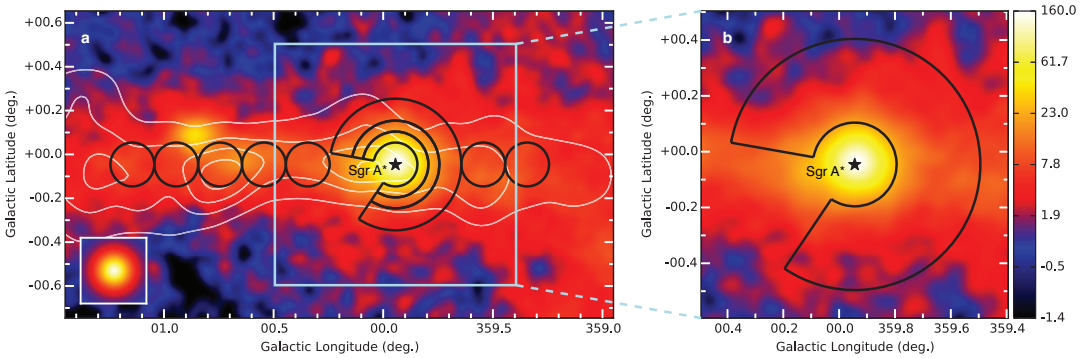

Figure 4.4: *VHE gamma-ray image of the Galactic Centre region. The color scale indicates counts per $0.02° \times 0.02°$ size pixel.* ***Left panel:*** *The black lines outline the regions used to calculate the cosmic-ray energy density throughout the central molecular zone. A section of 66° is excluded from the annuli to avoid contamination from a newly detected source. White contour lines indicate the density distribution of molecular gas, as traced by its CS line emission. The location of Sgr A* is given by the black star. The inset shows the simulation of a point-like source.* ***Right panel:*** *Zoomed view of the inner ∼70 pc and the contour of the region used to extract the spectrum of the diffuse emission. Figure extracted from Ref. [296].*

ray accelerator(s) responsible for the ultra-relativistic protons, and by the gas density distribution. The more detailed and accurate spatial morphology seen now in gamma rays is a unique proxy to probe the cosmic-ray distribution at the heart of our Galaxy.

Cosmic-ray distribution measurement

The derivation of the cosmic-ray density profile in the central molecular zone relies on the distribution of target material (for cosmic-ray interactions). The bulk of the gas in the Galactic Centre region is in the form of the molecular hydrogen H_2, for which mass estimates are based on indirect measurements using tracer molecules. They are typically rare relative to H_2 but much easier to detect and with an approximately known ratio to H_2. Among them are the CS, $^{12}C^{16}O$ and HCN molecules with line emission from transitions that can be detected. The total mass in the inner 150 pc of the central molecular zone is estimated to be $3^{+2}_{-1} \times 10^7$ $M_\odot$ [485, 486]. The regions shown in the left panel of Fig. 4.4 cover almost completely the inner 150 pc of the central molecular zone and are used to extract the radial distribution of cosmic rays. If the gamma-ray emission is completely due to the decay of neutral pions produced in proton-proton interactions, the gamma-ray luminosity L_γ above energy E_γ is related to the total energy of cosmic-ray protons W_p as $L_\gamma(\geq E_\gamma) \simeq \eta_N W_p(\geq 10\,E_\gamma)/t_{pp\to\pi_0}$, where $t_{pp\to\pi_0} =$

1.6×10^8 yr $(1\ \mathrm{cm}^{-3}/\mathrm{n_H})$ [487] is the proton energy loss timescale due to neutral pion production in an environment of hydrogen gas of density n_H, and $\eta_N \simeq 1.5$ accounts for the presence of nuclei heavier than hydrogen in both cosmic rays and interstellar matter. Given the target mass measurements, the energy density of cosmic rays, w_{CR}, averaged along the line of sight can be obtained.

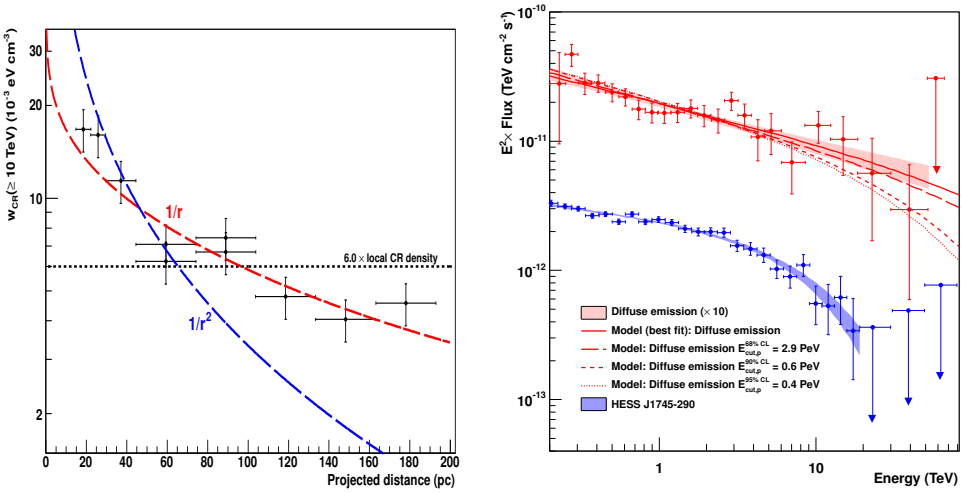

Figure 4.5: *Cosmic-ray distribution and energy fluxes in the Galactic Centre.* ***Left panel:*** *Spatial distribution of the cosmic-ray density versus projected distance from Sgr A*. The vertical and horizontal error bars show the 1σ statistical plus systematic errors and the bin size, respectively. Constant, $1/r$ and $1/r^2$ fits to the measurement of the cosmic-ray density radial profile integrated along the line of sight are shown.* ***Right panel:*** *Spectra of the diffuse emission and HESS J1745-290. The vertical and horizontal error bars show the 1σ statistical error and the bin size, respectively. Arrows represent 2σ flux upper limits. The 1σ confidence bands of the best-fit spectra of the diffuse and HESS J1745-290 are shown in red and blue shaded areas, respectively. The red lines show the numerical computations assuming that gamma rays result from the decay of neutral pions produced by pp interactions. Figures extracted from Ref. [296].*

Figure 4.5 shows the radial profile of the E≥10 TeV cosmic-ray energy density w_{CR} up to r≈200 pc for a Galactic Centre distance of 8.5 kpc, determined from the gamma-ray luminosity and the amount of target gas. This high energy density in the central molecular zone is found to be an order of magnitude larger than that of the "sea" of cosmic rays that universally fills the Galaxy, while the energy density of low energy (GeV) cosmic rays in this region has a level comparable to it. This requires the presence of one or more accelerators of multi-TeV particles operating in the central molecular zone.

If the accelerator injects protons at a continuous rate, $\dot{Q}_{\rm p}(E)$, the radial distribution of cosmic rays in the central molecular zone, in the case of diffusive propagation, is described as $w_{\rm CR}(E,r,t) = \dot{Q}_{\rm p}(E)/(4\pi D(E)r) \times {\rm erfc}(r/r_{\rm diff})$ [488], where $\dot{Q}_{\rm p}(E)$, $D(E)$ and $r_{\rm diff}$ are the proton injection rate, the diffusion coefficient, and the diffusion radius, respectively. For timescales t smaller than the proton-proton interaction time ($t_{pp} \simeq 5 \times 10^4 (n_{\rm H}/10^3 cm^{-3})^{-1}$ yr), the diffusion radius is $r_{\rm diff} \simeq \sqrt{4D(E)t}$. Thus, at distances $r < r_{\rm diff}$, the proton flux should decrease as $\sim 1/r$ provided that the diffusion coefficient does not have a strong spatial dependency in the central molecular zone. The measurements of the CR density shown in the left panel of Fig. 4.5 clearly support the $1/r$ dependence over the entire central molecular zone region. The $1/r^2$ and constant profiles, the former being expected if cosmic rays are advected in a wind, and the latter in the case of a single burst-like event of cosmic-ray injection, are significantly disfavored.

The CR radial profile shown in the left panel of Fig. 4.5 points towards an accelerator located in the inner 10 pc of the GC. The $1/r$ profile of the CR density up to 200 pc indicates a quasi-continuous injection of protons into the central molecular zone from a centrally located accelerator on a timescale Δt exceeding the characteristic time of diffusive escape of particles from the central molecular zone, that is, $\Delta {\rm t} \geq {\rm t_{diff}} \approx {\rm R}^2/6{\rm D} \approx 2 \times 10^3 ({\rm D}/10^{30} {\rm cm}^2 {\rm s}^{-1})^{-1}$ yr, where D is normalized to the characteristic value of multi-TeV cosmic rays in the Galactic disk. The average injection rate of particles is found to be $\dot{Q}_p(\geq 10\,{\rm TeV}) \approx 4 \times 10^{37} (D/10^{30})$ erg s^{-1}. The diffusion coefficient itself depends on the power spectrum of the turbulent magnetic field, which is unknown in the central molecular zone region. This introduces an uncertainty in the estimates of the injection power of relativistic protons. Yet, the diffusive nature of the propagation is constrained by the condition $R^2/6D \gg R/c$. For a radius of the central molecular zone region of 200 pc, this implies $D \ll 3 \times 10^{30}$ cm^{2}s^{-1}, and, consequently, $\dot{Q}_p \ll 1.2 \times 10^{38}$ erg s^{-1}.

The integration of the CR radial distribution over the timescale Δt given in the left panel of Fig. 4.5 yields the total energy $W_{\rm p}$ of E$\geq$10 TeV protons confined in the central molecular zone: $W_p \approx 1.0 \times 10^{49}$ erg. The supermassive black hole Sgr A* at the Galactic Centre is the most plausible supplier of ultra-relativistic protons and nuclei; these particles could have been accelerated either in the accretion flow (*i.e.* in the immediate vicinity of the black hole) or somewhat further away - for example, at the site of termination of an outflow. If Sgr A* is indeed the particles' source, the required acceleration rate of about 10^{37} - 10^{38} erg s^{-1} would exceed by two-to-three orders of magnitude the current bolometric luminosity of this object, and would constitute at least 1% of the current power produced by accretion onto the supermassive black hole. Given that the current

accretion rate is relatively modest, and that at certain epochs this supermassive black hole could have operated at a much higher accretion rate[1], this higher rate could also facilitate greater cosmic-ray production rates. An average acceleration rate of 10^{39} ergs^{-1} of E$\geq$10 TeV protons over the last 10^6-10^7 years would be sufficient to explain the flux of cosmic rays around the energy spectrum feature - the so-called *knee* - at 1 PeV. If this explanation is correct, it could be a solution to one of the most controversial and actively debated problems of the paradigm of the SNR origin of Galactic cosmic rays.

4.3.2 Discovery of the first Galactic PeVatron

With the available H.E.S.S.-I photon statistics, the energy spectrum of the diffuse γ-ray emission has been extracted from an annulus centered at Sgr A* as shown on the right panel of Fig. 4.4). The best fit to the data is found for a spectrum following a power law extending with a photon index of $\sim$2.3 to energies up to tens of TeV, without a cut-off or a break as shown in the right panel of Fig. 4.5. This is the first time that such a gamma-ray spectrum, arising from hadronic interactions, has been detected. Since these gamma rays result from the decay of neutral pions produced by *pp* interactions, the derivation of such a hard power-law spectrum implies that the spectrum of the parent protons should extend to energies close to 1 PeV. The best fit of a gamma-ray spectrum from neutral pion decay to the H.E.S.S. data is found for a proton spectrum following a pure power law with an index of $\sim$2.4. Assuming a cut-off in the parent proton spectrum, the corresponding secondary gamma-ray spectrum deviates from the HESS data at 68%, 90% and 95% confidence levels for cut-offs at 2.9 PeV, 0.6 PeV and 0.4 PeV, respectively.

This is the first robust detection of a VHE cosmic hadronic accelerator which operates as a source of PeV particles in the Galaxy, i.e. a PeVatron.

pp interactions of PeV protons could also be studied by the observation of emitted neutrinos or X-rays from the synchrotron emission of secondary electrons and positrons (see Methods and Extended Data Figs. 3 and 4 of Ref. [296]). However, the measured gamma-ray flux puts the expected fluxes of neutrinos and X-rays below or at best close to the sensitivities of the current instruments, but may be accessible for future instruments like a km^3 neutrino telescope located in the Northern hemisphere [491].

[1]Sagittarius A* went through active phases in the past, as demonstrated by X-ray outbursts [489] and an outflow from the Galactic Centre [490].

Connecting HESS J1745-290 and the TeV diffuse emission

The Galactic Centre PeVatron appears to be located in the same region as the central gamma-ray source HESS J1745-290. Unfortunately, the current data cannot provide an answer as to whether there is an intrinsic link between these two objects. The point-like source HESS J1745-290 itself remains unidentified. Moreover, it has also been suggested that this source might have a diffuse origin, peaking towards the direction of the Galactic Centre because of the higher concentration there of both gas and relativistic particles. In fact, this interpretation would imply an extension of the spectrum of the central source to energies beyond 10 TeV, which however is at odds with the detection of a clear cut-off in the spectrum of HESS J1745-290 at about 10 TeV. Yet the attractive idea of explaining the entire gamma-ray emission from the Galactic Centre by run-away protons from the same centrally located accelerator can still be compatible with the cut-off in the spectrum of the central source. For example, the cut-off could be due to the absorption of gamma-rays caused by interactions with the ambient infrared radiation field.

4.3.3 Alternative sources of PeV cosmic rays ?

Any scenario that attempts to explain the H.E.S.S. observations of the central molecular zone should satisfy the following conditions: *(i)* the accelerator has to be located in the inner 10 pc of the Galaxy, *(ii)* the accelerator(s) has (have) to be continuous over a timescale of at least thousands of years, and *(iii)* the acceleration has to proceed up to PeV energies. Besides the supermassive black hole Sgr A*, alternative sources of the cosmic rays responsible for the CMZ gamma-ray emission include SNRs, stellar clusters, and radio filaments.

A single supernova remnant

A single supernova remnant would suffice to provide the rather modest energy in cosmic rays. A possible candidate could be Sgr A East. Although this object has already been excluded as a counterpart of HESS J1745-290 [468], the multi-TeV protons accelerated by this object and then injected into the central molecular zone could contribute to the diffuse gamma-ray component. Particle acceleration in SNRs is widely believed to proceed through diffusive shock acceleration, where the acceleration timescale is inversely proportional to the shock speed squared. Due to the high shock speeds and large magnetic field strength that can be reached in the early free expansion phase of the SNR evolution, protons can be accelerated up to PeV energies. However, Ref. [492] shows that the duration of this phase is of the order of tens of years. Thus, even though

SNRs can potentially provide PeV particles, they cannot likely act as continuous injectors of such energetic particles for a time of the order of thousands of years.

Stellar clusters

Compact stellar clusters are other potential sites of the acceleration of protons in the Galactic Centre. Three are known in the inner 0.1°-0.2° region: the central, the Arches, and the Quintuplet cluster. The mechanical power in these clusters in the form of stellar winds, which can provide adequate conditions for particle acceleration, is sufficient to explain the required total energy of cosmic rays in the central molecular zone. The most likely sites for acceleration of particles in stellar clusters are the stellar winds of the massive OB stars that form the cluster, and the shocks of the supernovae which mark the end of the life of these stars. Thus, the mechanism of operation of PeVatrons in stellar clusters is reduced to the presence of supernova shocks. However, the acceleration of protons to PeV energies requires bulk motions in excess of 10,000 kms^{-1} which could only exist in the stellar clusters because of very young supernova shocks. Thus SNR shocks following the explosion of cluster member stars remain the best candidates as particle accelerators.

Both the Arches and the Quintuplet clusters are located outside the inner 10 pc region, and this disfavors their role as accelerators of the cosmic rays responsible for the diffuse gamma-ray emission. On the contrary, the central cluster is located well within the central 10 pc region, and thus should be considered as a potential candidate for the acceleration of cosmic rays in the central molecular zone.

Since the acceleration of PeV particles by shocks, either in individual SNRs or in stellar clusters, cannot last much longer than 100 years [493], we would need more than 10 supernova events to meet the requirement of continuous injection of cosmic rays in the central molecular zone over 10^3 years. Given the very small size of the region ($\sim$0.4 pc), such a large supernova explosion rate is unrealistic.

Radio filaments

It has been proposed in Ref. [494] that the diffuse gamma-ray emission from the central molecular zone was the result of non-thermal Bremsstrahlung from relativistic electrons. In this scenario, the putative sources of gamma-ray emitting electrons are the elongated radio filaments detected throughout the central molecular zone region. This is in tension with the location of the source of cosmic rays is in the inner 10 pc of the Galaxy.

Though the acceleration mechanism is not discussed in Ref. [494], filaments are assumed to somehow accelerate electrons and then release them in the inter-

stellar medium. In order to fill the whole central molecular zone region before being cooled by synchrotron and inverse Compton losses, electrons are assumed to propagate ballistically, *i.e.* at the speed of light without a significant deflection in the magnetic field. This unconventional assumption is made at the expenses of a very large energy requirement: observations can be explained if the energy injection rate of cosmic-ray electrons in the central molecular zone is of the order of 10^{41} erg s^{-1}. This is a very large injection rate, being comparable to the total luminosity of cosmic-ray protons in the whole Galaxy, and makes this scenario problematic.

A leptonic origin for the multi-TeV gamma-rays ?

Two prime radiation mechanisms are related to interactions of ultrarelativistic protons and electrons, with the dense gas in the central molecular zone and with the ambient infrared radiation fields, respectively. To explain multi-TeV gamma rays, the maximum energy of protons and electrons need to be as large as ∼1 PeV and ∼100 TeV, respectively. In addition, these particles should effectively propagate and fill the entire central molecular zone. Whereas in the case of the hadronic scenario one needs to postulate an existence of a PeVatron in the Galactic Centre, any *leptonic* model of gamma-ray production should address the following questions: *(i)* whether the accelerator could be sufficiently effective to boost the energy of electrons up to $\geq$ 100 TeV under the severe radiative losses in the Galactic Centre; *(ii)* whether these electrons can escape the sites of their production and propagate over distances of tens of parsecs; and *(iii)* whether they can explain the observed hard spectrum of multi-TeV gamma rays.

Acceleration of electrons to multi-100 TeV energies is more difficult than acceleration of protons because of severe synchrotron and inverse Compton (IC) losses. Acceleration of electrons to energies beyond 100 TeV is possible in the so-called extreme accelerators, where the acceleration proceeds at the maximum possible rate allowed by classical electrodynamics, $tacc \simeq R_{\rm L}/c \approx 0.4(E/100TeV)(B/\mu G^{-}1{\rm yr}$. Even so, the escape of such energetic electrons from the accelerator, and their propagation far enough (tens of parsecs) to fill the central molecular zone, can be realized only for rather unrealistically weak magnetic fields and fast diffusion. Indeed, the propagation time over a distance R (in pc) and for a particle diffusion coefficient D is equal to $t_{\rm diff} = R^2/6D \approx 2 \times 10^3 (R/200{\rm pc})^2 (D/10^{30}{\rm cm}^2{\rm s}^{-1}) yr$ and, for typical interstellar conditions, is much longer than the synchrotron loss time of electrons with energy E_e, $t_{\rm syn} \approx 10(B/100\mu G)^{-2}(E_e/100TeV)^{-1}$ yr.

The efficiency of a given gamma-ray emitting process is determined by the cooling time of particles through that specific channel compared to the characteristic times of other (radiative and non-radiative) processes. The bremsstrahlung and IC scattering result in gamma-ray emission while the ionization and syn-

chrotron losses reduce the efficiency of gamma-ray production. Bremsstrahlung is an effective mechanism of gamma radiation at GeV energies. Above 100 GeV, IC cooling becomes more effective and strongly dominates over bremsstrahlung at energies above 10 TeV in the Central Molecular Zone.

At low energies, the losses due to the diffusive escape of electrons from the central molecular zone are more important. Although it has been shown that the magnetic field in the Galactic Centre should have a lower limit of B = 50 μG on 400 pc scale, even with a B = 15 μG magnetic field, the calculations above 10 TeV do not match the observed fluxes. If we assume, say, gas density higher by an order of magnitude, then bremsstrahlung would dominate over the IC contribution, and the flux of gamma rays could be increased. However, for any reasonable magnetic field, the synchrotron losses above 10 TeV will dominate over bremsstrahlung. This will make the steady-state electron spectrum steeper with power-law index $\alpha = \alpha_0 + 1$ (α_0 is the power-law index of the electron injection spectrum). Since the gamma-ray spectrum produced owing to bremsstrahlung mimics the energy spectrum of parent electrons ($\Gamma = \alpha$), at energies of gamma-rays above a few TeV we should expect quite a steep spectrum of gamma-rays, with a power-law index $\Gamma > 3.4$, which is in apparent conflict with observations.

4.3.4 The Galactic Center excess and TeV diffuse emission

The Galactic Center hosts numerous sources that produce diffuse gamma-ray emission in the GeV energy range. Recently, a high-energy gamma-ray excess has been detected by Fermi-LAT with a spatial extension up to about 20° from the Galactic Center, known as *the Galactic Centre excess*. See, for instance, Refs. [495, 496, 497, 498, 499]. Several emission scenarii have been suggested. Among the most widely discussed are dark matter annihilations in the inner region of the Galactic dark matter halo [495, 497, 498, 499], as well as outflows from the supermassive black hole Sagittarius A* injecting energetic cosmic-ray protons [500] or leptons [501, 502] in the interstellar medium. The dark matter scenario may be in tension with the non-observation of gamma-ray excesses towards dwarf galaxy satellites of the Milky Way. The Sagittarius A* scenario would hardly reproduce the morphology of the Galactic Center excess. More recently, a hypothetical population of MSP in the Galactic bulge has been shown to well reproduce the morphology of the Galactic Center excess [503, 504, 505, 474][1].

[1]The unresolved bulge MSP population is robustly detected against the underlying interstellar emission models possibly including the Fermi bubble component [474]. However, there is no observational hint of detection about the existence of such a population.

Leptonic emission from millisecond pulsars and dark matter spike

An alternative leptonic interpretation of the H.E.S.S. diffuse emission detected in the inner 50 pc to the excess of GeV gamma-rays at the GC has been attempted in Ref. [506] from millisecond pulsars (MSPs) [507, 508, 509, 510, 511, 512, 513, 514, 505, 515] advocated to explain the *GeV Galactic Center excess* reported from Fermi-LAT data [495, 516, 517, 518, 507, 519, 508, 520, 521, 522]. A leptonic model of the TeV diffuse emission could evade the constraints discussed in Ref. [296], in particular, for the hardness of the observed spectrum, and the propagation set-up to enable electrons to diffuse out to sufficiently large distances. Compared to Ref. [296], a smaller magnetic field strength of 10 μG compared to 0.1 mG and a slightly larger diffusion coefficient at the highest energies can be considered.

The interaction of the high-energy electron wind of MSPs may create a shock with the interstellar medium which can accelerate electrons to VHE, potentially up to 100 TeV [471]. The maximum electron energy is limited by their ability to escape the shock region, and by their synchrotron losses. VHE gamma rays are produced by the inverse Compton process of electrons scattering off the interstellar radiation field. It has been claimed in Refs. [471, 523] that IC emission from MSPs could be responsible for the H.E.S.S. central source data,

Assuming the spatial distribution of MSPs fixed by the GeV Galactic Centre excess data, the normalization of the electron injection spectrum[1] can be obtained by fitting the spectrum of the H.E.S.S. diffuse emission. The electron spectrum from MSPs after propagation can be computed in a steady state and accounting for energy losses and spatial diffusion. See Ref. [506] for further modelling on the propagation and predicted gamma-ray emission.

The left panel of Fig. 4.6 shows the predicted gamma-ray fluxes from the MSP-induced IC emission model for maximum electron energies of 50 TeV. The best-fit model corresponds to a fraction $f_e^{\pm} \approx 0.1$. Such emissions from the so far undetected MSPs could account for the H.E.S.S. diffuse emission up $\sim$10 TeV. However, even for an energy cut-off at 100 TeV, the MSP-induced IC emission fails to reproduce the high energy part of the spectrum beyond 10 TeV. This is due to synchrotron emission taking over IC emission above $\sim$10 TeV, inducing a softening in the gamma-ray spectrum. Therefore, an additional hard component is needed, and this provides the motivation for considering a contribution from multi-TeV annihilating DM.

[1]The fraction of spin-down power released by pulsars, $f_e^{\pm}$, in the electron wind is taken to 0.1, which is motivated since it actually corresponds to an electron wind power equal to the luminosity of the direct pulsar gamma-ray emission that can account for the GeV excess. We also note that a higher value of this fraction would overshoot the low energy part of the H.E.S.S. diffuse emission.

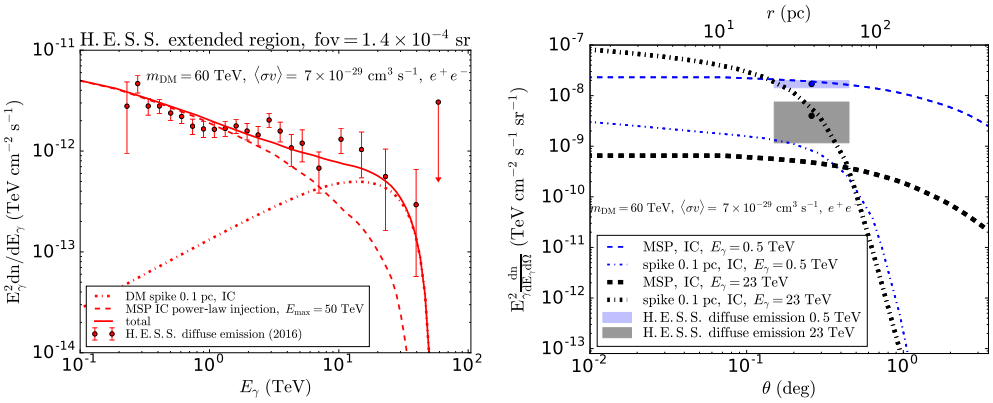

Figure 4.6: *VHE emission from a combination of millisecond pulsars and dark matter spike.* ***Left panel:*** *Spectra from 100 GeV to 100 TeV for the H.E.S.S. diffuse emission. IC emission from MSPs is depicted as a dashed line. IC emission from a spike of radius 0.1 pc, for a 60 TeV DM candidate annihilating exclusively to e^+e^- with a cross section of $\langle\sigma c\rangle = 7 \times 10^{-29}$ $cm^3 s^{-1}$ is shown as a dot-dashed line. The solid line represents the total spectrum.* ***Right panel:*** *IC emission intensity from MSPs (dashed) and a 0.1 pc DM spike (dot-dashed) as a function of angular distance from the GC, at 0.5 TeV (thin blue) and 23 TeV (thick black). The data points at these energies and their statistical error bars are depicted as shaded rectangles. Figures extracted from Ref. [506].*

Given that the DM candidate must feature an annihilation cross section smaller than $\sim 10^{-25}$ cm^{3}s^{-1} at TeV masses to avoid tensions with recent H.E.S.S. constraints, and that the dark matter density must be high enough in the GC region to produce a sufficiently high gamma-ray flux, a standard NFW profile cannot account for the observed emission. A supermassive BH-induced spike can be assumed in the inner part of the DM density profile. The existence of a spike is actually debated [524, 525][1]

The gamma-ray contribution from a DM spike of radius 0.1 pc[2] for a DM candidate of mass $m_{\rm DM} = 60$ TeV, annihilating to e^+e^- with a sub-thermal best-fit cross section of $\langle\sigma v\rangle = 7 \times 10^{-29}$ cm^3 s^{-1} is shown in the left panel of Fig. 4.6. The H.E.S.S. diffuse emission can be accounted for by the sum of the IC emission from MSPs and a DM spike, with the lower part of the H.E.S.S. spectrum associated with MSPs, and the high energy part above $\sim$ 10 TeV with DM. This model is compatible with the observed emission from the central source

[1]Moreover, there is compelling evidence for a unique major merger involving the Milky Way about 12 billion years ago that led to the formation of the bulge [526], which would not have affected the survival of a spike.

[2]This corresponding roughly to the size of the gravitational sphere of influence of the central black hole.

HESS J1745-290, in particular with the upper limits at the highest energies [506].

The right panel of Fig. 4.6 are the IC intensities $E_\gamma^2 \mathrm{d}n/(\mathrm{d}E_\gamma \mathrm{d}\Omega)$ at 0.5 TeV (thin blue lines) and 23 TeV (thick black lines), as a function of angle θ (or radius r) from the Galactic Centre, for the Inverse Compton MSP and DM spike components. For the DM spike, which dominates above ~ 10 TeV, the IC intensity drops steeply around 0.3° at 23 TeV and around 1° at 0.5 TeV. These specific scales correspond to the diffusion lengths associated with the losses and diffusion coefficient. For the MSP component, dominant below ~ 10 TeV, the spatial extension of the IC emission is of order a few degrees, therefore larger than the H.E.S.S. region.

The diffuse emission has been detected by H.E.S.S. by accumulating statistics from a significant exposure time in this region. However, the emission might be even more extended, and future H.E.S.S. observations at Galactic latitudes $|b| > 1$ deg may help to discriminate between the proposed scenarii. In particular, according to our predictions, H.E.S.S. should observe an even more extended signal below ~ 10 TeV, due to the MSP component.

One should note that the IC DM spike induced flux is sensitive to the losses and diffusion coefficient in the central pc. A magnetic field larger than 10 μG, for instance a 0.1 mG field [473, 527, 528] or a 1 mG field [529], would lead to a significant increase in synchrotron losses, thus significantly reducing the IC flux and spoiling the achievement of explaining the high-energy part of the H.E.S.S. diffuse emission. With a 10 μG magnetic field, using a milder energy dependence of the diffusion coefficient would only imply a higher normalization of the diffusion coefficient for electrons of a few 10 TeV to diffuse out to the region of interest. However, if the diffusion coefficient was in fact much smaller, typically for Bohm diffusion [471], the spike-induced IC emission would be confined within the region corresponding to the central source and there would be no leakage into the diffuse emission region. Regarding the DM profile, for values of the spike radius larger than ~ 0.1 pc, the associated IC flux significantly overshoots both the diffuse and point source data, unless the annihilation cross section is further reduced. The model depends strongly on the DM annihilation channel, and require dominant annihilation into e^+e^-. For softer channels like $\mu^+\mu^-$, $\tau^+\tau^-$ or $b\bar{b}$, the IC flux is too small in the H.E.S.S. extended region of interest while the associated emission in the central 0.1° overshoots the flux from the central source HESS J1745-290. For a 10 μG magnetic field, the synchrotron flux for this model is actually several orders of magnitude below the steady diffuse X-ray emission measured with the NuSTAR satellite within a few pc of Sgr A*, in the 20–40 keV band [530, 531].

Hadronic emission from an unresolved bulge population of millisecond pulsars ?

An unresolved MSP population has been strongly advocated to explain the Galactic Center excess, through a leptonic channel [474]. At higher energies, the H.E.S.S. observations are interpreted as a convincing proof that protons are accelerated up to PeV energies. Assuming that the MSP emission is loaded in baryons, and thus possible PeV proton accelerators, the MSP population could also be responsible of the H.E.S.S. diffuse TeV emission.

In addition to the Galactic disk pulsar population, a distinct bulge pulsar population is needed, for radial distance lower than 3 kpc from the Galactic Center. A bulge-like population can be explained in scenarios where MSP are first formed in globular clusters and subsequently infall in the Galactic Center region [532, 533, 534][1].

Assuming the MSP population characterized by a spatial distribution around the Galactic Center, and by period, magnetic field and age distributions, MSP accelerate protons up to very high energies, that can reach PeV energies for initial spin periods of 1 ms and dipole magnetic fields of 10^9 G [535]. The gamma-ray flux profile as a function of distance from the Galactic Center and the inferred cosmic-ray density, as well as the TeV gamma-ray flux energy spectrum in the inner 50 pc region can be inferred by a population of MSPs with free parameters limited to the magnetic field distribution, the acceleration efficiency and the number of MSP in the population considered. See Ref. [535] for details on the emission modelling. Figure 4.7 shows the gamma-ray spectrum and a luminosity profile in the transient monoenergetic cosmic-ray injection [535] that are in agreement with the H.E.S.S. measurements considering the bulge MSP contribution only, a moderate acceleration efficiency $\eta_{\rm acc} \sim 0.03$, a total number of pulsars $\eta_{\rm p} N_{\rm b} \sim 10^6$, and a power-law distribution of the magnetic field of index -1 between $B_{\rm min} = 10^8$ G and $B_{\rm max} = 10^{11}$ G. In the case of a transient cosmic-ray injection, the number of MSPs $N_{\rm b}(L_{\rm CR}(t_{\rm sd}) > 10^{33}{\rm ergs}^{-1}) \simeq 7 \times 10^4$. The MSP number with $L_{\rm CR}(t_{\rm sd}) > 10^{34}{\rm ergs}^{-1}$ is of the same order than the one derived in Ref. [536]. A total population of $\eta_{\rm p} 10^6$ MSP, accelerating protons up to very high energies with baryon loading $\eta_{\rm p}$, appears as an acceptable candidate to explain the TeV diffuse emission.

The modelling of the MSP population is subject to uncertainties. The dipole magnetic field distribution of such objects is still not well constrained by the observations. Note that this distribution has a strong impact on the predictions, especially on the shape of the gamma-ray spectrum. While the maximum value of the magnetic field has a minor impact as long as higher than 10^{11} G, the index -1 of its power-law distribution is decisive in order to match the H.E.S.S. measure-

[1] 3000 MSPs are predicted in Ref. [534] in the inner 100 pc of the Galaxy.

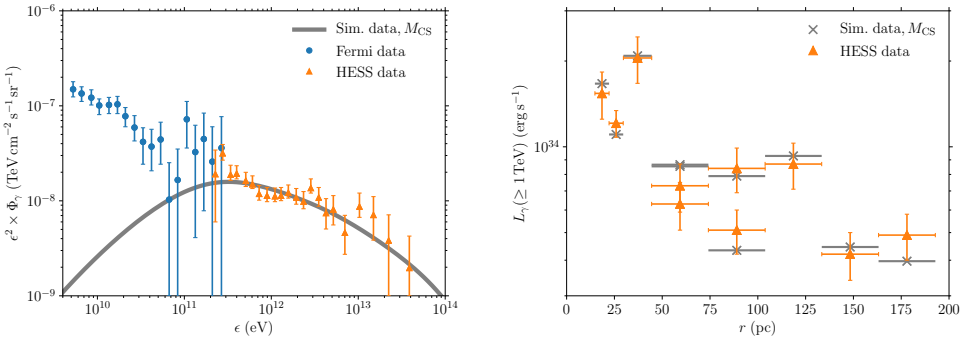

Figure 4.7: *Left panel: Diffuse gamma-ray spectrum predicted by the transient monoenergetic injection model with $\eta = 0.03$ and $\eta_p Nb \simeq 10^6$ (grey line) and measured by Fermi-LAT (blue dots) and H.E.S.S. (orange triangles). Right panel: Gamma-ray luminosity as a function of the distance to the Galactic center for the same model (grey crosses) and measured by H.E.S.S. (orange triangles). Figures extracted from Ref. [535].*

ments. A total number of pulsars in the bulge $\eta_p 10^6$ is required to reproduce the H.E.S.S. measurements. This number depends on the baryon loading η_p which is a poorly constrained quantity, on the acceleration efficiency and on the various distributions characterizing our pulsar population.

Better observational constraints would be required to obtain a more accurate estimate of this quantity. Moreover, N_b should not be compared directly with the number of MSP derived in other MSP population studies, such as [3, 30]. Their number of MSP are frequently given for gamma-ray luminosities in a given range, with gamma rays produced through leptonic processes. From our cosmic- ray luminosity distribution, about 10% of the total MSP population is characterized by $L_{CR}(tsd) > 10^{33}\mathrm{ergs}^{-1}$. A higher value of the cosmic-ray luminosity lower bound $L_{CR}(t_{sd}) > 10^{34}\mathrm{ergs}^{-1}$ lead to an even lower fraction ∼3% of the total MSP population, which gives a number of pulsars in this luminosity interval $N_b(L_{CR}(t_{sd}) > 10^{34}\mathrm{ergs}^{-1} \sim 10^4$ - 10^5, more compatible with the values obtained in [474, 536]. A more detailed treatment would require a comparison between our hadronic model and leptonic scenarii.

Further more precise measurements above 50 TeV with H.E.S.S. and future higher ones with CTA, whether or not indicating the presence of a high energy cut-off in the VHE diffuse emission spectrum, would put strong constraints on several parameters of the discussed model, such as the acceleration efficiency η_{acc} or the magnetic field distribution, in particular on its upper bound B_{max}, the value of B_{min} being already better constrained by observations. A high energy cut-off would be associated with a low η_{acc} or a low B_{max}.

The millisecond pulsar scenario at the Galactic Centre can be appealing to some extend to explain the TeV emission. However, such a population of millisecond pulsars has to be discovered. If it exists, future observations of the Galactic bulge with SKA should have the sensitivity to detect it.

4.4 Perspectives

The Galactic Centre, arguably one of the most studied regions of the sky in nearly every wavelength, is a laboratory for particle astrophysics. In VHE gamma rays, this region has yielded major scientific discoveries. Additional statistics and improved systematic uncertainty understanding may enable to characterize the shape of the gamma-ray energy cut-off of the central emission HESS J1745-290 that may be associated to Sagittarius A* while so far unknown. Future observations with improved energy resolution and sensitivity of CTA will permit to further investigate the spectral shape in the energy cutoff region and disentangle among the models that have been put forth to explain it, possibly unveiling the longtime debated nature of this source. Though another avenue could the search for variability, the null result for short-term (minutes to hours) and long-term (months to years) variability favor continuous acceleration mechanism, the latter one being in addition hampered by a high level of systematic errors from the inhomogeneous quality of data acquired over scale of years. Monitoring of the cut-off position in the energy spectrum over years may also help to measure the activity of the central engine.

The current Inner Galaxy Survey carried out by H.E.S.S. is the first survey of the Galactic Center region in VHE gamma rays. Among the variety of topics that can be presently addressed is the search for VHE emission from the low-latitude emission from the Fermi bubbles. While the underlying scenario to explain the Fermi bubbles is highly debated from GeV measurements, a search at TeV energies as one of the prime goal of the IGS, would help to further characterize it and possibly discriminate among the proposed scenarii. Among them is the search for emission from the hard Fermi bubbles component at low Galactic latitudes extending up to a TeV. Fig. 4.8 shows the spectrum of the Fermi bubbles measured by Fermi-LAT [475]. While the IGS H.E.S.S. observations have the sensitivity to probe the high-energy part of the spectrum, searches for VHE emission will require a multi-template fitting analysis using the spatial and spectral features of the emissions shining in this region together with an accurate determination of the residual background taking into account the complexity of the spatial distribution of the night sky background in this region and using accurate Monte Carlo simulations of the instrument and observation conditions during the data

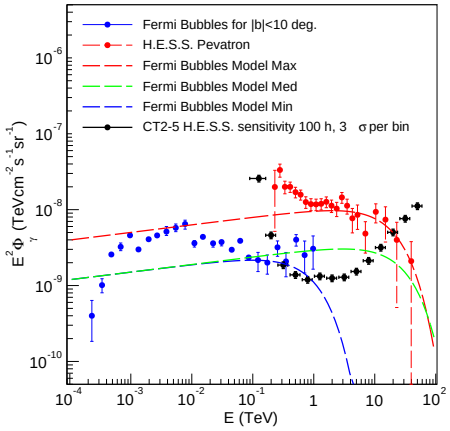

Figure 4.8: *Energy spectrum of the inner part of the Fermi Bubbles emission (blue dots). The black points correspond to H.E.S.S. sensitivity in 100 hours. Min (blue dashed line) and max (red dashed line) models for the low-latitude Fermi Bubble spectrum extrapolated in the TeV energy range are given. The red dots corresponds to GC Pevatron spectrum. The CT2-5 H.E.S.S. sensitivity for 100 h is plotted in black dots. Figure extracted from Ref. [].*

taking. If possible, H.E.S.S. IGS measurements will provide a crucial input to unveil the origin of the Fermi bubbles.

A VHE survey of the Galactic centre in the inner few degrees is crucial to attack the wide variety of targets and topics, for which a large observation time spread over multiple years is required. Although the current level of systematic uncertainties prevents from precise measurements in the ten TeV energy range, studies of the spectral and spatial morphology of the diffuse emission would help to better characterize the injection PeV proton spectrum. However, the realisation of a deep and high-precision survey of the Galactic Centre region is non-trivial. Further studies of the spectral and spatial morphology of the TeV emissions will have to face the complexity and confusion of the gamma-ray emissions, to handle strongly varying background optical light, and the difficulty of modeling the background. In addition, the systematic errors need to be pushed to extremely low levels to produce meaningful limits on the various models. At price of a careful control of the level of systematics which includes an improved background determination through detailed Monte Carlo simulations including the most precise characteristics of the instrument and the observation conditions, the expected higher sensitivity of CTA may make the measurement for a-few-PeV energy cutoff in the proton injection spectrum possible.

Bibliography

[1] P. A. R. Ade et al. *Astron. Astrophys.*, 571:A16, 2014. 5, 20

[2] E. Komatsu et al. *Astrophys. J. Suppl.*, 192:18, 2011. 5

[3] P. A. R. Ade et al. *Astron. Astrophys.*, 571:A17, 2014. 5

[4] Y. Akrami et al. arXiv:1807.06205. 5

[5] J. H. Oort. *Bull. of the Astronom. Institutes of the Netherlands*, 6:249, 1932. 6

[6] F. Zwicky. *Helvetica Physica Acta*, 6:110, 1933. 6

[7] V. C. Rubin and W. K. Ford, Jr. *Astrophys. J.*, 159:379, 1970. 6

[8] D. Clowe et al. *Astrophys. J.*, 648:L109, 2006. 7

[9] A. Burkert. *Astrophys. J.*, 447:L25, 1995. 7, 35

[10] W. J. G. de Blok and A. Bosma. *Astronom. Astrophys.*, 385:816, 2002. 7

[11] W. J. G. de Blok. *Astrophys. J.*, 634:227, 2005. 7

[12] V. C. Rubin, W. K. Ford, Jr., and N. Thonnard. *Astrophys. J.*, 225:L107, 1978. 8

[13] D. P. Clemens. *Astrophys. J.*, 295:422, 1985. 8

[14] P. Mróz et al. *Astrophys. J.*, 870:L10, 2019. 8

[15] J. Dubinski and R. G. Carlberg. *Astrophys. J.*, 378:496, 1991. 7

[16] J. F. Navarro, C. S. Frenk, and S. D. M. White. *Astrophys. J.*, 490:493, 1997. 7, 8, 33, 96

[17] V. Avila-Reese et al. *MNRAS*, 310:527, 1999. 8

[18] J. S. Bullock et al. *MNRAS*, 321:559, 2001. 8, 96

[19] V. Springel et al. *MNRAS*, 391:1685, 2008. 9, 10, 31, 32

[20] J. Diemand et al. *Nature*, 454:735, 2008. 8, 10, 31, 32, 44, 89

[21] J. Stadel et al. *MNRAS*, 398:L21, 2009. 8

[22] G. M. Voit. *Rev. Mod. Phys.*, 77:207, 2005. 8

[23] S. Colafrancesco, S. Profumo, and P. Ullio. *Astron. Astrophys.*, 455:21, 2006. 8

[24] T. Richtler et al. *Astron. Astrophys.*, 478:L23, 2008. 8, 102

[25] Y. Schuberth et al. *Astron. Astrophys.*, 513:A52, 2010. 8, 102, 104

[26] A. El-Zant, I. Shlosman, and Y. Hoffman. *Astrophys. J.*, 560:636, 2001. 9

[27] A. A. Klypin et al. *Astrophys. J.*, 522:82, 1999. 10

[28] B. Moore et al. *Astrophys.J.*, 524:L19, 1999. 10

[29] W. Chiu et al. *Astrophys. J.*, 563:21, 2001. 10

[30] G Kauffmann et al. *MNRAS*, 264:201, 1993. 10

[31] A. Drlica-Wagner et al. *Astrophys. J.*, 813(2):109, 2015. 10

[32] J. S. Bullock, A. V. Kravtsov, and D. H. Weinberg. *Astrophys. J.*, 539:517, 2000. 11

[33] A. J. Benson et al. *MNRAS*, 333:156, 2002. 11

[34] R. S. Somerville. *Astrophys. J.*, 572:L23, 2002. 11

[35] B. Moore. *Nature*, 370:629, 1994. 11

[36] R. A. Flores and J. R. Primack. *Astrophys. J. Lett.*, 427:L1, 1994. 11

[37] J. Diemand et al. *MNRAS*, 364:665, 2005. 11

[38] V. Springel et al. *MNRAS*, 391:1685, 2008. 11

[39] W. J. G. de Blok. *Advances in Astronomy*, 2010. 11

[40] H. Hoekstra, T. S. van Albada, and R. Sancisi. *MNRAS*, 323:453, 2001. 11

[41] C. Carignan and S. Beaulieu. *Astrophys. J.*, 347:760, 1989. 11

[42] M. Milosavljevic and D. Merritt. *Astrophys. J.*, 563:34, 2001. 11

[43] O. Y. Gnedin and H. Zhao. *MNRAS*, 333:299, 2002. 11

[44] M. D. Weinberg and N. Katz. *Astrophys. J.*, 580:627, 2002. 11

[45] S. Dodelson and L. M. Widrow. *Phys. Rev. Lett.*, 72:17, 1994. 12

[46] A. Kusenko. *Phys. Rept.*, 481:1, 2009. 12, 21

[47] F. Takayama and M. Yamaguchi. *Phys. Lett. B*, 485:388, 2000. 12

[48] W. Buchmüller et al. *JHEP*, 3:037, 2007. 12

[49] D. Gorbunov, A. Khmelnitsky, and V. Rubakov. *JHEP*, 12:055, 2008. 12

[50] A. V. Macciò et al. *MNRAS*, 424:1105, 2012. 12

[51] A. V. Macciò et al. *MNRAS*, 428:3715, 2013. 12

[52] M. Viel et al. *Phys. Rev. D*, 71(6):063534, 2005. 13

[53] U. Seljak et al. *Phys. Rev. Lett.*, 97(19):191303, 2006. 13

[54] K. Abazajian and S. M. Koushiappas. *Phys. Rev. D*, 74(2):023527, 2006. 13

[55] M. Viel et al. *Phys. Rev.*, D88:043502, 2013. 13

[56] M. G. Walker and J. Peñarrubia. *Astrophys. J.*, 742:20, 2011. 13, 48

[57] N. C. Amorisco and N. W. Evans. *MNRAS*, 419:184, 2012. 13

[58] J. R. Jardel and K. Gebhardt. *Astrophys. J.*, 746:89, 2012. 13

[59] A. Boyarsky et al. *JCAP*, 0905:012, 2009. 13

[60] P. Colin, V. Avila-Reese, and O. Valenzuela. *Astrophys. J.*, 542:622, 2000. 13

[61] M. R. Lovell et al. *MNRAS*, 439:300, 2014. 13

[62] L. E. Strigari. *Phys. Rept.*, 531:1, 2013. 13

[63] R. Kennedy et al. *MNRAS*, 442(3):2487, 2014. 13

[64] E. D. Carlson, M. E. Machacek, and L. J. Hall. *Astrophys. J.*, 398:43, 1992. 13

[65] D. N. Spergel and P. J. Steinhardt. *Phys. Rev. Lett.*, 84:3760, 2000. 13

[66] M. Vogelsberger, J. Zavala, and A. Loeb. *MNRAS*, 423:3740, 2012. 13

[67] M. Rocha et al. *MNRAS*, 430:81, 2013. 13

[68] M. Markevitch et al. *Astrophys. J.*, 606:819, 2004. 13, 23

[69] N. Yoshida et al. *Astrophys. J.*, 535:L103, 2000. 14

[70] J. Miralda-Escude. *Astrophys. J.*, 564:60, 2002. 14

[71] A. Loeb and N. Weiner. *Phys. Rev. Lett.*, 106:171302, 2011. 14

[72] P. Tisserand et al. *Astron. Astrophys.*, 469:387, 2007. 14

[73] L. Susskind. *Phys. Rept.*, 104:181, 1984. 15

[74] G. Jungman, M. Kamionkowski, and K. Griest. *Phys. Rept.*, 267:195, 1996. 15, 17

[75] L. Bergstrom. *Rept. Prog. Phys.*, 63:793, 2000. 15, 17

[76] G. Bertone, D. Hooper, and J. Silk. *Phys. Rept.*, 405:279, 2005. 15, 17

[77] J. L. Feng. *Ann. Rev. Astron. Astrophys.*, 48:495, 2010. 15

[78] P. A. R. Ade et al. (Planck Collaboration). arXiv:1502.01589. 16, 19, 20, 23

[79] G. Steigman, B. Dasgupta, and J. F. Beacom. *Phys. Rev.*, D86:023506, 2012. 16

[80] M. Kamionkowski. arxiv:0706.2986. 2007. 17

[81] J. R. Ellis et al. *Nucl. Phys.*, B238:453–476, 1984. 17

[82] L. Roszkowski, E. M. Sessolo, and A. J. Williams. *JHEP*, 02:014, 2015. 17

[83] O. Klein. *Zeitschrift fur Physik*, 37:895, 1926. 18

[84] G. Servant and T. M. P. Tait. *Nuclear Physics B*, 650:391, 2003. 18, 28

[85] M. Cirelli, N. Fornengo, and A. Strumia. *Nucl. Phys.*, B753:178, 2006. 18, 72

[86] M. Cirelli et al. *JCAP*, 1510(10):026, 2015. 19, 86

[87] K. Griest and M. Kamionkowski. *Phys. Rev. Lett.*, 64:615, 1990. 19

[88] J. F. Beacom, N. F. Bell, and G. D. Mack. *Phys. Rev. Lett.*, 99:231301, 2007. 19

[89] G. D. Mack et al. *Phys. Rev. D*, 78(6):063542, 2008. 19

[90] L. Bergström. *New J. of Phys.*, 11(10):105006, 2009. 19

[91] J. L. Feng. *Ann. Rev. of Astron. and Astrophys.*, 48:495, 2010. 19

[92] K. Griest and M. Kamionkowski. *Phys. Rev. Lett.*, 64:615, 1990. 19

[93] L. Hui. *Phys. Rev. Lett.*, 86:3467, 2001. 19

[94] M. Kaplinghat, L. Knox, and M. S. Turner. *Phys. Rev. Lett.*, 85:3335, 2000. 20

[95] R. D. Peccei and H. R. Quinn. *Phys. Rev. Lett.*, 38:1440, 1977. [,328(1977)]. 20

[96] H. Murayama et al. *Eur.Phys.J.*, C3:264, 1998. 20

[97] M. Hertzberg, M. Tegmark, and F. Wilczek. *Phys.Rev.*, D78:083507, 2008. 20

[98] T. E. Jeltema and S. Profumo. *MNRAS*, 450(2):2143, 2015. 21

[99] S. Bird et al. *Phys. Rev. Lett.*, 116(20):201301, 2016. 21

[100] N. Padmanabhan and D. P. Finkbeiner. *Phys. Rev.*, D72:023508, 2005. 23

[101] T. R. Slatyer, N. Padmanabhan, and D. P. Finkbeiner. *Phys. Rev.*, D80:043526, 2009. 23

[102] O. Buchmueller, M. J. Dolan, and C. McCabe. *JHEP*, 01:025, 2014. 23

[103] O. Buchmueller et al. *JHEP*, 01:037, 2015. 23

[104] L. Bergström, P. Ullio, and J. H. Buckley. *Astropart. Phys.*, 9:137, 1998. 27

[105] F. Aharonian, D. Khangulyan, and D. Malyshev. *Astronom. Astrophys.*, 547:A114, 2012. 27

[106] D. Larson et al. *Astrophys. J. Suppl.*, 192:16, 2011. 27

[107] L. Bergström. *Phys. Lett. B*, 225:372, 1989. 27

[108] L. Bergstrom et al. *Phys. Rev. Lett.*, 95:241301, 2005. 28

[109] H.-C. Cheng, J. L. Feng, and K. T. Matchev. *Phys. Rev. Lett.*, 89:211301, 2002. 28

[110] L. Bergström et al. *Phys. Rev. Lett.*, 95(24):241301, 2005. 28

[111] T. Bringmann, L. Bergström, and J. Edsjö. *JHEP*, 1:49, 2008. 28

[112] H. Goldberg. *Phys. Rev. Lett.*, 50:1419, May 1983. 28

[113] V. Lefranc et al. *Phys. Rev. D*, 91(12):122003, 2015. 29, 69, 87

[114] J. Chang et al. *Nature*, 456:362, 2008. 29

[115] O. Adriani et al. *Nature*, 458:607, 2009. 29

[116] I. Büsching et al. *Astrophys. J.*, 678:L39, 2008. 29

[117] D. Hooper, P. Blasi, and P. Dario Serpico. *JCAP*, 1:25, 2009. 29

[118] P. Blasi. *Phys. Rev. Lett.*, 103(5):051104, 2009. 29

[119] S. Profumo. *Central European Journal of Physics*, 10:1, 2012. 29

[120] A. Boulares. *Astrophys. J.*, 342:807, 1989. 29

[121] A. M. Atoyan, F. A. Aharonian, and H. J. Völk. *Phys. Rev. D*, 52:3265, 1995. 29

[122] L. Bergström, T. Bringmann, and J. Edsjö. *Phys. Rev. D*, 78(10):103520, 2008. 29

[123] A. Sommerfeld. *Annalen der Physik*, 403:257, 1931. 30

[124] J. Hisano, S. Matsumoto, and M. M. Nojiri. *Phys. Rev. Lett.*, 92:031303, 2004. 30

[125] J. Hisano et al. *Phys. Rev. D*, 71:063528, 2005. 30

[126] M. Cirelli, A. Strumia, and M. Tamburini. *Nucl. Phys. B*, 787:152, 2007. 30

[127] N. Arkani-Hamed et al. *Phys. Rev.*, D79:015014, 2009. 30, 31, 103

[128] M. Pospelov and A. Ritz. *Phys. Lett. B*, 671:391, 2009. 30

[129] M. Lattanzi and J. Silk. *Phys. Rev.*, D79:083523, 2009. 30

[130] A. Pinzke, C. Pfrommer, and L. Bergström. *Phys. Rev. D*, 84(12):123509, 2011. 30

[131] V. Springel et al. *Nature*, 456:73, 2008. 31

[132] M. Boylan-Kolchin, J. S. Bullock, and M. Kaplinghat. *MNRAS*, 415:L40, 2011. 31

[133] T. Bringmann. *New J. Phys.*, 11:105027, 2009. 31

[134] D. Anderhalden and J. Diemand. *JCAP*, 1304:009, 2013. [Erratum: JCAP1308,E02(2013)]. 32

[135] L. Gao et al. *MNRAS*, 419:1721, 2012. 32

[136] L. E. Strigari et al. *Phys. Rev.*, D75:083526, 2007. 32, 48

[137] L. Pieri, G. Bertone, and E Branchini. *MNRAS*, 384:1627, 2008. 32

[138] G. D. Martinez et al. *JCAP*, 0906:014, 2009. 32

[139] X. Chen and M. Kamionkowski. *Phys.Rev.*, D70:043502, 2004. 32

[140] D. Eichler. *Phys.Rev.Lett.*, 63:2440, 1989. 33

[141] A. Arvanitaki et al. *Phys.Rev.*, D79:105022, 2009. 33

[142] C. Arina, T. Hambye, A. Ibarra, and C. Weniger. *JCAP*, 1003:024, 2010. 33

[143] M. Cirelli et al. *Phys. Rev.*, D86:083506, 2012. 33, 105, 106

[144] C. Amsler et al. *Phys. Lett. B*, 667:1, 2008. 33

[145] J. F. Navarro et al. *MNRAS*, 402:21, 2010. 34

[146] A. Koch et al. *Astrophys. J.*, 657:241, 2007. 34

[147] A. R. Duffy et al. *MNRAS*, 390:L64, 2008. [Erratum: MNRAS415,L85(2011)]. 34

[148] M. A. Sánchez-Conde and F. Prada. *MNRAS*, 442(3):2271, 2014. 34, 52, 53

[149] N. Y. Gnedin, K. Tassis, and A. V. Kravtsov. *Astrophys.J.*, 697:55, 2009. 34

[150] J. H. Wise and T. Abel. *MNRAS*, 414:3458, 2011. 34

[151] R. Teyssier. *Astron. Astrophys.*, 385:337, 2002. 34

[152] D. Keres et al. *MNRAS*, 425:2027, 2012. 34

[153] A. Pontzen and F. Governato. *MNRAS*, 421:3464, 2012. 34

[154] R. A. Swaters, B. F. Madore, and M. Trewhella. *Astrophys. J.*, 531:L107, 2000. 35

[155] J. Binney and S. Tremaine. Princeton, NJ: Princeton University Press, 2008. 35, 36, 41

[156] I. King. *Astronom. J.*, 67:471, 1962. 35

[157] O. E. Gerhard. *MNRAS*, 265:213, 1993. 35

[158] D. Massari et al. *Nature Astronomy*, 2:156, 2018. 36

[159] D. Massari and A. Helmi. *Astron. Astrophys.*, 620:A155, 2018. 36

[160] Y. B. Zeldovich et al. *Sov. J. Nucl. Phys.*, 31:664, 1980. [Yad. Fiz., 31, 1286]. 36

[161] G. R. Blumenthal et al. *Astrophys. J.*, 301:27, 1986. 36

[162] R. Jesseit, T. Naab, and A. Burkert. *Astrophys. J.*, 571:L89, 2002. 37, 41

[163] O. Y. Gnedin et al. *Astrophys. J.*, 616:16, 2004. 37

[164] O. Y. Gnedin and J. R. Primack. *Phys. Rev. Lett.*, 93(6):061302, 2004. 37

[165] F. Prada et al. *Phys. Rev. Lett.*, 93(24):241301, 2004. 37

[166] P. Gondolo and J. Silk. *Phys. Rev. Lett.*, 83:1719, 1999. 37, 41, 43

[167] P. Ullio, H. Zhao, and M. Kamionkowski. *Phys. Rev. D*, 64(4):043504, 2001. 37

[168] D. Merritt et al. *Phys. Rev. Lett.*, 88(19):191301, 2002. 37

[169] T. Goerdt et al. *Astrophys. J.*, 725:1707, 2010. 38, 47

[170] A. A. El-Zant et al. *Astrophys. J.*, 607:L75, 2004. 38

[171] O. Y. Gnedin and H. Zhao. *MNRAS*, 333:299, 2002. 38

[172] S. Mashchenko, J. Wadsley, and H. M. P. Couchman. *Science*, 319:174, 2008. 38, 47

[173] M. D. Weinberg and N. Katz. *MNRAS*, 375:425, 2007. 38

[174] A. Klypin et al. *MNRAS.*, 398:1027, 2009. 38

[175] J. A. Sellwood. *Astrophys. J.*, 679:379, 2008. 38

[176] J. Dubinski, I. Berentzen, and I. Shlosman. *Astrophys. J.*, 697:293, 2009. 38

[177] X.X. Xue et al. *Astrophys. J.*, 684:1143, 2008. 38

[178] O. Gnedin et al. *Astrophys. J.*, 720:L108, 2010. 38

[179] B. Little and S. Tremaine. *Astrophys. J.*, 320:493, 1987. 39

[180] R. Catena and P. Ullio. *JCAP*, 1008:004, 2010. 39

[181] J. Bovy and H.-W. Rix. *Astrophys. J.*, 779:115, 2013. 39

[182] F. Iocco et al. *JCAP*, 1111:029, 2011. 40

[183] A. S. Ilyin, K. P. Zybin, and A. V. Gurevich. *J. Exp. Theor. Phys.*, 98:1–13, 2004. [Zh. Eksp. Teor. Fiz.98,5(2004)]. 40

[184] O. Y. Gnedin and J. R. Primack. *Phys. Rev. Lett.*, 93:061302, 2004. 40

[185] D. Merritt. *Phys. Rev. Lett.*, 92:201304, 2004. 40, 41, 43, 96, 97

[186] E. Vasiliev and M. Zelnikov. *Phys. Rev.*, D78:083506, 2008. 40

[187] T. Lacroix, C. Bœhm, and J. Silk. *Phys. Rev.*, D92(4):043510, 2015. 40

[188] P. Ullio, H. Zhao, and M. Kamionkowski. *Phys. Rev.*, D64:043504, 2001. 40

[189] K. M. Ashman and S. E. Zepf. *Globular Cluster Systems*. 2008. 41, 100

[190] P.J.E. Peebles. *Astrophys. J.*, 277:470, 1984. 41, 96

[191] E. Komatsu et al. *Astrophys.J.Suppl.*, 180:330, 2009. 41

[192] J. P. Brodie and J. Strader. *Ann. Rev. Astron. Astrophys.*, 44:193, 2006. 41

[193] H. Baumgardt et al. *MNRAS*, 396:2051, 2009. 41

[194] C. Conroy, A. Loeb, and D. Spergel. *Astrophys. J.*, 741:72, 2011. 41

[195] J. Cohen et al. *Astrophys. J.*, 725:288, 2010. 41

[196] G. R. Blumenthal et al. *Astrophys. J.*, 301:27, 1986. 41, 96

[197] Ya. B. Zeldovich et al. *Sov. J. Nucl. Phys.*, 31:664, 1980. 41, 96

[198] O. Y. Gnedin et al. *Astrophys. J.*, 616:16, 2004. 41

[199] F. Prada et al. *Phys.Rev.Lett.*, 93:241301, 2004. 41

[200] B. Lanzoni et al. *Astrophys. J. Lett.*, 668, 2007. 41, 83, 95, 98

[201] E. Noyola, K. Gebhardt, and M. Bergmann. *Astrophys. J.*, 676:1008, 2008. 41, 42, 83

[202] A. K. H. Kong. *Astrophys. J.*, 661:875, 2007. 41

[203] J. S. Ulvestad, J. E. Greene, and L. C. Ho. *Astrophys. J.*, 661:L151, 2007. 41

[204] C. L. Fryer and V. Kalogera. *Astrophys.J.*, 554:548, 2001. 42

[205] J. M. Silverman and A. V. Filippenko. *Astrophys. J.*, 678:L17, 2008. 42

[206] L. Ferrarese and H. Ford. *Space Sci.Rev.*, 116:523, 2005. 42

[207] J. E. Greene and L. C. Ho. arXiv:0707.2617. 2007. 42

[208] J. Magorrian et al. *Astron.J.*, 115:2285, 1998. 42

[209] E. Colbert and A. Ptak. *Astrophys. J. Suppl.*, 143:25, 2002. 42

[210] D. A. Swartz et al. *Astrophys. J. Suppl.*, 154:519, 2004. 42

[211] G. C. Dewangan et al. *Astrophys. J.*, 635:198, 2005. 42

[212] J. Frank and M.J.af Cambridge U. Rees. *MNRAS*, 176:633, 1976. 42

[213] B. M. Petersen et al. *Astrophys. J.*, 632:799, 2005. 42

[214] R. R. Islam, J. E. Taylor, and J. Silk. *MNRAS*, 340:647, 2003. 42

[215] M. Volonteri, F. Haardt, and P. Madau. *Astrophys.J.*, 582:559, 2003. 42

[216] S. M. Koushiappas, J.S. Bullock, and A. Dekel. *MNRAS*, 354:292, 2004. 42

[217] G. Bertone, A. R. Zentner, and J. Silk. *Phys. Rev.*, D72:103517, 2005. 42, 43, 89, 91, 93

[218] P. Madau and M. J. Rees. *Astrophys. J.*, 551:L27, 2001. 42

[219] A. Heger et al. *Astrophys.J.*, 591:288, 2003. 42

[220] M. G. Haehnelt and M. J. Rees. *MNRAS*, 263:168, 1993. 42

[221] A. Loeb and F. A. Rasio. *Astrophys. J.*, 432:52, 1994. 42

[222] D. Eisenstein and A. Loeb. *Astrophys.J.*, 443:11, 1995. 42

[223] M. G. Haehnelt, P. Natarajan, and M. J. Rees. *MNRAS*, 300(817), 1998. 42

[224] O. Y. Gnedin. *Class. Quant. Grav.*, 18:3983, 2001. 42

[225] V. Bromm and A. Loeb. *Astrophys. J.*, 596:34, 2003. 42

[226] G. D. Quinlan, L. Hernquist, and S. Sigurdsson. *Astrophys. J.*, 440:554, 1995. 43

[227] F. Aharonian et al. (H.E.S.S. Collaboration). *Astrophys. J.*, 691:175, 2009. 44, 79, 86

[228] T. Bringmann, J. Lavalle, and P. Salati. *Phys. Rev. Lett.*, 103:161301, 2009. 44, 93

[229] V. Springel et al. *Nature*, 456:73, 2008. 44

[230] J. Diemand et al. *Nature*, 454:735, 2008. 44

[231] R.A. Ibata, G. Gilmore, and M.J. Irwin. *Nature*, 370:194, 1994. 46

[232] A. Albert et al. *Astrophys. J.*, 834(2):110, 2017. 46

[233] N. W. Evans, F. Ferrer, and S. Sarkar. *Phys. Rev.*, D69:123501, 2004. 47

[234] J. T. Kleyna et al. *Astrophys. J.*, 588:L21, 2003. 47

[235] T. Goerdt et al. *MNRAS*, 368:1073, 2006. 47

[236] M. Walker et al. *Astrophys. J.*, 704:1274, 2009. 47, 82

[237] J. I. Read and G. Gilmore. *MNRAS*, 356:107, 2005. 47

[238] F. Governato et al. *Nature*, 463:203, 2010. 47

[239] D. R. Cole, W. Dehnen, and M. I. Wilkinson. *MNRAS*, 416:1118, 2011. 47

[240] S. Koposov et al. *Astrophys. J.*, 686:279, 2008. 47

[241] E. J. Tollerud et al. *Astrophys. J.*, 688:277, 2008. 47

[242] J. S. Bullock. *arXiv:1009.4505*, 2010. 47

[243] J. R. Hargis, B. Willman, and A. H. G. Peter. *Astrophys. J. Lett.*, 795:L13, 2014. 47, 84

[244] K. Bechtol et al. (DES Collaboration). *Astrophys. J.*, 807(1):50, 2015. 47

[245] S. E. Koposov et al. *Astrophys. J.*, 805(2):130, 2015. 47

[246] G. Gilmore et al. *Astrophys. J.*, 663:948, 2007. 48

[247] A. W. McConnachie. *Astron. J.*, 144:4, 2012. 48

[248] K. Hayashi and M. Chiba. *Astrophys. J.*, 755:145, 2012. 48

[249] A. Geringer-Sameth, S. M. Koushiappas, and M. Walker. *Astrophys. J.*, 801(2):74, 2015. 48, 49

[250] L. E. Strigari, C. S. Frenk, and S. D. M. White. *Astrophys. J.*, 838(2):123, 2017. 48

[251] M. I. Wilkinson et al. *MNRAS*, 330:778, 2002. 48

[252] L. E. Strigari, J. S. Bullock, and M. Kaplinghat. *Astrophys. J.*, 657:L1, 2007. 48

[253] J. Wolf et al. *MNRAS*, 406:1220, 2010. 49

[254] G. D. Martinez. *MNRAS*, 451(3):2524, 2015. 49, 84

[255] V. Bonnivard et al. *MNRAS*, 453(1):849, 2015. 49, 65

[256] E. N. Kirby et al. *Astrophys. J.*, 814(1):L7, 2015. 49

[257] E. N. Kirby et al. *Astrophys. J.*, 838:83, Apr 2017. 49

[258] V. Bonnivard and others. *Astrophys. J.*, 808:L36, 2015. 49, 84

[259] A. Genina and M. Fairbairn. *MNRAS*, 463(4):3630, 2016. 49

[260] Y. Zhao et al. *Phys. Rev.*, D97(6):063013, 2018. 49

[261] S. Courteau et al. *Rev. Mod. Phys.*, 86:47, 2014. 50

[262] J. Klimentowski et al. *MNRAS*, 400:2162, 2009. 50

[263] J. Klimentowski et al. *MNRAS*, 378:353, 2007. 50

[264] V. Bonnivard et al. *MNRAS*, 462(1):223, 2016. 50

[265] M. G. Walker and J. Peñarrubia. *Astrophys. J.*, 742:20, 2011. 51

[266] N. C. Amorisco and N. W. Evans. *MNRAS*, 419:184, 2012. 51

[267] T. Richardson and M. Fairbairn. *MNRAS*, 441:1584, 2014. 51

[268] V. Bonnivard et al. *MNRAS*, 446:3002, 2015. 51

[269] A. Dekel et al. *Nature*, 437:707, 2005. 51

[270] G. Battaglia et al. *Astron. Astrophys.*, 459:423, 2006. 51

[271] D. Merritt. *Astrophys. J.*, 313:121, 1987. 51

[272] V. Lefranc et al. *JCAP*, 1609(09):043, 2016. 52, 88

[273] A. Pinzke, C. Pfrommer, and L. Bergstrom. *Phys. Rev. Lett.*, 103:181302, 2009. 52, 53, 103

[274] A. Pinzke, C. Pfrommer, and L. Bergstrom. *Phys. Rev.*, D84:123509, 2011. 52, 53

[275] T. E. Jeltema, J. Kehayias, and S. Profumo. *Phys. Rev. D*, 80:023005, 2009. 52, 53, 101, 103

[276] P. Blasi, S. Gabici, and G. Brunetti. *Int. J. Mod. Phys.*, A22:681, 2007. 52

[277] S. Colafrancesco and P. Blasi. *Astropart. Phys.*, 9:227, 1998. 52

[278] R. Dongsu et al. *Astrophys. J.*, 593:599, 2003. 52

[279] H. J. Völk, F. A. Aharonian, and D. Breitschwerdt. *Space Sc. Rev.*, 75:279, 1996. 52

[280] J. A. Hinton and W. Domainko. *MNRAS*, 382:466, 2007. 52

[281] T. H. Reiprich and H. Boehringer. *Astrophys. J.*, 567:716, 2002. 53, 101

[282] G. Pedaletti, S. J. Wagner, and F. M. Rieger. *Astrophys. J.*, 738(2):142, 2011. 53

[283] M. Ackermann et al. *Astrophys. J. Lett.*, 717(1):L71, 2010. 53

[284] M. Ackermann et al. *JCAP*, 5:025, 2010. 53, 101

[285] A. Abramowski et al. (H.E.S.S. collaboration). *Astrophys. J.*, 750:123, 2012. 53, 103, 104

[286] J. A. Hinton and W. Hofmann. *Ann. Rev. of Astron. and Astrophys.*, 47:523, 2009. 54

[287] F. Aharonian et al. *Rept. Prog. Phys.*, 71:096901, 2008. 54

[288] P. M. Chadwick et al. *J. of Phys. G Nucl. Phys.*, 35(3):033201, 2008. 54

[289] J. Holder. *Astropart. Phys.*, 39:61, 2012. 54

[290] T. C. Weekes et al. *Astrophys. J.*, 342:379, 1989. 54

[291] http://tevcat.uchicago.edu. 54

[292] F. Acero et al. (H.E.S.S. collaboration). *Science*, 326:1080, 2009. 54

[293] V. A. Acciari et al. *Nature*, 462:770, 2009. 54

[294] A. Abramowski et al. (H.E.S.S. collaboration). *Astronom. Astrophys.*, 531:L18, 2011. 54, 95

[295] F. Aharonian et al. (H.E.S.S. collaboration). *Nature*, 439:695, 2006. 54, 120

[296] A. Abramowski et al. (H.E.S.S. collaboration). *Nature*, 531:476, 2016. 54, 114, 115, 121, 122, 124, 129

[297] F. Aharonian et al. (H.E.S.S. collaboration). *Phys. Rev. Lett.*, 101:170402, 2008. 54

[298] F. Aharonian et al. *Nature*, 440:1018–1021, 2006. 54

[299] A. Abramowski et al. (H.E.S.S. collaboration). *Phys. Rev. Lett.*, 106:161301, 2011. 54, 65, 66, 67

[300] H. Abdallah et al. (H.E.S.S. collaboration). *Phys. Rev. Lett.*, 117(11):111301, 2016. 54, 65, 66, 67, 76

[301] H. Abdallah et al. (H.E.S.S. collaboration). *Phys. Rev. Lett.*, 120(20):201101, 2018. 54, 67, 76

[302] F. Aharonian et al. *Reports on Progress in Physics*, 71(9):096901, 2008. 56

[303] The HEGRA experiment. http://www.mpi-hd.mpg.de/hfm/HEGRA/. 56

[304] The CANGAROO experiment. http://icrhp9.icrr.u-tokyo.ac.jp/. 59

[305] The HESS experiment. http://www.mpi-hd.mpg.de/hfm/HESS/. 59

[306] J. Aleksić et al. *Astronom. Astrophys.*, 544:A96, 2012. 59

[307] The VERITAS experiment. http://veritas.sao.arizona.edu/. 59

[308] M. Actis et al. (CTA Consortium). *Exp. Astron.*, (32):193, 2011. 60

[309] B. S. Acharya et al. *(CTA consortium) arXiv:1709.07997*. 2018. 60, 64, 69, 87, 92

[310] A. Viana. *Indirect searches of dark matter and the galactic center at very high energy with H.E.S.S.* PhD thesis, Université Paris Diderot, Ecole doctorale N576 PHENIICS, 2012. 64, 84, 110

[311] V. Lefranc. *Recherche de matière noire, observation du centre Galactique avec H.E.S.S. et modernisation des caméras de H.E.S.S. I.* PhD thesis, Université Paris-Saclay, Ecole doctorale N576 PHENIICS, 2016. 64, 65, 86, 87, 110, 114, 119

[312] L. Rinchiuso. *Study of the Galactic Center and dark matter search with H.E.S.S.* PhD thesis, Université Paris-Saclay, Ecole doctorale N576 PHENIICS, 2019. 64, 65, 68, 74, 75, 76, 85, 110

[313] A. Abramowski et al. (H.E.S.S. collaboration). *Phys. Rev. Lett.*, 114(8):081301, 2015. 65

[314] W. A. Rolke, A. M. Lopez, and J. Conrad. *Nucl. Instrum. Meth.*, A551:493, 2005. 65

[315] J. Aleksic et al. (MAGIC collaboration). *JCAP*, 1402:008, 2014. 65, 67, 86

[316] A. Abramowski et al. (H.E.S.S. collaboration). *Phys. Rev.*, D90:112012, 2014. 65, 67, 79, 84, 86

[317] M. Ackermann et al. (Fermi-LAT Collaboration). *Phys. Rev. Lett.*, 115(23):231301, 2015. 65, 67, 86

[318] M. Ackermann et al. (Fermi-LAT collaboration). *Phys. Rev.*, D91(12):122002, 2015. 67

[319] H. Silverwood et al. *JCAP*, 1503(03):055, 2015. 69, 70

[320] G. Cowan et al. *European Physical Journal C*, 71:1554, 2011. 69

[321] M. Ackermann et al. (Fermi-LAT collaboration). *Astrophys. J.*, 750:3, 2012. 69

[322] M. Ackermann et al. Fermi-LAT Collaboration. *Astrophys. J.*, 799:86, 2015. 69

[323] `http://fermi.gsfc.nasa.gov/ssc/data/access/lat/BackgroundModels.html`. 69

[324] B. Anderson. in 5^{th} Fermi Symposium October 20 - 24, 2014, Nagoya, Japan. 71

[325] G. F. Giudice et al. *JHEP*, 12:027, 1998. 72

[326] L. Randall and R. Sundrum. *Nucl. Phys.*, B557:79, 1999. 72

[327] A. Arvanitaki et al. *JHEP*, 02:126, 2013. 72

[328] N. Arkani-Hamed et al. arXiv:1212.6971. 2012. 72

[329] J. Hisano et al. *Phys. Lett.*, B646:34, 2007. 72, 86

[330] A. Hryczuk, R. Iengo, and P. Ullio. *JHEP*, 03:069, 2011. 72

[331] M. Beneke et al. *JHEP*, 03:119, 2016. 72

[332] M. Baumgart et al. *JHEP*, 01:036, 2019. 72, 73

[333] J. Hisano et al. *Phys. Rev.*, D71:063528, 2005. 72

[334] M. Baumgart and V. Vaidya. *JHEP*, 03:213, 2016. 72, 73

[335] L. Rinchiuso et al. *Phys. Rev.*, D98(12):123014, 2018. 73, 74

[336] M. Baumgart et al. *JHEP*, 03:117, 2018. 73

[337] A. Hryczuk et al. *JHEP*, 10:043, 2019. 76, 77

[338] F. Aharonian et al. (H.E.S.S. Collaboration). *Astropart. Phys.*, 29:55, 2008. 79, 81, 83, 86

[339] A. Abramowski et al. (H.E.S.S. collaboration). *Astropart. Phys.*, 34:608, 2011. 79, 86

[340] J. H. An and N. W. Evans. *Astrophys. J.*, 701:1500, 2009. 79

[341] G. Battaglia. *PhD thesis*. PhD thesis, Univ. Groningen, The Netherlands, 2007. 79

[342] G. Battaglia et al. *Astrophys. J.*, 681:L13, 2008. 79

[343] L. P. Osipkov. *Pisma v Astronomicheskii Zhurnal*, 5:77, 1979. 79

[344] D. Merritt. *Astronom. J.*, 90:1027, June 1985. 79

[345] A. Abramowski et al. (H.E.S.S. Collaboration). *Astropart. Phys.*, 34:608, 2011. 80

[346] L. Bergstrom, P. Ullio, and J. H. Buckley. *Astropart. Phys.*, 9:137, 1998. 80

[347] A. Viana et al. *Astrophys. J.*, 746:77, 2012. 80, 83

[348] R. Ibata et al. *Astrophys. J.*, 547:L133, 2001. 81

[349] M. Mateo, E. W. Olszewski, and H. L. Morrison. *Astrophys. J.*, 508:L55, 1998. 81

[350] S. R. Majewski et al. *Astron. J.*, 118:1709, 1999. 81

[351] S. R. Majewski et al. *Astrophys. J.*, 599:1082, 2003. 81

[352] D. Martinez-Delgado et al. *Astrophys. J.*, 549:L199, 2001. 81

[353] D. Martinez-Delgado et al. *Astrophys. J.*, 601:242, 2004. 81

[354] V. Belokurov et al. *Astrophys. J.*, 642:L137, 2006. 81

[355] L. L. Watkins et al. *MNRAS*, 398:1757, 2009. 81

[356] S. R. Majewski et al. 2003. [IAU Symp.220,189(2004)]. 81

[357] J. Penarrubia, J. F. Navarro, and A. W. McConnachie. *Astrophys.J.*, 673, 2007. 81

[358] M. Niederste-Ostholt et al. *Astrophys. J.*, 712:516, 2010. 82

[359] J. Penarrubia et al. *Astrophys. J.*, 698:222, 2009. 82

[360] J. Penarrubia, A. McConnachie, and J. F. Navarro. *Astrophys. J.*, 672:904, 2008. 82

[361] J. S. Bullock et al. *MNRAS*, 321:559, 2001. 82

[362] E. L. Lokas et al. *Astrophys. J.*, 725:1516, 2010. 82

[363] J. Penarrubia et al. *MNRAS*, 408:L26, 2010. 82

[364] M. Mateo. *Ann. Rev. Astron. Astrophys.*, 36:435, 1998. 82

[365] M. Fellhauer et al. *New Astron.*, 5:305, 2000. 83

[366] A. A. Abdo et al. (Fermi-LAT collaboration). *Astron. Astrophys.*, 524:A75, 2010. 83, 100

[367] R. Ibata et al. *Astrophys. J.*, 699:L169, 2009. 83

[368] V. Belokurov et al. *Astrophys. J.*, 654:897, 2007. 84

[369] L. E. Strigari et al. *Astrophys. J.*, 678:614, 2008. 84

[370] R. R. Munoz, M. Geha, and B. Willman. *Astron. J.*, 140:138, 2010. 84

[371] A. Drlica-Wagner et al. *Astrophys. J.*, 2015. 84, 86

[372] A. Geringer-Sameth and others . *Phys. Rev. Lett.*, 115(8):081101, 2015. 84, 86

[373] D. Hooper and T. Linden. *JCAP*, 1509(09):016, 2015. 84, 86

[374] `http://pan-starrs.ifa.hawaii.edu/public/`. 84

[375] N. Kaiser et al. *Proc.SPIE Int.Soc.Opt.Eng.*, 4836:154, 2002. 84

[376] `http://www.darkenergysurvey.org/`. 84

[377] B. Flaugher. The Dark Energy Survey. *Int.J.Mod.Phys.*, A20:3121, 2005. 84

[378] `http://www.lsst.org/lsst/`. 84

[379] J.A. Tyson and others . *Nucl. Phys. Proc. Suppl.*, 124:21, 2003. 84

[380] `http://fermi.gsfc.nasa.gov/`. 86

[381] E. Aliu et al. (MAGIC Collaboration). *Astrophys. J.*, 697:1299, 2009. 86

[382] J. Albert et al. (MAGIC Collaboration). *Astrophys. J.*, 679:428, 2008. 86

[383] V. A. Acciari et al. (VERITAS Collaboration). *Astrophys. J.*, 720:1174, 2010. 86

[384] E. Aliu et al. (VERITAS Collaboration). *Phys. Rev. D*, 85:062001, 2012. 86

[385] M. Actis et al. (CTA Consortium). *Experimental Astronomy*, 32:193, 2011. 86

[386] M. Cirelli, A. Strumia, and M. Tamburini. *Nucl. Phys.*, B787:152, 2007. 86

[387] C. Garcia-Cely et al. *arXiv:1507.05536*, 2015. 86

[388] M. Doro et al. *Astropart.Phys.*, 43:189, 2013. 86

[389] B. Anderson et al. *Astrophys. J.*, 718:899, 2010. 89

[390] C. Giocoli, L. Pieri, and G. Tormen. *MNRAS*, 387:689, 2008. 89

[391] L. Pieri et al. *Phys. Rev.*, D83:023518, 2011. 89

[392] N. Mirabal, D. Nieto, and S. Pardo. *arXiv:1007.2644*, 2010. 89

[393] M. R. Buckley and D. Hooper. *Phys. Rev.*, D82:063501, 2010. 89

[394] J. Coronado-Blazquez et al. *JCAP*, 1907:020, 2019. 89

[395] F. Aharonian et al. (H.E.S.S. collaboration). *Phys. Rev.*, D78:072008, 2008. 89, 91, 92

[396] P. Brun et al. *Phys. Rev.*, D83:015003, 2011. 92

[397] E. Moulin. In *Proceedings of the 5th International Conference, Beyond 2010, Cape Town, South Africa, February 1-6, 2010*, page 557, 2011. 93

[398] E. Zackrisson and T. Riehm. *Adv.Astron.*, 2010:478910, 2010. 94

[399] J. Chen and S. Koushiappas. *Astrophys.J.*, 724:400, 2010. 94

[400] H. Garsden, N.F. Bate, and G.F. Lewis. *MNRAS*, 420:3574, 2012. 94

[401] A. Geringer-Sameth and S. M. Koushiappas. *MNRAS*, 425:862, 2012. 94

[402] R. G. Carlberg and C. J. Grillmair. *Astrophys.J.*, 768:171, 2013. 94

[403] C. J. Grillmair et al. *Astrophys. J. Lett.*, 769:L23, 2013. 94

[404] C. J. Grillmair. *Astrophys. J. Lett.*, 790:L10, 2014. 94

[405] J. Hargis et al. NOAO Proposal, 2014. 94

[406] B. Sesar et al. *Astrophys. J.*, 793:135, 2014. 94

[407] D. Erkal and V. Belokurov. *MNRAS*, 450(1):1136, 2015. 94

[408] S. Kabuki et al. *Astrophys. J.*, 668:968, 2007. 95

[409] F. Aharonian et al. (H.E.S.S. Collaboration). *Astron. Astrophys.*, 499:273, 2009. 95

[410] M. McCutcheon. (VERITAS Collaboration) arXiv:0907.4974. 2009. 95

[411] M. Wood et al. *Astrophys. J.*, 677:906, 2008. 95, 96, 97, 99, 100

[412] `http://www.physics.mcmaster.ca/~harris/mwgc.dat`. 95

[413] L.R. Yungelson et al. *Astron. Astrophys.*, 477:223, 2008. 95

[414] H. Baumgardt, J. Makino, and P. Hut. *Astrophys.J.*, 620:238, 2005. 95

[415] E. Noyola and K. Gebhardt. *Astron. J.*, 132:447, 2006. 95

[416] S. Umbreit, J. M. Fregeau, and F. A. Rasio. *IAU Symp.*, 246:351, 2008. 95

[417] A.A. Nucita et al. arxiv:0712.1134. 95

[418] J. D. Dull et al. *Astrophys. J.*, 481:267, 1997. 95, 97

[419] J. Gerssen et al. *Astron. J.*, 124:3270, 2002. 95

[420] A. A. Kiselev et al. *Astron. Lett.*, 34:529, 2008. 95

[421] F. De Paolis, V.G. Gurzadian, and G. Ingrosso. *Astron.Astrophys.*, 315:396, 1996. 95

[422] A. Abramowski et al. (H.E.S.S. Collaboration). *Astrophys.J.*, 735:12, 2011. 95, 96

[423] S. L. Shapiro and S. A. Teukolsky. *Black Holes, White Dwarfs, and Neutron Stars.* Wiley-Interscience, New York, 1983, 672 p., 1983. 96, 97

[424] D. Merritt, S. Harfst, and G. Bertone. *Phys. Rev.*, D75:043517, 2007. 96, 97, 99

[425] G. Bertone and M. Fairbairn. *Phys. Rev.*, D77:043515, 2008. 96, 97, 99

[426] C. Amsler et al. *Phys. Lett.*, B667:1, 2008. 96

[427] K. Gebhardt et al. *Astron. J.*, 113:1026, 1997. 97

[428] G. Meylan and C. Pryor. In *Proc. of the workshop Structure and Dynamics of Globular Clusters*, 1993. 98

[429] A. Abramowski et al. (H.E.S.S. collaboration). *Astron. Astrophys.*, 531:L18, 2011. 101

[430] F. Aharonian et al. (H.E.S.S. Collaboration). *Science*, 314:1424, 2006. 101

[431] D. A. Buote et al. *Astrophys. J.*, 664:123, 2007. 101

[432] M. J. Drinkwater, M. D. Gregg, and M. Colless. *Astrophys. J.*, 548:L139, 2001. 102

[433] M. Paolillo et al. *Astrophys. J.*, 565:883, 2002. 102

[434] A. Pinzke and C. Pfrommer. *MNRAS*, 409:449, 2010. 103

[435] C. Pfrommer, T. A. Ensslin, and V. Springel. *MNRAS*, 385:1211, 2008. 103

[436] M. Ackermann et al. (Fermi-LAT Collaboration). *JCAP*, 5:25, 2010. 104

[437] Y. Nomura and J. Thaler. *Phys. Rev.*, D79:075008, 2009. 103

[438] J. Bovy. *Phys. Rev.*, D79:083539, 2009. 103

[439] S. Profumo and T. E. Jeltema. *JCAP*, 0907:020, 2009. 103

[440] R. Schodel et al. *Submitted to: Nature*, 2002. 110

[441] A. M. Ghez et al. *Astron. Nachr.*, 324:S1, 2003. 110

[442] F. Eisenhauer et al. *Astrophys. J.*, 628:246, 2005. 110

[443] S. Gillessen et al. *Astrophys. J.*, 692:1075, 2009. 110

[444] R. Genzel and V. Karas. *IAU Symp.*, 238:173, 2007. 110

[445] F. Melia. *The Galactic Supermassive Black Hole, Princeton University Press.* 110

[446] R. Genzel, F. Eisenhauer, and S. Gillessen. *Rev. of Mod. Phys.*, 82:3121, 2010. 110

[447] Z. Malkin. *Astron. Rep.*, 57:128, 2013. 110

[448] T. N. LaRosa et al. *Astronom. J.*, 119:207, 2000. 111, 112

[449] M. Tsuboi, T. Handa, and N. Ukita. *Astrophys. J. Suppl. Series*, 120(1):1, 1999. 113

[450] K. Ferrière, W. Gillard, and P. Jean. *Astron. Astrophys.*, 467:611, 2007. 113

[451] P. A. Jones et al. *MNRAS*, 419:2961, 2012. 113

[452] P. J. Barnes et al. *Astrophys. J.*, 812:6, 2015. 113

[453] S. Molinari et al. *Astrophys. J.l*, 735:L33, 2011. 113

[454] D. Pierce-Price et al. *Astrophys. J.*, 545:L121, 2000. 113

[455] M. P. Muno et al. *Astrophys. J. Suppl.*, 181:110, 2009. 113

[456] R. Launhardt, R. Zylka, and P. G. Mezger. *Astron. Astrophys.*, 384:112, 2002. 113

[457] K. Kosack et al. *Astrophys. J.*, 608:L97, 2004. 113

[458] K. Tsuchiya et al. *Astrophys. J.*, 606:L115, 2004. 113

[459] F. Aharonian et al. (h.e.s.s. collaboration). *Astron. Astrophys.*, 425:L13, 2004. 113

[460] F. Aharonian et al. *Phys. Rev. Lett.*, 97:221102, 2006. 113

[461] J. Albert et al. *Astrophys. J.*, 638:L101, 2006. 113

[462] A. Archer et al. *Astrophys. J.*, 790(2):149, 2014. 113

[463] F. Aharonian et al. (H.E.S.S. Collaboration). *Astron. Astrophys.*, 503:817, 2009. 114, 115, 116

[464] F. Acero et al. (Fermi-LAT Collaboration). *Astrophys. J. Suppl.*, 218(2):23, 2015. 115

[465] S. Abdollahi et al. (Fermi-LAT Collaboration) arXiv:1902.10045. 2019. 115

[466] Q. D. Wang, F. J. Lu, and E. V. Gotthelf. *MNRAS*, 367:937, 2006. 116

[467] W. Bednarek and T. Sobczak. *MNRAS*, 435:L14, 2013. 116

[468] F. Acero et al. (H.E.S.S. Collaboration). *MNRAS*, 402:1877, 2010. 116, 125

[469] J. A. Hinton and F. A. Aharonian. *Astrophys. J.*, 657:302, 2007. 117

[470] F. Aharonian and A. Neronov. *Astrophys. J.*, 619:306, 2005. 117, 118

[471] W. Bednarek and T. Sobczak. *MNRAS*, 435:L14, 2013. 118, 129, 131

[472] P. G. Mezger, W. J. Duschl, and R. Zylka. *Astron. Astrophys. Review*, 7:289, 1996. 118

[473] M. D. Kistler. *ArXiv:1511.01159*, 2015. 118, 131

[474] M. Ajello et al. (Fermi-LAT Collaboration), arXiv:1705.00009. 2017. 118, 128, 132, 133

[475] M. Ackermann et al. (Fermi-LAT Collaboration). *Astrophys. J.*, 840(1):43, 2017. 118, 134

[476] A. V. Belikov, G. Zaharijas, and J. Silk. *Phys. Rev. D*, 86(8):083516, 2012. 118

[477] J. A. R. Cembranos, V. Gammaldi, and A. L. Maroto. *Phys. Rev.*, D86:103506, 2012. 118

[478] G. Bertone and D. Merritt. *Phys. Rev.*, D72:103502, 2005. 118

[479] T. Bringmann et al. *Phys. Rev.*, D84:103525, 2011. 119

[480] A. Ibarra, Lopez G. S., and M. Pato. *JCAP*, 1207:043, 2012. 119

[481] A. Ibarra et al. *JCAP*, 1305:016, 2013. [Erratum: JCAP1603,no.03,E01(2016)]. 119

[482] A. V. Belikov and J. Silk. *Phys. Rev. Lett.*, 111(7):071302, 2013. 119

[483] A. V. Belikov, E. Moulin, and J. Silk. *Phys. Rev.*, D94(10):103005, 2016. 119, 120

[484] `https://portal.cta-observatory.org/Pages/CTA-Performance.aspx`. 119

[485] M. Tsuboi, T. Handa, and N. Ukita. *Astrophys. J. Suppl.*, 120:1, 1999. 121

[486] K. Ferriere, W. Gillard, and P. Jean. *Astron. Astrophys.*, 467:611, 2007. 121

[487] R. M. Crocker et al. *MNRAS*, 413(2):763, 2011. 122

[488] F. A. Aharonian. *Very high energy cosmic gamma radiation: A crucial window on the extreme universe*. 2004. 123

[489] M. Clavel et al. *Astron. Astrophys.*, 558:A32, 2013. 124

[490] M. Su, T. R. Slatyer, and D. P. Finkbeiner. *Astrophys. J.*, 724:1044, 2010. 124

[491] S. Celli, A. Palladino, and F. Vissani. arxiv:1604.08791. 2016. 124

[492] AR Bell, KM Schure, B Reville, and G Giacinti. *MNRAS*, 431:415, 2013. 125

[493] A. M. Bykov. *Astron. Astrophys. Rev.*, 22(1):77, 2014. 126

[494] F. Yusef-Zadeh et al. *Astrophys. J.*, 762:33, 2013. 126

[495] L. Goodenough and D. Hooper. arxiv:0910.2998. 2009. 128, 129

[496] K. N. Abazajian and M. Kaplinghat. *Phys. Rev.*, D86:083511, 2012. [Erratum: Phys. Rev.D87,129902(2013)]. 128

[497] D. Hooper and T. R. Slatyer. *Phys. Dark Univ.*, 2:118, 2013. 128

[498] K. N. Abazajian et al. *Phys. Rev.*, D90(2):023526, 2014. 128

[499] F. Calore, I. Cholis, and C. Weniger. *JCAP*, 2015(03):038, 2015. 128

[500] J. Petrović, P. Serpico, and G. Zaharijaš. *JCAP*, 10:052, 2014. 128

[501] D. Gaggero et al. *JCAP*, 1512:056, 2015. 128

[502] E. Carlson, S. Profumo, and T. Linden. *Phys. Rev. Lett.*, 117:111101, 2016. 128

[503] W. Wang, Z. J. Jiang, and K. S. Cheng. *MNRAS*, 358:263, 2005. 128

[504] I. Cholis, D. Hooper, and T. Linden. *JCAP*, 1506(06):043, 2015. 128

[505] R. Bartels, S. Krishnamurthy, and C. Weniger. *Phys. Rev. Lett.*, 116:051102, 2016. 128, 129

[506] T. Lacroix, J. Silk, E. Moulin, and C. Bœhm. *Phys. Rev.*, D94(12):123008, 2016. 129, 130, 131

[507] K. N. Abazajian and M. Kaplinghat. *Phys. Rev. D*, 86(8):083511, 2012. 129

[508] C. Gordon and O. Macías. *Phys. Rev. D*, 88(8):083521, 2013. 129

[509] O. Macías and C. Gordon. *Phys. Rev. D*, 89(6):063515, 2014. 129

[510] K. N. Abazajian. *JCAP*, 3:10, 2011. 129

[511] R. S. Wharton et al. *Astrophys. J.*, 753:108, 2012. 129

[512] N. Mirabal. *MNRAS*, 436:2461, 2013. 129

[513] Q. Yuan and B. Zhang. *J. of High Energy Astrophys.*, 3:1, 2014. 129

[514] J. Petrović, P. D. Serpico, and G. Zaharijas. *JCAP*, 2:23, 2015. 129

[515] T. D. Brandt and B. Kocsis. *Astrophys. J.*, 812:15, 2015. 129

[516] V. Vitale and Morselli A. arXiv:0912.3828. 129

[517] D. Hooper and L. Goodenough. *Phys. Lett. B*, 697:412, 2011. 129

[518] D. Hooper and T. Linden. *Phys. Rev. D*, 84(12):123005, 2011. 129

[519] K. N. Abazajian and M. Kaplinghat. *Phys. Rev. D*, 87(12):129902, 2013. 129

[520] K. N. Abazajian et al. *Phys. Rev. D*, 90(2):023526, 2014. 129

[521] T. Daylan et al. *Physics of the Dark Universe*, 12:1, 2016. 129

[522] F. Calore et al. *Phys. Rev. D*, 91(6):063003, March 2015a. 129

[523] Q. Yuan and K. Ioka. *Astrophys. J.*, 802:124, April 2015. 129

[524] P. Ullio, H. Zhao, and M. Kamionkowski. *Phys. Rev. D*, 64(4):043504, 2001. 130

[525] O. Y. Gnedin and J. R. Primack. *Phys. Rev. Lett.*, 93(6):061302, 2004. 130

[526] G. Gilmore and R. F. G. Wyse. In S. Deiters et al., editors, *Dynamics of Star Clusters and the Milky Way*, volume 228 of *Astronomical Society of the Pacific Conference Series*, page 225, 2001. 130

[527] R. M. Crocker et al. *Nature*, 463:65, 2010. 131

[528] J. A. Hinton and F. A. Aharonian. *Astrophys. J.*, 657:302, 2007. 131

[529] R. P. Eatough et al. *Nature*, 501:391, 2013. 131

[530] K. Mori et al. *Astrophys. J.*, 814:94, 2015. 131

[531] K. Perez et al. *Nature*, 520:646, 2015. 131

[532] G. Fragione, F. Antonini, and O. Y. Gnedin. *MNRAS*, 475:5313, 2018. 132

[533] G. Fragione, V. Pavlík, and S. Banerjee. *MNRAS*, 480(4):4955, 2018. 132

[534] M. Arca-Sedda, B. Kocsis, and T. D. Brandt. *MNRAS*, 2018. 132

[535] C. Guépin et al. *JCAP*, 1807(07):042, 2018. 132, 133

[536] H. Ploeg et al. *JCAP*, 8:015, 2017. 132, 133

List of Figures

List of Tables